New experimental constraint on the reaction rate of ^{67}Zn(n,γ)^{68}Zn

Frida Woldstad Furmyr

Thesis submitted for the degree of
Master in Nuclear Physics
60 credits

Department of Physics
Faculty of Mathematics and Natural Sciences

UNIVERSITY OF OSLO

Spring 2019

New experimental constraint on the reaction rate of ^{67}Zn(n,γ)^{68}Zn

Frida Woldstad Furmyr

New experimental constraint on the reaction rate of ^{67}Zn(n,γ)^{68}Zn

http://www.duo.uio.no/

Printed: Reprosentralen, University of Oslo

Acknowledgements

First of all, I want to thank my supervisors Gry Merete Tveten and Ann-Cecilie Larsen for all the help, support and thorough explanations you have given me. Thank you for spending your evenings on late video calls to California during the fall semester, and for leaving your office door open every day during this spring. I also want to thank you both for being an inspiration to me, opening up my eyes to nuclear physics a little over two years ago. Doing my masters in such an inclusive and friendly group as the nuclear physics group in Oslo is a choice I will always be grateful I made. I want to thank the whole group for the fun everyday lunches, exciting seminars and trips, and also for helping out taking shifts at the experiment. A special thank you to Sunniva Siem for being inclusive towards, and thoughtful of your students, I truly felt like you were taking care of us all the way.

I would also like to thank the Intpart project for all the possibilities of travel it has given me in the course of two years, enabling international experiments and collaborations. As a side effect to learning more about physics, I've now been to corners of the world where I have never remotely been before, and thereby also learning a lot about culture, people and myself. I want to especially thank Prof. Utsunomiya for a great experience in Japan due to his perfect hospitality during the NewSUBARU experiment, and for interesting data discussions. Another thank you to his students for helping out with long night shifts during this experiment, I learned how exhausting these can be. Thank you also to Prof. Bernstein for the experience of participating in your group at the Lawrence Berkeley Lab, both at an exciting medical isotope production experiment, and at the friday happy hours! And thank you to Hannah for dragging me to said happy hours in busy times. Experiencing a new country and university with you was amazing.

I want to thank my family for believing in me, and supporting me going after my passion even in times when I felt dumb and hopeless, helping me believe I could make it after all. And thank you to Dr. E for not only being supportive and patient, but also for reminding me "You only have a bachelors degree!", as it has been quite motivational. Lastly, I want to thank my office pals, my nuclear girls, for making these years special, fun and for making me feel safe. I know you have my back, and I am glad for this environment we have had together, I truly believe it is special.

Frida Woldstad Furmyr
Oslo, May 23, 2019.

Contents

List of Figures

Chapter 1

Introduction

We are living in a universe composed of a great variety of elements and isotopes. 118 elements have been identified [1] (94 chemical elements are found terrestrially), and 252 isotope variations of these elements are considered stable [2]. Mapping our understanding of the universe we live in is a complex and still ongoing journey in science. One of the *"Eleven Science Questions for the New Century"* [3] is: **How do we explain the origin of the heavier elements: from iron to uranium?** To make an attempt at answering this question, let us start from the beginning.

Each element can take several isotopic forms, each form containing a nucleus with its own characteristic nuclear properties, different from all other nuclei. The vast amount of discovered isotopes is shown in the Chart of Nuclides in Figure 1.1. Luckily, the variations are simply consisting of different amounts of two simple components: neutrons and protons. Only for very high energies can a nucleon be produced or annihilated. All "prompt" nuclear reactions can be described as a shuffling and reshuffling of neutrons and protons into new nuclei, the only exception being the β-decay process where an interchange between a proton and a neutron occur. In principle, these reactions enable any transformation from one nucleon into another, even at low energy.

The matter in our universe consists of many elements in a given abundance, as shown in Figure 1.2. After the Big Bang, the universe consisted of a dense and hot quark-gluon plasma, which quickly drifted apart, cooled down and allowed the quarks to settle into their preferred constellation: protons and neutrons. It seems likely that all elements evolved from simple hydrogen since protons are stable, while neutrons will eventually decay into to a proton. In the very early stages after the Big Bang, chemical reactions occurred creating a few light elements like beryllium and lithium. But chemistry alone far from explain the elemental abundance we see today. Hydrogen ^{1}H is by far the most abundant element to this day ($\sim 71\%$), followed by helium ^{4}He ($\sim 27.4\%$), which is formed due to stellar burning of hydrogen. This type of stellar burning happens as the star possesses a self-governing mechanism where the temperature is adjusted so that the energy flow through the star is balanced through generation of nuclear energy. The remaining ($\sim 1-2\%$) consists of what astrophysicists refer to as "Metals": every other element we know to exist [4]. After production

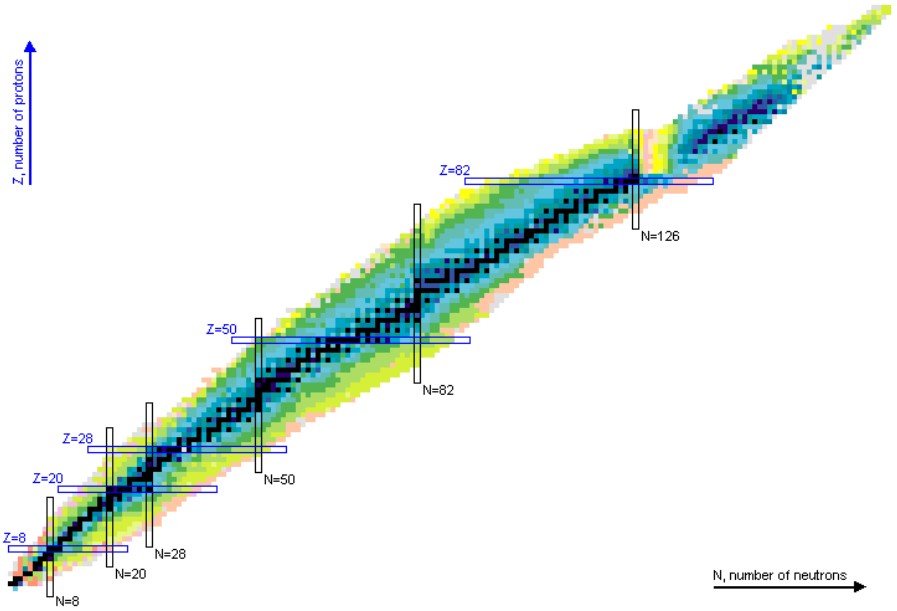

Figure 1.1: The Chart of known Nuclides, where each plotted box represent one nuclei with the number of neutrons in the nuclei plotted against the number of protons. The colors indicate the half-life of the isotope, where the valley of stability in black in the center hosts the stable isotopes. Figure is taken from Ref. [2].

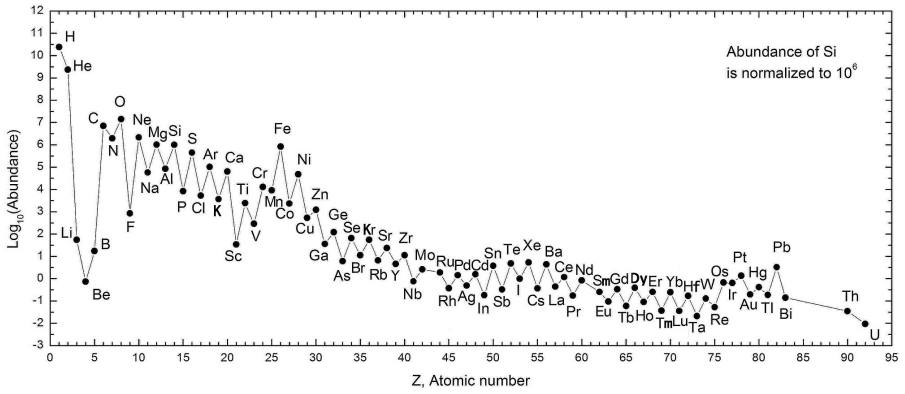

Figure 1.2: Abundances of the chemical elements in the Solar System. Figure is taken from Ref. [5].

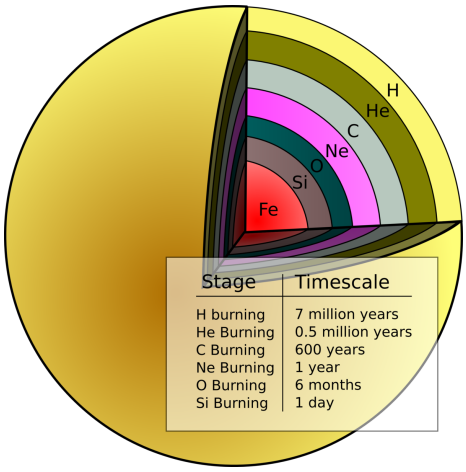

Figure 1.3: An illustration of the Stellar Burning happening in shells inside large stars. Figure is illustrated by Ref. [6], reflecting the content of Ref. [7].

of helium from hydrogen burning, higher temperatures are generated through gravitational collapse and increasing pressure to burn helium, which creates carbon, and so on. The stellar burning cycles continue in a similar way, in layers as shown in Figure 1.3, up to the point where a star no longer can fuel its energy production from fusing lighter elements together. This process therefore halts at iron, and we need other processes to explain why we for example have beautiful necklaces of silver and gold.

In the famous 1957 paper, E. M. Burbidge et al. [8] proposed that all elements except very light chemical elements are synthesized inside stars, as a result of nuclear reactions. Another article appearing that same year by A.G.W Cameron [9] proposed a very similar hypothesis, and the two articles together are still the framework of the theories we use today.

The most probable way elements heavier than iron are made is through two main contributing processes. They have been given the names s-process (the slow neutron capture process), and r-process (the rapid neutron capture process). The speeds slow and rapid are denoted with respect to the rate of which a β-decay would occur for this isotope, as in a β^--decay a neutron will turn into a proton (and also send out an electron and a neutrino).

The s-process takes place over thousands of years, hence living up to its name. Therefore this process involves neutron capture on stable nuclei. Due to free neutrons decaying quickly, the s-process has to take place in an environment where neutrons are readily supplied over thousands of years. Asymptotic-giant branch (AGB)-stars were showing technetium absorption lines in the ground breaking 1952 article by Merill [10]. This observation provided evidence that the s-process does occur in such stars, as technesium has no stable isotopes, and must have been created at this location. Since then, massive stars with a mass eight times the solar mass (in their helium-burning phase), have been proposed as a potential s-process site as well.

The main assumption for the s-process, is that the time scale $\tau \sim 1/\lambda$, where λ is the reaction rate, for neutron capture (n, γ), is much longer than the time scale of competing β-decay of unstable isotopes: $\lambda_\beta \gg \lambda_{n,\gamma}$. This way, the path towards heavier nuclei travels along the valley of stability (see Figure 1.1), in a slow yet steady manner.

The r-process on the other hand kicks off and ends within only few seconds, and involves the very unstable, neutron rich nuclei only. The main assumption for this process, is that the neutron capture is more likely to happen than the β-decay, $\lambda_\beta \ll \lambda_{n,\gamma}$, so that the nucleus has time to catch one neutron, then another neutron, and another, until it becomes so unstable that the assumption no longer holds. This takes us further right on the Chart of Nuclides, see Figure 1.1, towards the edge of our known isotopes at the *neutron drip line*. This assumption therefore demands an environment of extreme neutron density ($N_n \approx 10^{20} cm^3$). After an r-process cycle has been terminated, a cascade of β^--decays will bring the unstable nuclei back towards stability, to form new stable isotopes of new, heavier elements than were the seed nuclei of the process.

After decades of discussing what the astrophysical site of the r-process could be, the Advanced LIGO and Advanced Virgo gravitational-wave detectors made the first observation of a Neutron Star Merger (one of which is illustrated in Figure 1.4) in 2017 [11]. Following shortly after the gravitational-wave detection, a γ-ray burst was detected by the Fermi Gamma-Ray Burst Monitor [12] and the INTEGRAL telescope [13]. Measurements of a broad range of frequency bands of electromagnetic radiation from the collision were made over the following weeks, and the r-process manifested itself for the first time within the "afterglow" from heavy element production at the site of the merger. We can therefore confirm the speculations that such an environment can host this process. Supernovae are also candidates for hosting the r-process, but this has yet to be proven. But at this point in time, reaction network calculations simulating neutron star mergers are popular tools for attempts at reproducing the elemental abundance distribution.

Within the field of nuclear physics at present date, there are a lot of experiments that are of interest to execute to gather more knowledge about exactly how the nucleus works. In the field of nuclear astrophysics especially, there is one reaction type which is currently important to investigate for many isotopes, at many energy ranges. This reaction is called the neutron capture reaction, a reaction in which a nucleus is introduced to a neutron and picks it up, evolving to a different isotope. The end goal of this master project, is to study how likely a ^{67}Zn nucleus is to introduce a new neutron. This reaction is written as ^{67}Zn(n,γ)^{68}Zn. But why is this specific reaction interesting?

A major study is being done for all the stable isotopes of zink in the search of understanding the nucleosynthesis of heavier elements, with several labs collaborating to get a full understanding of the different perspectives one element can show. Relevant experiments have been performed using ^{68,70}Zn at the Oslo Cyclotron laboratory, and as a collaboration with NewSUBARU in Japan, complimentary experiments were executed for ^{64,66,68}Zn. The neutron rich isotopes

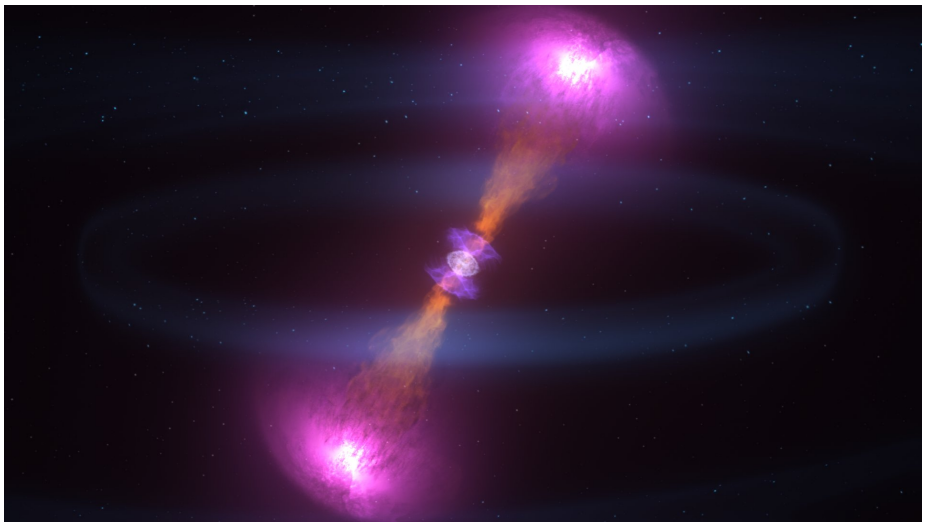

Figure 1.4: An illustration of a Binary Neutron Star Merger. Figure is courtesy of NASA (Ref. [14]).

are important for s-process and r-process models, as improving the measurement for the stable nuclei can help us get better models for development of the processes once they move through the unstable isotopes of Zn. Especially the path towards the "magic" (closed neutron shell nuclide, and therefore more stable) ^{80}Zn is interesting, see Figure 1.5 where the magic isotopes are highlighted in blue. This is a potential branching point for the r-process which is important to get a well founded understanding of. The proton rich side is closer to ^{64}Zn, and this isotope is therefore interesting for another less dominating process. The s- and r-process are often rounded up to contribute all of the abundance of the elements and isotopes, but this is not entirely true. There has to exist another process, called the p-process, which is responsible for about 30 shielded nuclei that can not be reached through s- and r-process. The Zn-project is therefore potentially an important step in the right direction of understanding the processes behind the creation of the elemental abundance we are surrounded by, as a whole.

This master thesis will focus on one of these Zn isotopes. In both experiments, I will be performing measurements on ^{68}Zn; the end-product nucleus of the neutron capture reaction ^{67}Zn(n,γ)^{68}Zn. My goal is to discover more about the nuclear properties of this nucleus, and there are several ways of going about this problem. Nuclear excitation levels can for example be studied by performing collisional experiments, where incoming particles with high energy can transfer energy to a target nucleus, causing an energy excitation. The first experiment discussed in this master thesis (in Chapter 3) is of this type, and was performed at the Oslo Cyclotron Laboratory (OCL). In this cyclotron, light particles are accelerated to quite (from an energy-physics perspective) low energies, and thereafter they are directed towards a ^{68}Zn target. After being excited the target nucleus will eventually (well, in all honesty rather fast) calm down, but release a gleam of light as a result from the energy it gained from

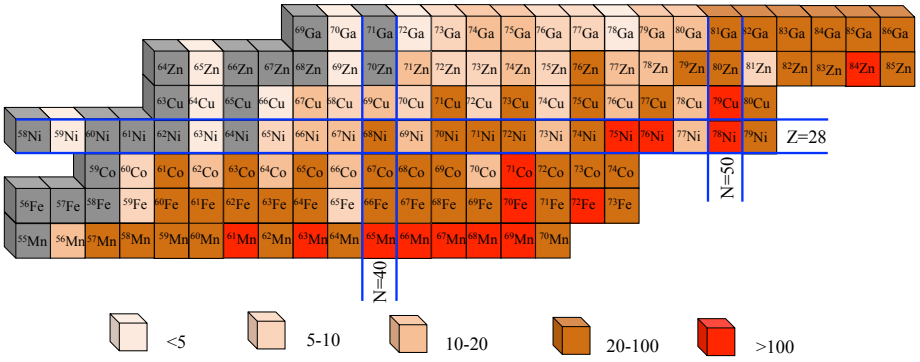

Figure 1.5: Variation in the theoretical prediction of neutron-capture reaction rates around mass 70. The (n,γ) rates were calculated with the reaction code TALYS [15], varying the level density and γ-strength function. Figure taken from Ref. [16].

the colliding particle. This gleam of light is a light particle, a photon or γ-ray, which is measured using the newest instrumental addition to OCL: The γ-ray detector array OSCAR. The reaction occurring is ^{68}Zn(p,p$'$)^{68}Zn. This is one of the ways to study how excited our target was, from measuring the energy of this γ-ray, and from this learn about how the energy levels in the ^{68}Zn nucleus are distributed. Among the structural qualities that are possible to extract from this data are the Nuclear Level Density, and the γ-ray strength function, and these will be thoroughly examined and discussed in this thesis.

The other experiment involved looking at the probability of a neutron being emitted as a response to photon irradiation: ^{68}Zn(γ,n)^{67}Zn, using slightly higher energy γ-rays with an energy above the so called neutron separation energy S_n, which suitably is the energy threshold where a ^{68}Zn starts seeing the release of one of its neutrons as a way of letting off some of the excess energy received. This experiment was performed at NewSUBARU in Japan, and Laser Compton Scattering was used as a way of acquiring almost mono-energetic γ-rays, which is crucial to this experiment. ^{68}Zn was placed in a neutron detecting chamber to count how many neutrons were released from the target from being exposed to different γ-energies. The details on this experiment is given in Chapter 4.

This master thesis will go into detail about the experiments, the calibration procedure and the data analysis. In Chapter 2, the important qualities level density and γ-strength function, and some other theoretical phenomena I find very relevant to the context, will be covered. The end goal is to look at the experimental data sets as a representation of the γ-ray strength function as a whole, and apply it for discussions in Chapter 5. I will discuss the program TALYS [15], applied to estimate the reaction rates of the neutron capture reaction ^{67}Zn(n,γ)^{68}Zn from the resulting γ-strength function. Using this method and other experimental approaches on different isotopes of interest, we will eventually uncover more about the way the neutron capture processes unfolds, and how and why the element abundance in our Solar System has the composition we measure today.

Chapter 2

Theory

Although this master thesis is heavily based upon experimental studies, the work is also carried out in a theoretical framework which is necessary to understand before both executing such experiments, and also to read about the experiments. At this point, there are plenty of experimental data for neutron capture on stable isotopes [17, 18] and (n,γ) reactions are often seen as the best understood type of nuclear reaction. However, some isotopes are difficult to study experimentally. Those include those where (n,γ) takes you into another stable isotope and isotopes with too short lifetime to be made targets of. Several labs in Europe have developed setups for studying radioactive targets, but the lifetime must be long enough to be able to make a target. On the theory side, there are many open questions related to nuclear structure far away from stability. Stand-alone theories do not yet explain the full truth, nor manage to reproduce the abundance of elements in our solar system. The theoreticians therefore demand new, relevant experimental data, so that the theories and models can be improved. This is why an international collaboration is studying several Zn-isotopes, attempting to improve our theoretical understanding of this element, and mass region. Leaving the experimental side of things for now, let us look at the theory behind the experiments as it stands today.

2.1 Nuclear reactions and scattering

A large part of experimental nuclear physics is performing fixed target experiments, where a chosen target nucleus is placed in a chamber, and bombarded with a beam of accelerated particles, inducing nuclear reactions. In nuclear reactions with no particle production, the number of nucleons is conserved. A general nuclear reaction is often written as

$$a + A \rightarrow B + b, \tag{2.1}$$

where a is the incoming particle, A is the target nucleus, B is the target nucleus after the nuclear reaction, and b the outgoing particle from the reaction. The incoming and outgoing particles, are usually lighter than the target nucleus. If a is a photon, we call it a photonuclear reaction. If b is a photon, it is called a radiative capture reaction. If the resulting particles differ from the initial partners, a nuclear transmutation has taken place.

However, if the final reaction partners are identical to the initial ones, they have gone through an elastic scattering event where kinetic energy is conserved and the initial and final quantum states are the same. This reaction is written as:

$$a + A \rightarrow A + a. \tag{2.2}$$

Another outcome is inelastic scattering, where the final reaction partners are identical before and after the reaction, but their initial and final quantum states are not the same throughout the scattering process. The target nucleus may be excited in the process. This reaction can be written as:

$$a + A \rightarrow A' + a'. \tag{2.3}$$

Another form of notation which is often used, and will be used extensively in this text, is:

$$A(a, a')A', \tag{2.4}$$

and it is popular as it is more efficient, but may not be as descriptive of the reaction to anyone new to the field of nuclear physics.

2.1.1 Nuclear Reaction Models

To describe a nuclear reaction, the quantum states of the partners both before and after a collision must be known, as well as the Hamiltonian operators working on the initial quantum state, governing the nuclear reaction process. There is a strong connection between nuclear reaction models and nuclear structure, and nuclear models are the main tool for investigating the properties of nuclear systems. Another important part of modelling nuclear reactions, is knowing the potentials governing the interaction. Depending on the situation, a lot of potentials may be necessary to properly describe a given reaction.

Particles interact through four different forces: The electromagnetic force, the weak force, the strong force and the gravitational force. Depending on the reaction in question and the kinetic energy of the particles, the force dominating will vary. In our experiment our particle has a high kinetic energy, such that the strong force governed by the nucleus will dominate as the particle gets close. In the analysis, all conservation laws specific to the the strong nuclear force are applied, and the symmetry properties of space and time are also conserved.

2.1.2 Nuclear Reaction Mechanisms

The Compound Nucleus Mechanism

The compound nucleus mechanism was proposed by Niels Bohr in 1936 [19]. The main assumption of a compound nucleus formation is that the entire kinetic energy of the incident particle gets distributed evenly and statistically between many nucleons in the formed compound nucleus. It also assumes that the nuclear reaction takes place in two independent stages. First, the incident particle merges with the target nucleus. Then the incident particle transfers a significant amount of energy to the target nucleus, distributes it among the nucleons, and excites the target nucleus to a higher energy state. The second stage has

an excited nucleon, and the incident particle may be emitted through inelastic scattering. Other situations may occur, as for example when more nucleons are excited in the process, not just one.

If the incoming particle is a photon, one can assume that only one nucleon gets excited. The photoabsorption cross section for incoming photons with energies between 13 and 25 MeV is usually dominated by the giant dipole resonance (GDR) [20], and is excited by the electromagnetic interactions between the reaction partners.

The second stage in a nuclear reaction in this model, depends on the energy and the emission threshold of the nucleons of the target. If the re-distributed energy is higher than a threshold, some sort of particle emission can be the result. This energy re-distribution takes a long time, $\sim 10^{-16}s$. The compound nucleus "forgets" how it was formed due to many reactions happening in this relatively long period of time. Therefore the relative probability of the decay of an excited compound nucleus is independent of its initial partition.

The disintegration of a compound system can be described by defining the energy magnitude $\Gamma(E)$ from the mean lifetime τ(E) as [21]:

$$\Gamma(E) = \frac{\hbar}{\tau(E)} \tag{2.5}$$

where Γ will later be referred to as a total level width, and $\hbar = 6.582119 \times 10^{-16}$eVs is the reduced Planck constant. As a compound nucleus can decay into different channels, this Γ as defined above is divided into decay rates over specific channels:

$$\Gamma(E) = \sum_{\beta} \Gamma_{\beta}(E), \tag{2.6}$$

with the sum $\sum_{\beta}$ extended over all channels β which the compound nucleus can decay into. Γ_{β} is the specific decay rate, or the partial width for the decay into channel β.

The nuclear excited state can be a bound state embedded in the continuum or quasi-continuum (see section 2.2), and described by the resonant Breit-Wigner distribution [22]:

$$P(E) = \frac{\Gamma}{2\pi(E - E_0)^2 + \frac{\Gamma^2}{4}} \tag{2.7}$$

where E_0 and Γ are the energy centroid and distribution width. Excited compound nucleus states are characterized by narrow energy distributions, and widths in the range 0.066 eV - 0.6 keV [23] using Eq. (2.5). The total Γ width of the Breit-Wigner distribution is the sum of the widths of all accessible partial distributions for different processes like elastic scattering, inelastic scattering and γ-emission. The total decay width would be given as:

$$\Gamma = \Gamma_{elastic} + \Gamma_{inelastic} + \Gamma_{\gamma}. \tag{2.8}$$

The probability of particle emission through the compound nucleus mechanism is the same for the angles θ and $\pi - \theta$, and so the differential cross section is

symmetrical with respect to $\theta = 90°$, a result from the conservation of total parity and angular momentum in nuclear interactions. Strong angular dependence is often the result of a direct reaction, only involving a few of the particles in the nucleus. The lack of such a strong dependence does indicate that the energy in the reaction will be distributed among all particles in the nucleus. It therefore in principle impossible to determine exactly how the compound nucleus was initially formed, according to this model.

The Pre-equilibrium Mechanism

The pre-equilibrium mechanism assumes the incident particle interacts only with a few of the nucleons in the target, not all. These processes have a lower level of complexity than those in the compound nucleus mechanism, and takes place in a shorter period of time ($\sim 10^{-20} - 10^{-19}$ s). These intermediate nuclear processes have excited states with a typical total width Γ = 6.6 - 66 keV [23], by using Eq. (2.5).

Direct Reactions

Direct reactions are single-step reactions executed in a short time interval ($\sim 10^{-22} - 10^{-21}$ s). These reactions have high particle emission probabilities, and are called single particle resonances. They are characterized by the typical total width 0.66 - 6.6 MeV [23], again by using Eq. (2.5).

Direct reactions represent reactions where the incident particle interacts in one single, or very few, steps with the target nucleus. During each step one of the compound system nucleons is in a virtual state, meaning it is in a quantum mechanical state which will have such a short lifetime it can not be measured. According to the shell model, the incident particle will most likely interact with the surface target nucleons. For other interactions with lower-laying nucleons to happen, one would need higher energies to excite the nucleon.

Stages of a Nuclear Reaction according to the Weisskopf-Feshbach model

Figure 2.1 shows the unitary treatment of nuclear reactions proposed by Weisskopf and Feshbach [24], where any nuclear reaction is assumed to take place in several stages. In the first stage, the particle beam scatters elastically by direct interaction with the target nuclei, which by incoming particles is considered to be a solid sphere. One particular type of elastic scattering is "shape-elastic scattering", which in addition to conserving the quantum states in an elastic collision, also conserves the relative orientation of the angular momentum.

The second stage involves a different range, where the incident particle and target interact through the strong interaction. This is where a compound system

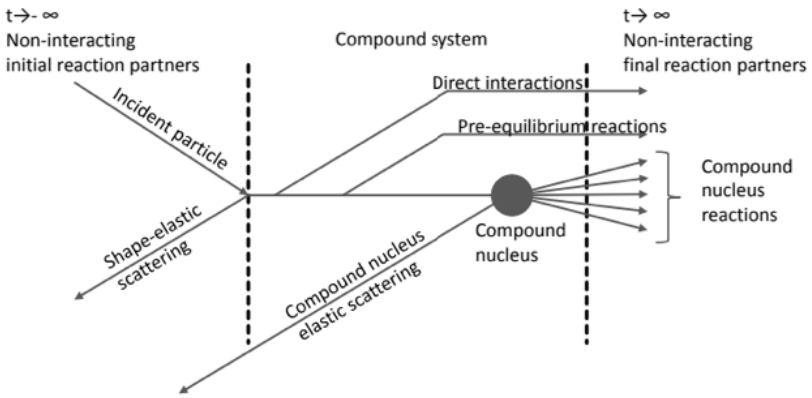

Figure 2.1: The Weisskopf-Feshbach model of the stages of a nuclear reaction. Figure taken from Ref. [23], which is a reconstruction of an original figure from Ref. [25].

is formed, and the number of interactions occurring will decide if the outgoing particle is emitted directly, pre-equilibrium, or through a statistical bound state embedded in the continuum. The third and final stage consists of the resulting reaction partners after the collision, which are no longer interacting with each other, and the scattering event is complete.

2.2 Nuclear Level Density

In the low energy regime the nuclear levels are well defined, but as the excitation energy of a nucleus increases, the levels will be stacked closer and closer together, as seen illustrated in Figure 2.2. Eventually they are bunched so close that they are overlapping creating a continuum of energy levels. Between these two regions of discrete levels and the continuum is the quasi-continuum region. In the quasi-continuum, the level density is assumed to depend on how close the isotope is to a closed shell where the single particle distance will increase. At higher energies this difference will not be able to show through the vast amount of available states.

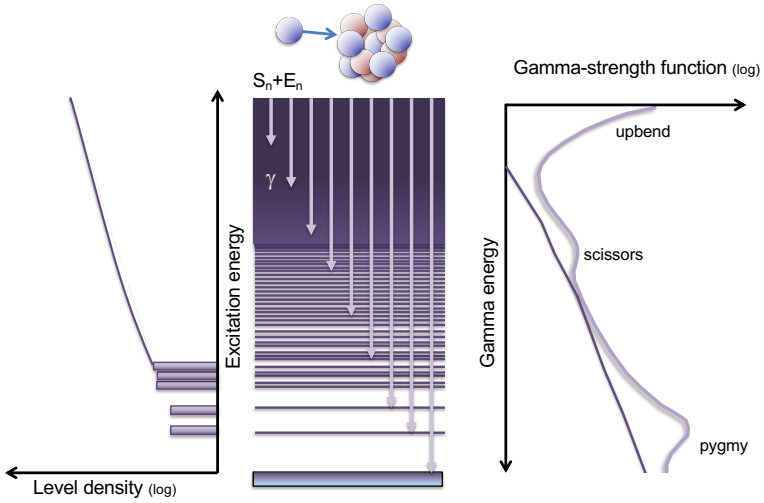

Figure 2.2: Illustration of the level density (left), the energy levels in a nucleus (middle) and the shape of the γ-ray strength function (right). Figure taken from Ref. [26].

The Nuclear Level Density (NLD) is defined as the number of levels per unit excitation energy, the most common unit being MeV, and is a measure of available quantum levels at a given excitation energy. There are a variety of models predicting level densities in the different energy regions. For the lower energy levels, up to about 10 MeV, the Constant Temperature Model [27] is the most commonly recommended model. Above this energy, the Fermi Gas Model [28] is recommended after the so called phase transition from the Constant Temperature region into a more gas-like chaotic region. The Fermi Gas Model is the very first level density model, proposed in 1936. In the continuum, a suggested model is the Generalized Superfluid Model (GSM) [29], considering superconductive pairing correlations when determining the level density. The two first models will be further discussed as they are both very relevant, but the GSM will be left at this note. There are several other models attempting to describe the level density.

The NLD tells us about the number of energy levels a system of several particles have at a given excitation energy. NLD is interesting as it can help us understand the complex quantum mechanical system which is the atomic nucleus. It is essential to calculate reaction cross sections, which will be explained in Chapter 2.5, and therefore also crucial to our understanding of nucleosynthesis processes in astrophysics. When the level density is found experimentally, it is directly related to the density of states; the number of physical realizations of the system at a given excitation energy.

To theoretically calculate the level density one can, in addition to using models, use numerical Monte Carlo shell-model calculations. These calculations are usually quite precise for light nuclei, but as the number of nucleons increase, experimental measurements to find a correct parametrization of the level dens-

ity are needed. Large-scale shell model calculations by the Oslo group have also been performed very recently in order to explore level densities [30]. However, as no model or simulation is as satisfying as data from the real world, the group at OCL has been successful in experimentally extracting the level density from primary γ-ray matrices under the neutron separation energy S_n, and the method behind this will be discussed in Chapter 3.

2.2.1 The Back Shifted Fermi Gas model

The Fermi Gas Model was first proposed by Bethe [28], and is based on the theory of Fermi statistics. The nucleus is modelled as a gas of non-interacting fermions, and as a function of excitation energy E_x the level density $\rho(E_x)$ is described as

$$\rho(E_x) = \frac{\sqrt{\pi}}{12} \frac{e^{2\sqrt{aE_x}}}{a^{1/4}E_x^{5/4}}, \tag{2.9}$$

where the constant level density parameter a determines the single-particle level density at the Fermi surface. This was later extended to The Back Shifted Fermi Gas model [31], which will be denoted FG as the older Fermi Gas model will not be used. This newer version is modified by treating the energy shift and level-density as free parameters. The model is based on a lot more samples of nuclei and their excitation energy, and expresses the level density by this formula:

$$\rho(E_x) = \frac{e^{2\sqrt{a(E_x-E_0)}}}{12\sqrt{2}\sigma a^{1/4}(E_x-E_0)^{5/4}}, \tag{2.10}$$

where ρ still grows exponentially as $e^{\sqrt{2aE}}$, as is characteristic for the Fermi Gas model. E_0 is the back-shift in excitation energy from the pairing gap, and σ is the spin cutoff parameter estimated in Ref. [31] as:

$$\sigma^2 = 0.0146A^{5/3}\frac{1+\sqrt{1+4a(E_x-E_0)}}{2a}, \tag{2.11}$$

where A is the mass number of the nucleus.

2.2.2 The Constant Temperature Model

In order to model the nuclear level density for all excitation energies, the FG model is commonly paired with the Constant Temperature (CT) model. The CT model, first proposed by Ericson [27, 32] in 1959, has been shown to work well for lower excitation energies, where exact solutions are reproduced [33]. The formula for the CT level density $\rho(E_x)$ is given by Ref. [34] as:

$$\rho(E_x) = \frac{1}{T}e^{(E_x-E_0)/T}, \tag{2.12}$$

where E_x is the excitation energy, T is the temperature and E_0 the back-shifted energy. Both the temperature and energy back-shift are parameters fitted especially for this model. To estimate the constant temperature: look at the increase in level densities, and determine the slope of this increase.

The parameter T, a kind of effective temperature, reaches its minimum at

$N = Z$, or at neighboring odd nuclei [33]. It is kept constant within a wide range of excitation energies E_x, which is the reason for the name Constant Temperature model. This effective temperature is introduced as an inverse coefficient of the level density as a function of E_x. The parameter T in the level density is an analog of the limiting Hagedorn temperature in particle physics [35]. The thermodynamic temperature T_{t-d} in the ground state is zero, and approaches the value T as the excitation energy approaches 10 MeV or higher. This does not mean the system is unable to reach higher temperatures, but in doing so, there will be a transition to a chaotic stage of randomly interacting constituents. The common interpretation of this transition, is a phase transition from superfluid paired dynamics to a normal Fermi liquid phase. This however does not hold, as the behavior persists if the standard attractive pairing interaction is removed from the Hamiltonian. We seem to be dealing with a general stochastization of dynamics as a typical feature of quantum many-body systems [33].

2.3 The γ-ray Strength Function

The γ-ray Strength Function (γSF) is a measure of the average, reduced γ-decay probability, and it reveals information about the structure and dynamics of the nucleus.

The γ-ray strength function is the distribution as a function of γ-ray energy, of the average reduced width for transitions of a particular multipole type. Transitions in multipole type are written as XL where X is E for electric or M for magnetic transition, and L is the multipolarity of the transition. For transitions of energy E_γ between E_i and E_γ ($E_i < E_\gamma$) the γSF f_{XL} is presented as [36]:

$$f_{XL}(E_i, J_i, \pi_i, E_\gamma) = \frac{\langle \Gamma_{XL}(E_i, J_i, \pi_i, E_\gamma) \rangle}{E_\gamma^{(2L+1)}} \rho(E_i, J_i, \pi_i), \tag{2.13}$$

where $\Gamma_{XL}(E_i, J_i, \pi_i, E_\gamma)$ is the partial width of the γ-ray averaged for transitions within an initial excitation energy bin E_i for levels with spin J_i and parity π_i around the energy E_γ. $\rho(E_i, J_i, \pi_i)$ is the average level density, and the energy dependence on L is included in the factor E_γ^{2L+1}, a penetration factor. Just like the NLD, the γSF is an average quantity. Therefore the regions where it is appropriate to discuss level density over single levels, also makes it useful to think in terms of a γSF over individual radiation widths. From inelastic scattering or photoabsorption cross section measurements where a photon beam has a large energy spread compared to the level spacing $D(E_i, J_i, \pi_i)) = \frac{1}{\rho(E_i, J_i, \pi_i)}$, one can obtain such average data [36].

The transmission coefficient $\mathcal{T}_{XL}(E_\gamma)$ represents the escape probability for a γ-ray stuck inside the nucleus [21]. In general, γ-rays try to escape many times before they will finally be emitted, causing the probability of a transmission to be much smaller than the probability of reflection. $\mathcal{T}_{XL}(E_\gamma)$ characterizes an exited state's average electromagnetic properties, connecting it to photoabsorption and radioactive decay processes. It can be defined in terms of the γSF by the relation

$$\mathcal{T}_{XL}(E_\gamma) = 2\pi E_\gamma^{2L+1} f_{XL}(E_\gamma). \tag{2.14}$$

Following Fermi's Golden Rule [37] [38], the γSF can be used to calculate photo-absorption cross sections due to the principle of detailed balance [21]. The γSF represents the distribution of average, reduced partial γ-transition widths. γ-decay is related to a "downward" strength function, and to find the "upward" one can determine the average photo-absorption cross section $\langle\sigma_{XL}(E_\gamma)\rangle$ summed over all possible final state spin values [39]:

$$f_{XL}(E_f, J_f, \pi_f, E_\gamma) = \frac{1}{(2L+1)(\pi\hbar c)^2} \frac{\langle\sigma_{XL}(E_f, J_f, \pi_f, E_\gamma)\rangle}{E_\gamma^{(2L-1)}} \tag{2.15}$$

where E_f is the final energy bin after a photo-absorption reaction, and in the excited levels J_f is the final spin and π_f the final parity.

When calculating nuclear reaction rates and cross sections with the open-access codes available, the extreme statistical model is used [36]. It assumes the strength function to independent of spin and parity. This is valid if the wave functions of the highly excited levels can take many configurations. The assumption of detailed balance is also more reliable in the case of the extreme statistical model.

2.3.1 E1 and M1 Resonances

In Figure 2.2 is a sketch of the shape of the γSF, mentioning the most important resonances that can be discovered in our results. The most important of the resonance models are the Giant Electric Dipole Resonance (GDR), which is believed to stem from harmonic vibrations where neutrons and protons oscillate off-phase against each other. This is shown to strongly influence the strength functions of most isotopes. Secondly, there is the Giant Magnetic Dipole Resonance (GMDR), referred to as $M1$, modelled by a spin-flip resonance model. There is experimental evidence of other resonance structures in the γSF, which are smaller in magnitude. Among these are the pygmy dipole resonance (PDR), a debris of the higher energy GDR due to destructive inference. High energy resolution experiments performed during the last decade reveal fine structure of the PDR in many nuclei [40].

The γSF of a nucleus under about 3 MeV is expected to be dominated by the receding tail of the GDR [41], so when the first measurements of a sizeable low-energy enhancement in this region was discovered for $^{56,57}Fe$ [42], scientists were surprised. This enhancement is later referred to as the *upbend*, and in the following years this was observed through the Oslo method, and other methods, in a wide range of nuclei. What makes it even more interesting, is the fact that the presence of such a low energy enhancement may also enhance the $r-process$ (n,γ) reaction rates by a factor of 10-100 [43]. Nevertheless, the physical mechanism behind the upbend has been puzzling, and later after being explored it seems to be dominantly of dipole nature [44]. Shell model calculations [45, 46] have shown very strong M1 transitions at these lower γ-energies, but it has also been suggested that the upbend is caused by thermal excitations in the continuum, causing lower energy E1-transitions [47].

The dominant part of the γSF is the $E1$ part, which can be described in its

simplest form with a standard Lorentzian model, or with an enhanced generalized Lorentzian model. For the $E1$ resonance, the standard Lorentzian model can be represented as

$$f_{E1}^{SLO}(E_\gamma) = c \cdot \frac{\sigma_{tau} E_\gamma \Gamma_r^2}{(E_\gamma^2 - E_r^2)^2 + E_\gamma^2 \Gamma_r^2)} \tag{2.16}$$

where the conversion constant $c = (3\pi^2\hbar^2c^2)^{-1} = 8.674{\cdot}10^{-8}\text{mv}^{-1}\text{MeV}^{-2}$, σ_r is the peak cross section, E_r the energy centroid and Γ_r the width of the resonance.

The enhanced generalized Lorentzian, as described in [48], appears more complicated, as it corrects for the widths dependence on temperature T and energy E. It also includes a term for the the γ-ray strength function at $E_\gamma = 0$.

$$\begin{aligned} f_{E_1}^{EGLO}(E_\gamma) = c \cdot \sigma_r \Gamma_r [\frac{E_\gamma \Gamma_{E_n}(E_\gamma, T)}{(E_\gamma^2 - E_r^2)^2 + E_\gamma^2 \Gamma_{E_n}^2(E_\gamma, T)} + 0.7 \cdot \frac{\Gamma_{E_n}(0,T)}{E_r^3}], \\ \Gamma E_n(E_\gamma, T) = [k_0 + (1-k_0)\frac{(E_\gamma - \epsilon_0)}{E_r - \epsilon_0}]\Gamma_K(E_\gamma, T), \\ \Gamma_k(E_\gamma, T) = \frac{\Gamma_r}{E_r^2}(E_\Gamma^2 + 4\pi^2T^2). \end{aligned} \tag{2.17}$$

where k_0 is the enhancement factor found to reproduce the reference strength around the energy $\epsilon_0 = 4.5$ MeV. The Back Shifted Fermi Gas model gives

$$k_0 = \begin{cases} 1 & \text{for A } < 148 \\ 1 + 0.09(A-148)^2 e^{-0.18(A-148)} & \text{for A } \geq 148 \end{cases} \tag{2.18}$$

where A is the nucleus mass number.

Several models attempt to quantify the γSF. The dominating radiation types involved in γ-emission being from the GDR and GMDR, the total strength function can be be decomposed to the different contributions from E1 and M1.

$$f_{tot} = f_{E1} + f_{M1} \tag{2.19}$$

However, there are other resonances also relevant to include as contributors for the total strength function in some cases, like the pygmy dipole resonance f_{pyg}, and the upbend f_{upb}. These can be added in in a similar way, leaving us with the complete strength function

$$f_{tot} = f_{E1} + f_{M1} + f_{pyg} + f_{upb} \tag{2.20}$$

2.4 The Brink Hypothesis

The Brink hypothesis [49] is an essential assumption behind the method that will be introduced in Chapter 3: The Oslo Method. This hypothesis proposes that the γSF only depends on the γ-ray energy E_γ, and not the temperature of the final state. It claims that similarly to the ground state, excited states also have an electric giant dipole resonance built on them, only shifted towards higher energies by the energy leap from the ground state to the excited state. The

probability of γ-decay from excited states will depend on the density of states in the decay region, and also how similar the resulting nucleus is to the original. Looking at the energy distribution of only the first γ-rays in the cascades of γ's, a first generation spectrum is acquired, which can tell us about both these two qualities. This can be formulated mathematically as

$$P(E_i, E_\gamma) \propto \tau(E_\gamma)\rho(E_i - E_\gamma), \tag{2.21}$$

where E_i is the initial excitation energy, $\mathrm{P}(E_i, E_\gamma)$ is the experimental, normalized first generation matrix, τ is the γ-ray transmission coefficient, and ρ is the level density. The proportionality to $\rho(E_i - E_\gamma)$ is in accordance with Fermi's golden rule [37] [38]. By utilizing our γ-particle coincidence data, one may extract both of these.

2.5 Cross Sections and Reaction Rates

When attempting to understand the nucleosynthesis, reaction probabilities are key pieces of information in the puzzle. A reaction cross section σ is a much used measure of this probability. Another is the reaction rate, which is often used in astrophysics.

The velocity v of the particles in a stellar environment govern the temperature T, which governs the cross section σ. The *reaction rate* r_{01} between the two species, projectile (0) and target (1) in a reaction $0 + 1 \rightarrow 2 + 3$ can be expressed as [4]:

$$r_{01} = N_0 N_1 \int_0^\infty v P(v) \sigma(v) dv \equiv N_0 N_1 \langle \sigma v \rangle_{01}, \tag{2.22}$$

with N_0, N_1 being the number density of the different particle species and $\langle \sigma v \rangle_{01}$ is the reaction rate per particle pair. $P(v)dv$ is the normalized probability that the relative velocity of the species in the interaction are in the interval $[v, v+dv]$.

Stellar plasma is non-degenerate, with velocities well below the relativistic region. Therefore, in most cases, the velocities can be described by a Maxwell-Boltzmann distribution as the reaction initiated by the motion are thermonuclear reactions:

$$P(v)dv = (\frac{m_{01}}{2\pi kT})^{3/2} e^{-m_{01}v^2/(2kT)} 4\pi v^2 dv, \tag{2.23}$$

where k is the Boltzmann constant $k = 8.6173 \times 10^{-5}$eV/K, and m_{01} is the reduced mass $m_{01} = m_0 m_1/(m_0 + m_1)$.

For neutron-induced reactions (like (n, γ)) the reaction rate is often expressed by the *Maxwellian-Averaged Cross Section* $N_A\langle\sigma\rangle_T$ [4]

$$\begin{aligned} N_A\langle\sigma\rangle_T \equiv \frac{N_A\langle\sigma v\rangle}{v_T} = \frac{1}{v_T} N_A \int_0^\infty v P(v) \sigma_n(v) dv = \\ \frac{4}{\sqrt{\pi}} \frac{N_a}{v_T^2} \int_0^\infty v \sigma_n(v) (\frac{v}{v_T})^2 e^{-(v/v_T)^2} dv \end{aligned} \tag{2.24}$$

with the thermal velocity $v_T = \sqrt{2kT/m_{01}}$, which is the maximum of the velocity distribution.

Chapter 3

Experimental details and data analysis of the ^{68}Zn(p,p$'\gamma$) measurement

3.1 Experimental setup at OCL

At the Oslo Cyclotron Laboratory (OCL), we are using a cyclotron to accelerate light beam particles, namely protons, deuterons, ^{3}He and ^{4}He. When using protons, they can be accelerated to energies from 2 - 35 MeV. In the case of this experiment, we accelerated protons to an energy of 16 MeV. The accelerated particle beam is directed into the experimental hall (see Figure 3.1), where OSCAR, the γ-detector array, and SiRi, the particle telescope, are placed, see Figure 3.2. In the middle of this setup, we placed a target foil of ^{68}Zn, and bombarded it with our beam. We studied the inelastic scattering reaction ^{68}Zn(p,p$'$), where the nuclei are excited by the incoming beam, and sends out a γ-ray (or several in a cascade: average multiplicity of 2.5 - 3) as a result of de-excitation. Coincidences between detected outgoing protons and γ-rays were measured, to be sure that the γ-rays are truly resulting from the reaction in question.

At OCL, the cyclotron being used is an MC-35 Scanditronix cyclotron. This is connected to target stations via beam lines as seen in Figure 3.2.

The beam line consists of air-tight pipes, where the ion beam can travel from the cyclotron to the target station while being in vacuum and hence not collide with air molecules on the way. To focus and guide the particles through the pipes, a magnetic fields $\vec{B}$ is induced by applying a Lorentz force onto the particle given as

$$\vec{F} = m\vec{a} = q\vec{v} \times \vec{B}. \tag{3.1}$$

In order to direct and focus the beam, both dipole "D" and quadrupole "Q" magnets are applied along the beam line, as shown in Figure 3.1. A switching magnet is used to select a beam line. Since a particle species defined by its mass

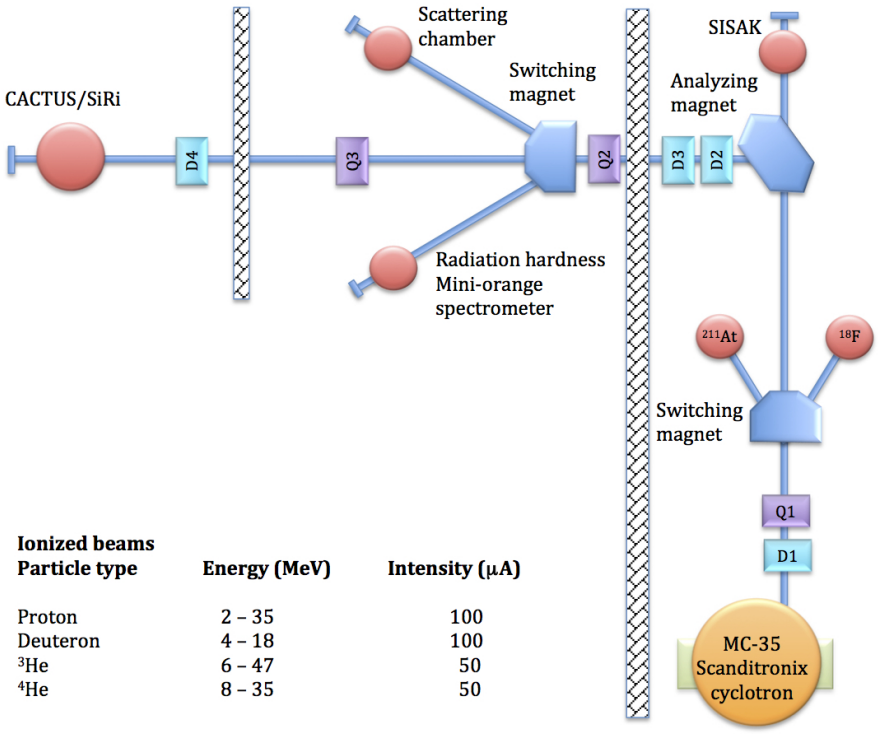

Figure 3.1: The experimental setup at the Oslo Cyclotron Laboratory. (Taken from the OCL website, Ref. [50].) CACTUS is now replaced by OSCAR.

m and its charge q, and the energy of the particle is related by

$$E_{kin} = \frac{1}{2}mv^2. \tag{3.2}$$

The magnetic field described by Eq. (3.1) will deflect a given particle type of a given energy into the beam line. An analyzing magnet is used to remove any beam contamination and ensure the desired energy is achieved, and also to deflect the beam 90° into the experimental hall towards the OSCAR/SiRi target station.

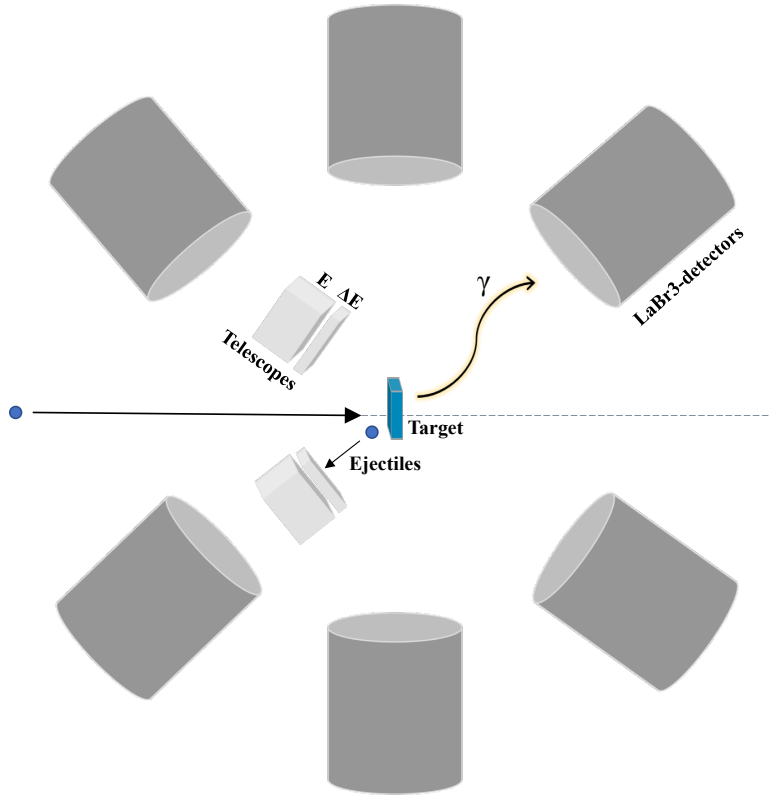

Figure 3.2: Schematic drawing of the detector setup of the ^{68}Zn(p,p$\prime$) experiment at the Oslo Cyclotron Laboratory (not to scale).

3.1.1 Cyclotron

Invented in 1932 by Lawrence and Livingston [51], the cyclotron has become one of the most useful particle accelerators in both nuclear and particle physics. A cyclotron induces a nearly homogeneous magnetic field $\vec{B}$ between two parallel magnetic poles. If a charged particle is introduced to this magnetic field with some velocity, it will gain an acceleration according to Eq. (3.1). This acceleration will be perpendicular to the radial distance, as the force F is always pointing towards the centre of the magnetic field, and get an acceleration $a = \frac{v^2}{r}$, and a corresponding frequency ω as shown in Figure 3.3. A sketch of a cyclotron is shown in Figure 3.4, where two "D"-shaped "dees" are alternating the voltage applied to the beam at a high frequency. The OCL cyclotron consists of four such dees. Two of the dees are connected to oscillators, and connected to each other in such a way that they can be run either in phase or anti-phase depending on particle type and desired energy. These modes are called "push-push" and "push-pull", respectively. The other dees are connected to earth ground.

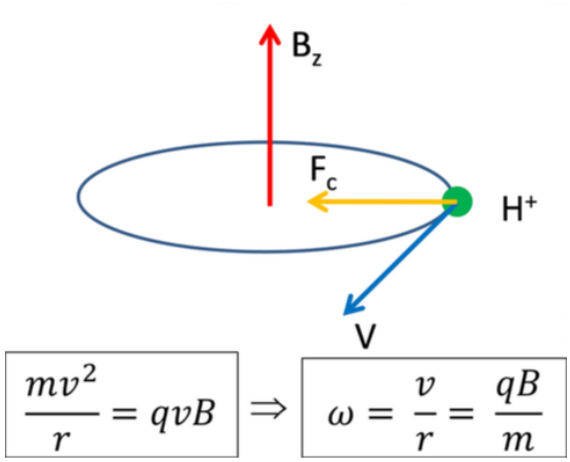

Figure 3.3: At first order, the speed of a particle in a cyclotron is independent of radius or energy, and rotates at constant frequency ω. Figure taken from Ref. [52].

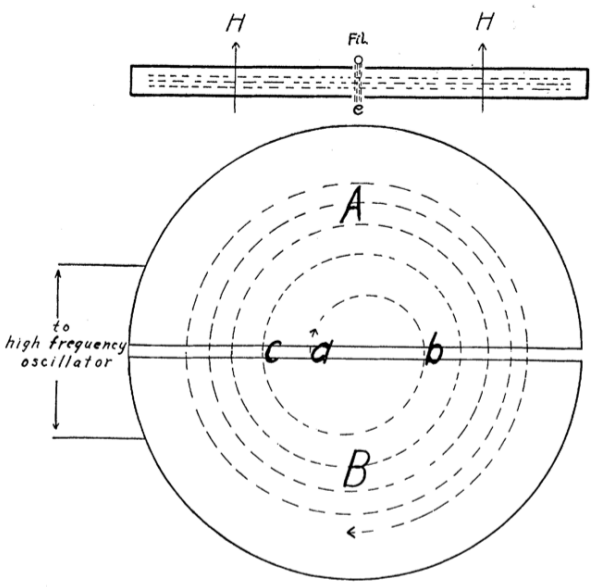

Figure 3.4: Acceleration of ions using a cyclotron as illustrated by the inventors E. Lawrence and M. Livingston. Figure taken from Ref. [51].

The magnetic field has an angular dependency that enables focusing of the beam, to correct for the relativistic increase in mass. The field increases as the radius r from the center of the cyclotron to the particle position increases. To create such a magnetic field, more magnetic dipoles are necessary. Correction coils are used to purposefully create such a slightly in-homogenous magnetic field, with a slightly stronger field at the outer edge to compensate for relativistic mass effects. We need to take such relativistic effects into account when the accelerated particles are moving at velocities higher than $0.1c$, where c is the speed of light.

The resulting beam from the cyclotron has some energy spread, so that the beam straight from the cyclotron can be used for experiments where the energy precision is not of importance and high intensity is advantageous. Such experiments are for instance isotope production for medical application research. For this experiment however, we need to send the beam through the analyzing magnet, which bends the beam using a magnetic field to select particles of a given energy. The beam will be sent through a slit of width s. The precision p of the beam momentum, and relative spread of its momentum is then given as

$$\frac{\Delta p}{p} = \frac{s}{r} \tag{3.3}$$

where r is the bending radius of the particle path moving through the analyzing magnet, and for our setup this spread is about 0.1 %. After our beam has been given a more narrow energy range, several quadrupole magnets are used to focus it, see Fig. (3.1). Lastly, it travels towards the area where the target is located along with the γ-detectors OSCAR and the particle telescope SiRi.

3.1.2 Target Foils

The target was a ^{68}Zn metal foil from Trace Sciences International. It is 99.23 % enriched, and weighs 10.01 mg. The area density is 3.5 mg/cm^2, and the dimensions are 1.3 cm $\times$ 2.2 cm. The target was carefully picked up using tweezers and glued to the target holder, and additional screws were used to make sure it stayed put. Alongside the zink, a target of natural Si was used for calibration purposes, as this target has well known γ-lines which can be easily identified. The target holder was then placed inside the target chamber in the middle of OSCAR. The incoming protons that undergo inelastic scattering when reaching the target, will be emitted at an angle while leaving a target nucleus excited. The target then undergoes emission of one or several γ-ray's. We are therefore interested in measuring both the outgoing proton using SiRi, and the outgoing γ-rays using OSCAR, and use the information of the two together to extract the level density and the γ-ray strength function of ^{68}Zn. The experiment was successfully run for two days, with help from the OCL group to take shifts. This allowed us enough time to gather good statistics, with over 13 million proton-γ coincidences.

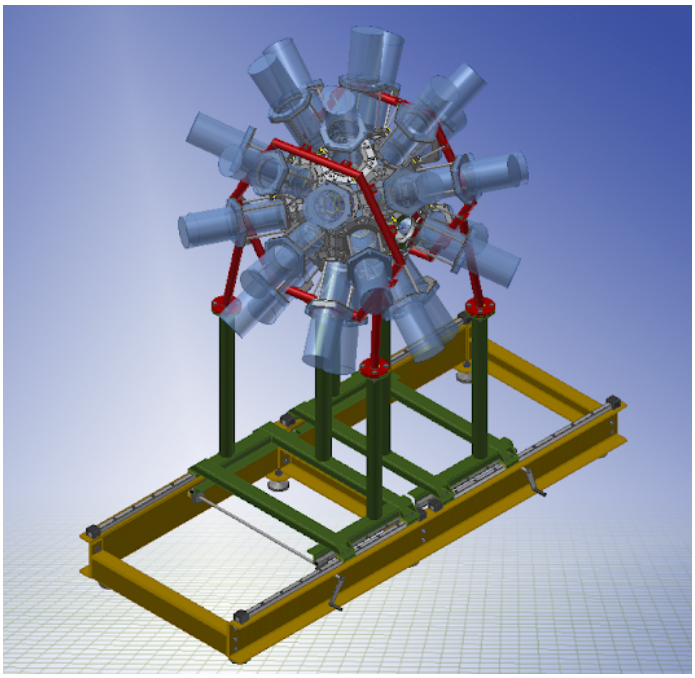

Figure 3.5: OSCAR, the new scintillation array at OCL. A number of LaBr3:Ce detectors are mounted spherically around the target to count γ-rays. Figure acquired from Ref. [53].

3.1.3 γ-ray Detector Array: OSCAR

Before a very recent upgrade at the OCL, similar experiments were performed using CACTUS, a NaI(Tl)-detector array. In 2001 an alternative crystal scintillator was developed, as $LaBr_3$:Ce- crystals were produced and proved to have an improved energy resolution, fast timing properties and high detection efficiency also for high-energy γ-rays [54]. One potential problem is that lanthanum contains radioactive ^{138}La, and lanthanum is also chemically similar to ^{227}Ac, which can be mined together with it and has a long half life. A radioactive background will therefore always be present, and must be accounted for. It also sets limitations on detection of low levels of radiation.

The γ-ray detector array OSCAR was a new addition to the Oslo Cyclotron Laboratory, with partial implementation, in the fall of 2017, with 21 detectors in place. The ^{68}Zn experiment was run in January 2018, being one of the first new experiments using this array. OSCAR consists of LaBr3:Ce-detectors positioned spherically around the target (see Figure 3.5) to be able to capture outgoing γ-rays at all angles. Since what we are studying is compound reactions, the de-excitation γ-rays will be sent out in all of the 4π solid angles. The scintillation material emits electromagnetic radiation (light) with wavelengths in the visible and ultraviolet spectrum, when the γ-rays interact with the crystal.

Each of the detectors are mounted to a photomultiplier tube (PMT), specifically a Hamamatsu R10233-100, to make the signal from the γ quant detectable electronically. This is done by converting the photons into electrons, and then amplifying the signal by scattering them onto a chain of dynodes, where the electron's kinetic energy is converted into several electrons with lower kinetic energy. This is shown in Fig. (3.6). After the amplification in the PMT is complete, the electron current, which is proportional to the energy of the incoming γ-ray, is measured.

The LaBr3:Ce-detectors are large volume 3.5 inches $\times$ 8 inches detectors. They can be placed in three distances from the target: 16, 22 and 35 cm. For this experiment we used the 22 cm target-detector distance, and the efficiency of OSCAR for different energies at this distance is presented in Figure 3.7. Active voltage dividers were used to reduce non-linearities. The PMTs get saturated because of the high light yield of the $LaBr_3$:Ce crystals, which causes this non-linearity. A LaBrPro box from Milan is used as a shaper and amplifier of the signal.

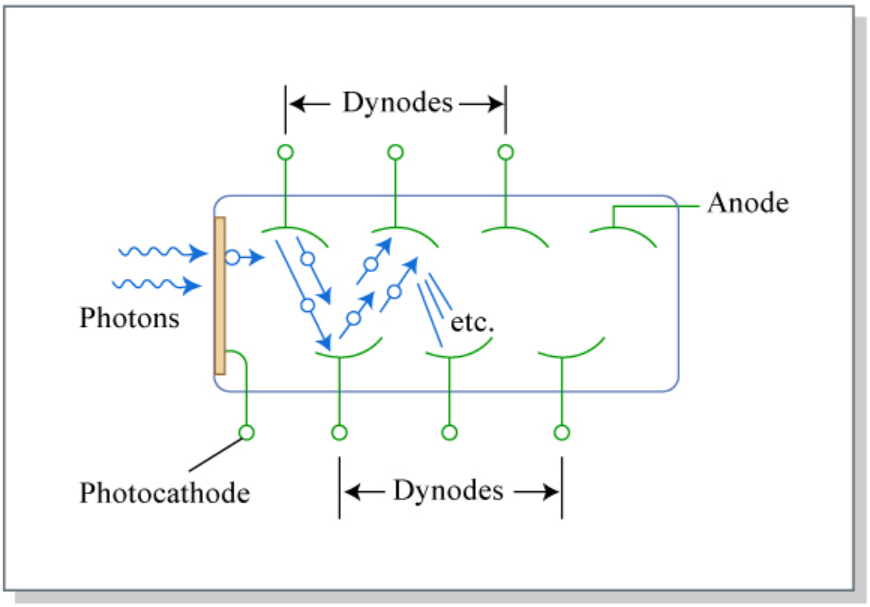

Figure 3.6: Schematic of a photomultipler tube (PMT): photons strike photocathode at one end; a sequence of dynodes lead toward an anode at the other end. Figure taken from Ref. [55].

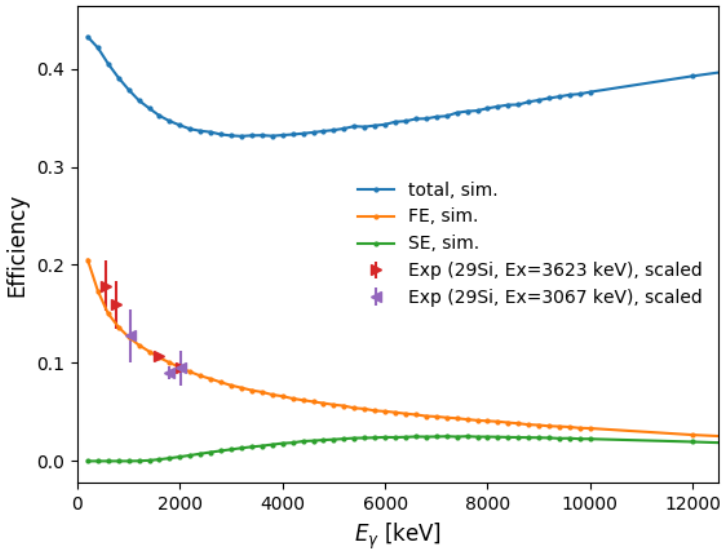

Figure 3.7: Efficiency of OSCAR at 22 cm target distance. Figure taken from Ref. [56].

3.1.4 Particle Telescope: SiRi

SiRi, the beautiful instrument pictured in Figure 3.8, consists of eight silicon particle telescopes. In this experiment, we placed them in backward angles at 126-140° with respect to the incoming direction of the beam, and at a 5 cm distance away from the target. Each telescope consists of a 130 μm thick front counter: the ΔE-detector, and a 1550μm thick back counter: the E-detector. The main purpose of SiRi is to measure the particle energy, while in addition, the front and back detector allow us to identify the type of charged particle we are looking at. Therefore, SiRi enables us to produce ΔE/E plots resembling "bananas" (often called banana plots). There is also a 10.5 μm thick aluminum foil in front of the ΔE in order to reduce the amount of δ-electrons entering the detector. The complete detector setup with the target and SiRi at forward angles is illustrated in Fig. 3.9. In Fig. 3.10 the layout of the segmented front detectors is shown.

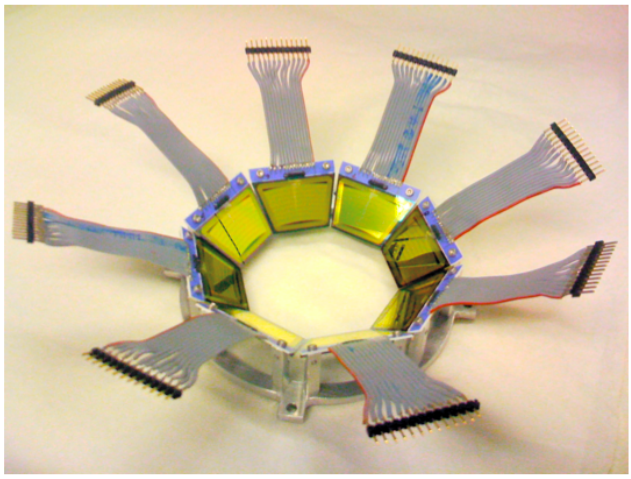

Figure 3.8: SiRi: Silicon particle telescope modules mounted on a supporting structure. Picture taken from Ref. [57].

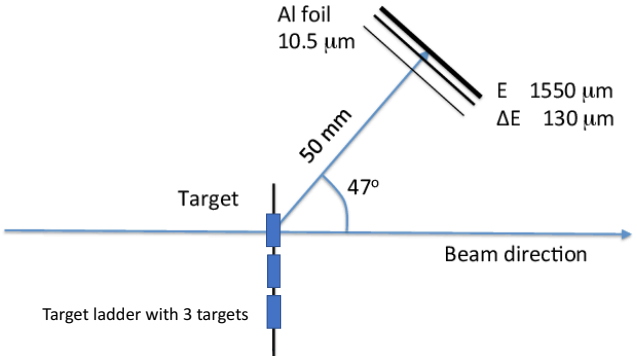

Figure 3.9: A $\Delta E/E$ detector module shown at $\theta = 47°$ with respect to the beam direction of motion. To reduce δ-electrons, aluminum foil with thickness 10.5 μm is placed in front of the detectors. Figure taken from Ref. [57], and slightly modified with a target ladder with three target holders.

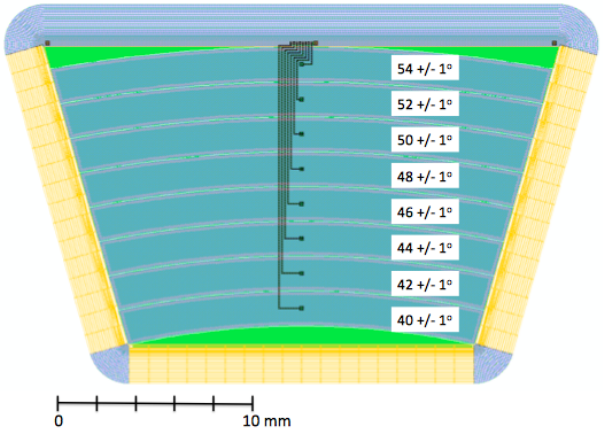

Figure 3.10: Layout of the front Δ E detector, with curved pads for specific angles. Figure taken from Ref. [57].

Charged particles of different mass deposit a corresponding different energy in ΔE. The higher the charge, the more energy is deposited in the material. A light particle of low charge, like protons, would be depositing a velocity dependent amount of energy. The energy loss dE of a particle passing a distance dx through a medium is given by the Bethe Block formula [58],

$$-\frac{dE}{dx} = 2\pi N_a r_e^2 m_e c^2 \rho \frac{Z}{A}\frac{z^2}{\beta^2}[ln(\frac{2m_e\gamma^2c^2v^2W_{max}}{I^2} - 2\beta^2)], \tag{3.4}$$

where N_a is Avogadros number, m_e the electron mass, r_e the classical electron radius, c the speed of light in vacuum. For a given material that the particle is passing through: ρ is the density, Z the atomic number, and A the mass number. The charge is denoted as z, in units of e, $\beta = v/c$ and the Lorentz factor $\gamma = \frac{1}{\sqrt{1-\beta^2}}$, I is the mean potential of excitation, and W_{max} the maximum energy transfer in a collision, as the charged particle is decelerated by giving off energy to the electrons in the detector medium through Coulomb interactions.

By combining energy measurements of the ΔE and E-detectors we get a higher energy resolution than by looking at these detectors separately. The total energy of the particle can be defined, and also which type it is based on whether the energy was deposited in the ΔE or E detector. The range travelled through the detector material, as a function of energy, is defined as $R(E)$:

$$R(E) = E(a_1 + a_2E) + \frac{a_3}{(E + a_4)}, \tag{3.5}$$

where E is the kinetic energy of the particles, and the a's are free parameters. Based on the spectrum of $R(E)$ the relation of total distance passed vs the distance passed in the E-detector is:

$$R(\Delta E + E) - R(E) = d_{front} \tag{3.6}$$

to define the thickness spectrum. The thickness is defined as d_{front}. In Figure

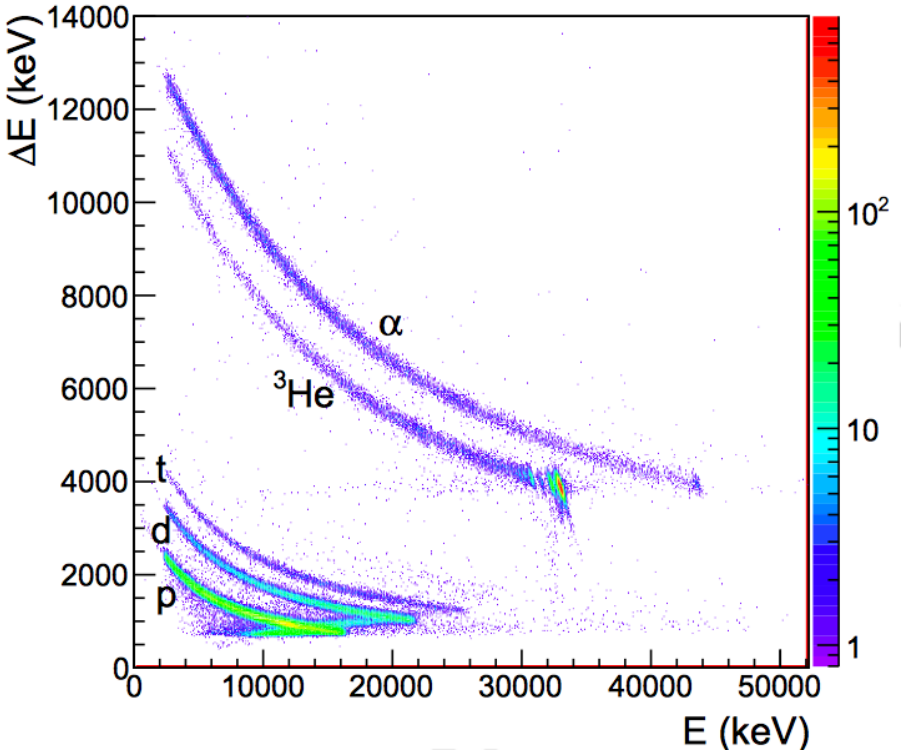

Figure 3.11: A $\Delta E/E$ plot for $\theta = 50°$. In ROOT called b1f5. Figure taken from [57], where the ^{112}Cd + ^{3}He reaction with SiRi in forward angles (40-54°) is studied.

3.11 a plot of deposited energy in the front counter as a function of energy deposited in the back counter is displayed. The different particle types are distinguished by the positioning of the bananas: the lowest charged particles in the lowest bananas. In this case, the protons p with charge $q = 1$ are in the lowest curve, and the He particles with $q = 2$ in the uppermost curve. The program Qkinz [60] can calculate the position and shape of the banana for a given charged particle, coming out at the corresponding ejectile angle.

3.1.5 Signal Processing

The signals from SiRi are processed by pre-amplifiers of the type Mesytec MPR-16. Four pre-amplifiers handle 16 ΔE strips each, for the 64 ΔE detector strips. Another pre-amplifier handles the eight E-detectors. The output is differential signals, which get transmitted to Mesytec STM-16 modules which contain timing- and spectroscopy filter amplifiers, and also a leading-edge discriminator [57].

A logic circuit filters out irrelevant signals to minimize the waste of server space. The discriminator outputs the logical "OR" signal of the ΔE-detectors, providing the master gate of the data aquisition, which is about 2 μs long. As a

detection is made in one of the LaBr3:Ce-detectors in OSCAR, a STOP signal is sent. These events in reality happen in coincidence, but the stop signal is delayed by ≈ 350 ns to allow a small time frame where measurements are made. A sorting of true coincidences will be performed offline. The analog signal from the shapers is converted to a digital signal, using ADC's from CAEN (mod. 785) and Mesytec (MADC-32). The time to digital signals are converted by a CAEN (mod.755) TDC. The data aquisition is placed in a VME module rack, and being controlled by software running on a CES8062 CPU. Using a CAEN VME USB module (mod. 1718), the data is transferred to a Linux computer [57].

3.2 Calibration of (p,p′)-data

Both the detector material and the electronics used can be sources of error propagation. Calibration is therefore a crucial step in making measured data aligned with what it in reality represents. The calibration is performed using the software ROOT [59].

3.2.1 SiRi calibration

The response of the SiRi detectors is linear, and the energy of the particle in our measured spectrum will follow

$$E(x) = a + b \cdot x, \tag{3.7}$$

where x is the channel number, a is the shift and b the energy dispersion per channel. Our goal is to determine a and b such that the peaks in the energy distribution $E(x)$ match the theoretical peaks estimated by Qkinz [60] for both the ΔE and E axis.

In the calibration I used the program Qkinz [60] to simulate experimental runs at OCL. The program takes inputs like the beam type and energy, target type and thickness, and allows you to choose backward or forward angled SiRi positioning. After applying these presets, the program can be used to determine the energy deposited in the different SiRi strips. The calculation is based on the Bethe Block formula (3.4).

With eight back counters, and eight front counters, this results in 64 back-front combinations having to be calibrated. A few spread out energy states must be used to make sure I not only calibrate the one point of the spectrum, but correct for a gain and shift from the detectors across the spectrum, from low states to high energy states. The ground state in ^{68}Zn was used, as well as the fourth excited state in ^{28}Si. Using these two well known states, I compared the position of the blobs in the ΔE / E plots to the actual value for the energy (theoretical value calculated by Qkinz). This correction gave us a shift and gain to calibrate the particle spectra for each $\Delta E - E$ combination.

The fourth excited state of ^{28}Si was chosen as the high calibration point as it is a higher energy state with a good amount of counts in the experimental data (see Fig. (3.13)). From this figure, it may seem like the fifth excited state has even better counts, however when looking at the Qkinz-plot and energy values in Fig. (3.14), one can see that the 5th, 6th and 7th excited state are very close to each other in the area of the peak in the experimental result, which makes none of them a good calibration point as I do not know the population of each state. The same overlap occurs for most higher states, as it is a general feature of the nucleus that the higher the excited energy state is, the closer the levels will generally be to others. Looking at the fourth excited state in Figure 3.14, this seems to have a distance larger than the energy resolution to other states, and therefore it is a good choice for calibration. By applying this technique, the calibrated ΔE/E plot for one ΔE-E combination seen in Fig. 3.12 was determined.

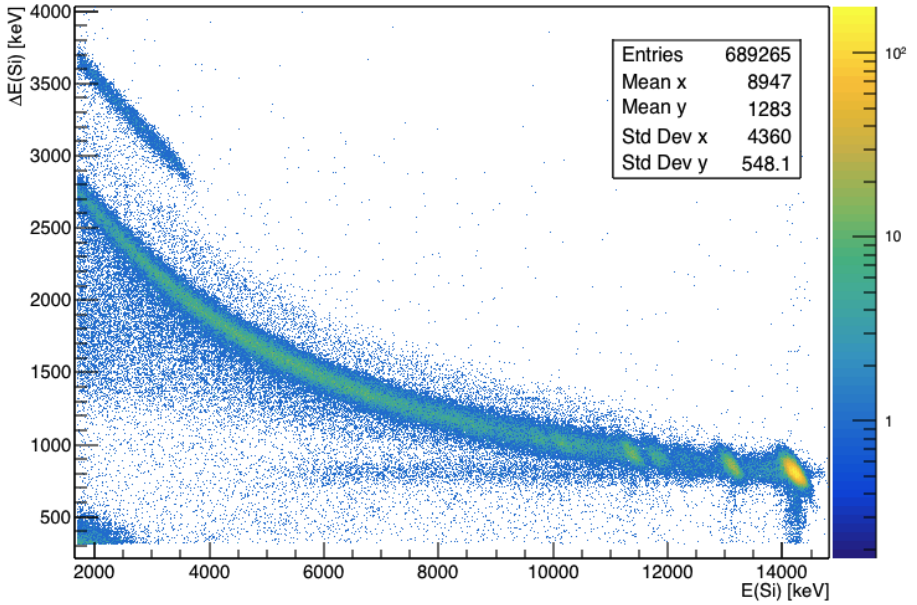

Figure 3.12: ^{68}Zn data, calibrated to correct theoretical energy peaks. The plot shows the energy deposited in the front counter ΔE, for the angle $\theta = 140°$ versus the energy deposited in the back counter E of SiRi in the first strip of the first back detector: b0f0 in ROOT. The lower banana is protons, and the small banana above is deuterons. The lower right, brightest peak is the ground state, and is used in the calibration.

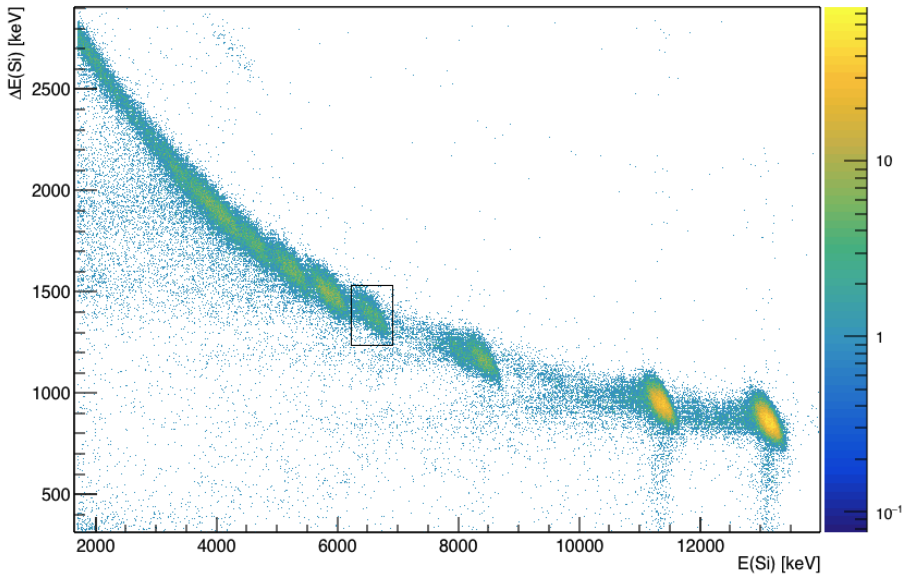

Figure 3.13: ^{28}Si data collected in the first strip for the angle $\theta = 140°$(front detector) of the first back detector. A plot of the energy deposited in the front counters ΔE, versus the energy deposited in the back counters E of SiRi. The fourth excited state is inside the black square, and was used for calibration.

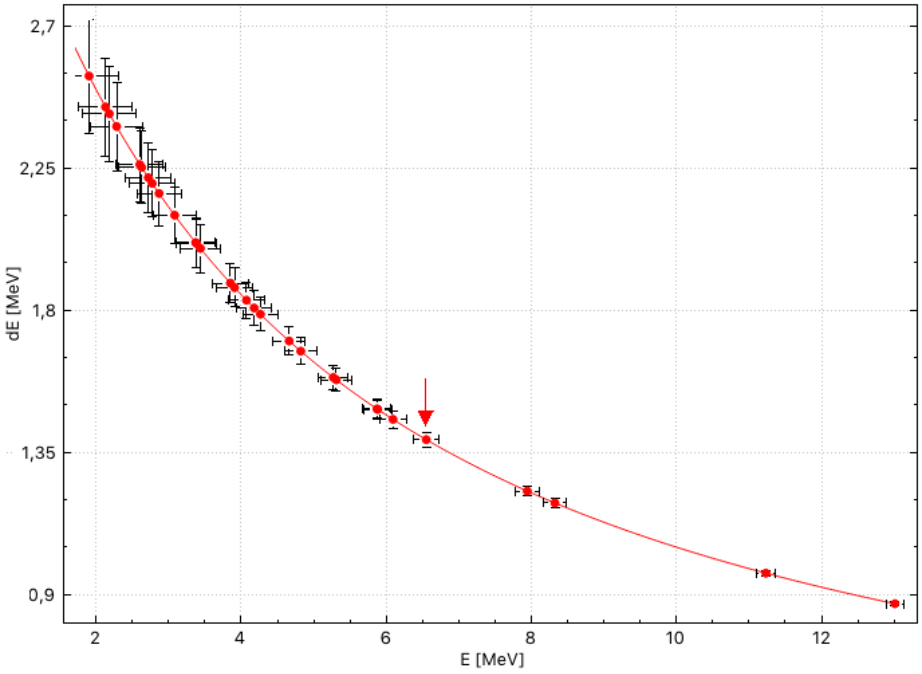

Figure 3.14: ^{28}Si Qkinz-calculations for the in the first SiRi strip (front detector) of the first SiRi back detector, using 16 MeV protons and 4 mg/cm^2 thick target in backward angles. The fourth excited state is under the arrow, and was used for calibration.

Ejectile Gating

Since I am interested in a specific reaction channel with a certain outgoing particle type, I wished to exclude the upper ΔE/E curve in Figure 3.12 that is due to outgoing deuterons, so that I only extracted the data for protons. The thickness of the ΔE detectors was calculated using the Bethe Block equation, see Eq. (3.4), and the range curve for protons in the Si material, using data from the experiment, Eq. (3.5) and Eq. (3.6). This resulted in a normal distribution around 130 μm, see Figure 3.15. The smaller peak implies a lower apparent thickness, but this is due to electrons. The small peak at around 210 μm is due to deuterons. In order to avoid these ejectiles, I gated on the proton-peak and used only coincident γ-rays to these measurements as our valid reaction data.

3.2.2 OSCAR calibration

γ-energy Calibration

In order to calibrate the energy spectrum of the γ-ray detectors, I compared the experimental peaks in our data to known theoretical values of energy levels for ^{68}Zn [61] and ^{28}Si [62] for the excitation energy E_x in the target material and γ-ray energies E_γ resulting from the de-exitation. The peak mean values were found by estimating a Gaussian curve to the experimental peaks and extracting the mean value. Using a peak in the lower region and more peaks in the higher region allowed us to adjust the whole spectrum correctly, not just correctly for one region. This process was done for each individual detector for every calibration peak. The resulting spectrum after a linear calibration is shown in Figure 3.16, and has nicely aligned energy peaks for all detectors, and the peaks are corresponding to actual experimental values. Slight variations occur, and are visible in Figure 3.16, especially in the high energy-regions, and a tendency towards non-linearity can be seen due to saturation of the PM-tubes. However, the variations will still be within the detector resolution uncertainty, and the calibration is found to be satisfactory for data-analysis. Seeing as the centroids can be quite precisely determined, it is therefore a good idea to in the future explore quadratic or other non-linear calibration techniques for OSCAR. This is currently being looked at by scientists in the Oslo group.

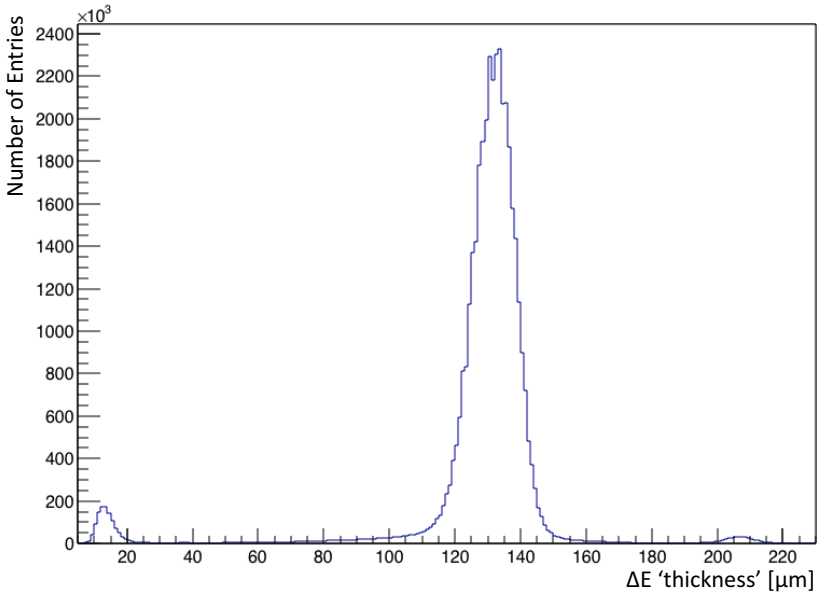

Figure 3.15: Apparent thickness of the ΔE detector for protons, based on calculations from the data, using the range curve of protons in Si.

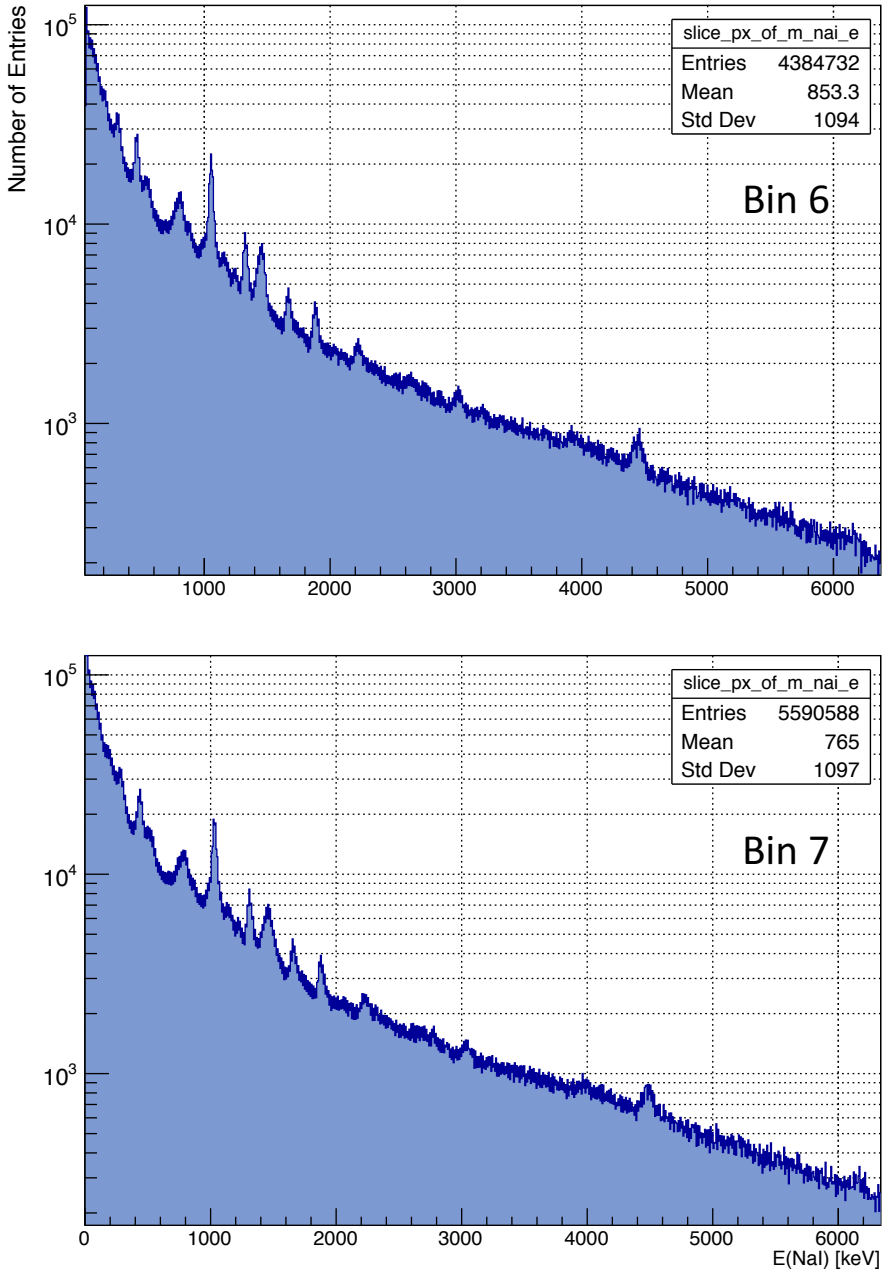

Figure 3.16: γ-detector alignment after calibration for detector 6 and 7 of the ^{68}Zn run (As an example pair to demonstrate, all other detectors have similar profiles). The peaks are well calibrated, yet better for lower energies than higher energies.

γ-time Correction

The time spectrum is dependent on energy due to the threshold, which decides what is noise and what is valid data. Using Leading Edge discriminators for this set threshold will cause a phenomenon is called *walk*, and it manifests itself in our data such that signals of low amplitude will appear to be happening after a simultaneous signal of higher amplitude. This is unfortunate when looking at coincident events. Due to a favorable trait of the new $LaBr_3$:Ce detectors and the fact that the ΔE detectors were used to generate the start signal, the timing was already very good. However I still needed to apply a slight adjustment to the lower energies (see Figure 3.17). By doing a polynomial fit to the curved shape shown in Figure 3.17, using the function [57]

$$t(x) = 200 + a + b/(x + c) + d \cdot x, \tag{3.8}$$

where t is the time channel and x the energy channel. 200 is an arbitrary number representing the position of the prompt time peak, while a, b, c, d are coefficients determined by fitting the polynomial to the curve. Finding these coefficients can take several fits, until a straighter time spectrum is achieved, see Figure 3.17. In Figure 3.18, small peaks around our time peak are visible, which are due to neighbouring beam bursts with a spacing of the cyclotron frequency. By gating on a single small peak by the same interval (here we set the peak to be within 194 and 206 as shown in Figure 3.18), I subtracted the corresponding spectrum.

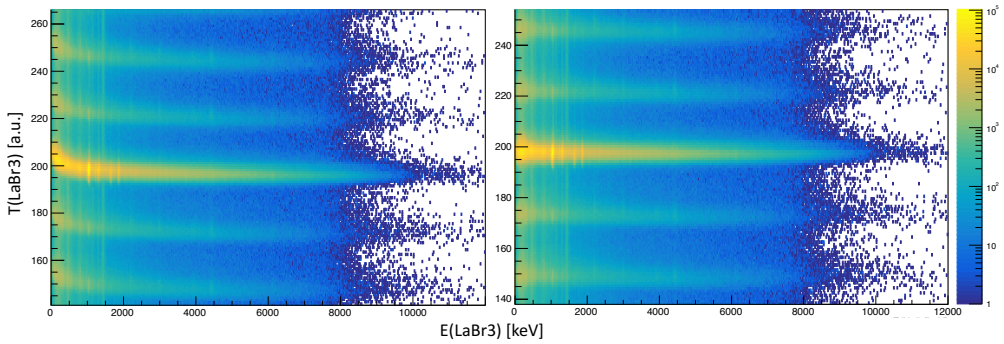

Figure 3.17: The uncorrected time spectrum (left), where one can see a slight bend at low energies, which must be aligned with the rest of the data. and corrected, straightened time spectrum (right), using a polynomial fit to the curve of the original time spectrum. Small peaks are still present around our time peak, which are due to random coincidences of background radiation.

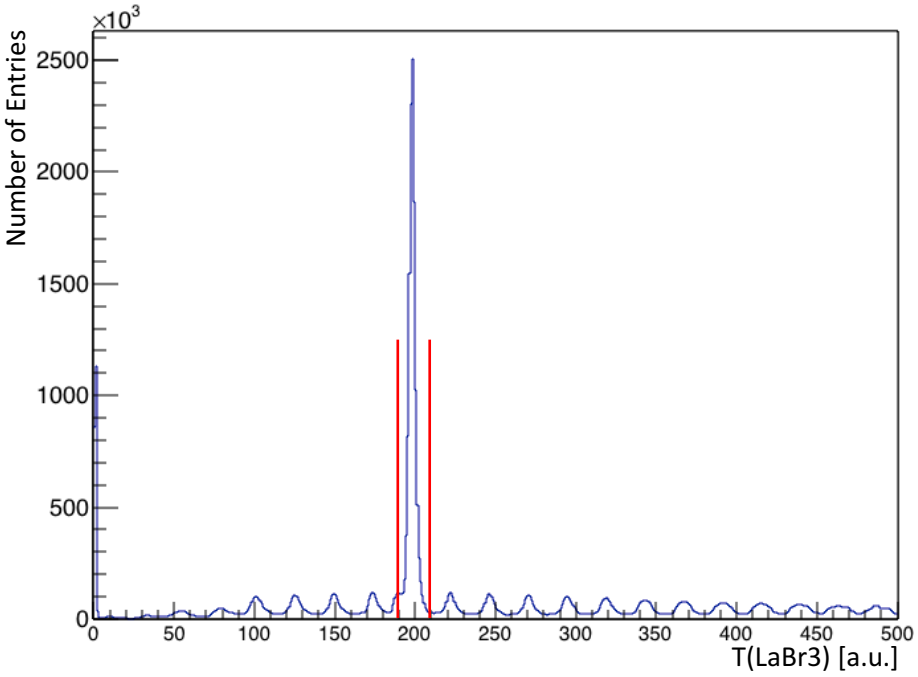

Figure 3.18: The corrected time spectrum, projected onto the y-axis. The gates set at 194 and 206 for the background correction are shown.

3.2.3 Finished Calibration

Now that I had trustworthy coincidences to work with, I produced a coincidence matrix which expresses how the γ-ray energies E_γ relate to the excitation energy E_x of the nucleus. Since the energy of the incoming proton and also the energy of the outgoing proton is known, I could calculate this excitation energy that the nucleus obtains during a collision. The resulting matrix is represented in Figure 3.19, and this is the data representation I worked with as input into the process of the Oslo Method.

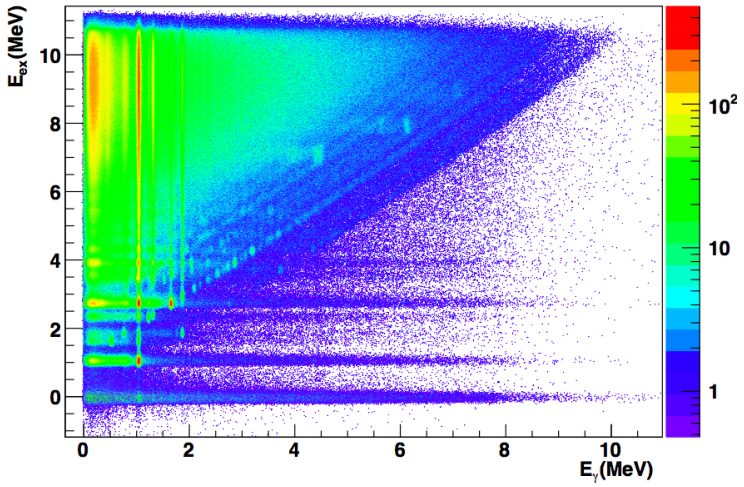

Figure 3.19: The coincidence matrix of excitation energy vs γ-energy after finished calibration, which will be unfolded using the Oslo Method. The peaks at around $E_\gamma = 4.439$ MeV and 6.130 MeV are traces of carbon and oxygen, which were useful to check our calibration.

3.3 The Oslo Method

The Oslo Method uses data from a light-ion reaction: usually (p,p$'\gamma$) or similar, to extract the nuclear level density and γ-strength function for the residual nuclei. This is useful input when calculating reaction cross sections and reaction rates to better understand heavy-element nucleosynthesis. One of the most important assumptions made in the Oslo Method is that the Brink hypothesis [49] holds, see Section 2.4. The Oslo Method Software [63] was used to perform the data treatment, and the mentioned programs (like MAMA) can be found in this repository.

3.3.1 The iterative unfolding method

In Ref. [64] the iterative unfolding method is thoroughly discussed, but I will give a brief explanation of it here. As the OSCAR detectors have a finite volume, a signal disturbance will occur from reactions within the detector material. My data must be filtered through an unfolding process to achieve a true

full energy γ-ray spectrum. I need to find the *response function* describing the way the detector distorts the incoming γ-ray, as our data will be tweaked by its resolution and efficiency. A variety of processes manifest themselves in our observed spectra: these include Compton-scattering, photoelectric effect, pair production, annihilation and backscattering- γ-rays. Which of the processes will dominate is highly energy dependent, as the cross section for the various interactions change as a function of energy. It also depends on the detector material.

In order to perform this unfolding and estimate the correctly shaped spectrum, I used the iterative folding method. By normalizing and smoothing the results, the detector response was subtracted from the true full energy γ-ray spectrum. I used it on a LaBr3:Ce-detector data set, but it can also be used for other detectors like NaI, Ge, BGO, CsI or other materials given that the response functions are known. The iterative unfolding method used in the Oslo method works by "guessing" a correct unfolded spectrum (by initially guessing our RAW-spectrum as the correct one), and thereafter iteratively folding it. The method itself is assumed to be very safe, even if fluctuations may occur from one channel to the next. The action of folding is quite fast and simple, so doing it many times is not a daunting task for a modern computer to handle. One will need to have a very precise determination of the response matrix R, which can be found by using spectra from isotopes with well known mono-energetic outgoing γ-rays, and/or from simulations.

After having measured spectra of monoenergetic γ-lines for the LaBr3:Ce detectors, an interpolation between these measured points is necessary as there is only a limited amount of well known mono-energetic sources. I separated the Compton background from the rest of the reactions/peaks in the spectra, and interpolated between the peaks by assuming a Gaussian distribution is smoothing each peak. For the Compton background, I interpolated between channels corresponding to the same scattering angle θ. I also made sure the probability of every process in each channel was normalized to 1.

R_{ij} is defined as the response in channel i when γ-rays hit the detector with an energy corresponding to channel j. Each response function is normalized: $\sum_i R_{ij} = 1$. The folding can be expressed in general as

$$f = \mathbf{R}u, \tag{3.9}$$

where f is the folded spectrum, and u is the unfolded spectrum. I initially used our raw-spectrum r as a guess for the unfolded spectrum u^0, which is the normal assumption (which will not be true), but the procedure is not sensitive to the choice of starting trial function. One performs typically 20 iterations of this operation from there gradually approaching a better guess. The first guess results in the back-folded spectra $f^0 = Ru^0$. The next guess will be $u^1 = u^0 + (r - f^0)$, which will be giving us $f^1 = Ru^1$, and continue, until $f \approx r$, which is typically achieved after 4-5 iterations.

The resulting and final u-spectrum is used to remove background disturbance from Compton scattering and pair production, in what is called the Compton subtraction method. The resulting u-spectrum from the unfolding contains

large fluctuations from one channel to the next (even for few iterations, but these fluctuations will increase with the number of iterations). One solution would be to smooth out the noise, but this could lead to loosing information about true states as if they were noisy resonances. Therefore the Compton subtraction method [64] was developed to subtract counts from the solution based on physical arguments about the detector response. This way, the counts corresponding to Compton scattering, annihilation and single and double escape are distributed back into the full energy peak. Thereafter, the smoothed Compton contribution is estimated to the folded spectrum, before being subtracted from the original unfolded spectrum. This results in a new spectrum

$$v(i) = p_f(i)u_0(i) + w(i) \tag{3.10}$$

where $p_f u_0$ is the full energy contribution, and w is the sum of single escape (u_s), double escape (u_d) and annihilation (u_a):

$$w(i) = u_s + u_d + u_a, \tag{3.11}$$

A Compton spectrum, including only the contribution from Compton scattering can be defined as the spectrum with no Compton contribution at all ($v(i)$), and subtract it from the experimental raw spectrum $r(i)$ as $c(i) = r(i) - v(i)$. This Compton spectrum will contain strong oscillations, as it depends on the unfolded spectrum u_0 from Eq. (3.10). According to the method presented in [64], $c(i)$ should be a slowly varying function of energy, and therefore this Compton spectrum can be smoothed without loosing important information. After smoothing $c(i)$, we can subtract all the disturbances from the raw spectrum in the following manner:

$$u(i) = [r(i) - c(i) - w(i)]/p_f(i), \tag{3.12}$$

with p_f being the probability of the full-energy peak. Lastly the γ-ray energies varying efficiency (see Figure 3.7) are corrected for: $U(i) = u(i)/\epsilon_{tot}(i)$, leaving us the final unfolded spectrum U. This method converges rapidly, and maintains the original shape of the spectrum.

As input for the unfolding I sent in the coincidence matrix (see Figure 3.19), which is the raw matrix. I also used MAMA to create a response matrix using the known response function for OSCAR, but during our unfolding I made response functions with 10 times less FWHM than experimentally known, to avoid negative resonances around the full energy peak [65].

The unfolding was performed using *MAMA*. For high energy γ-rays above 2 MeV, I set the lower limit at 500 keV. Below, the limit is 1/4 of the full-energy. Full-energy is taken from the upper unfolding limit. The iterations terminated when the folding of the unfolded spectrum is equal to the raw spectrum, and the result is plotted in Figure 3.20.

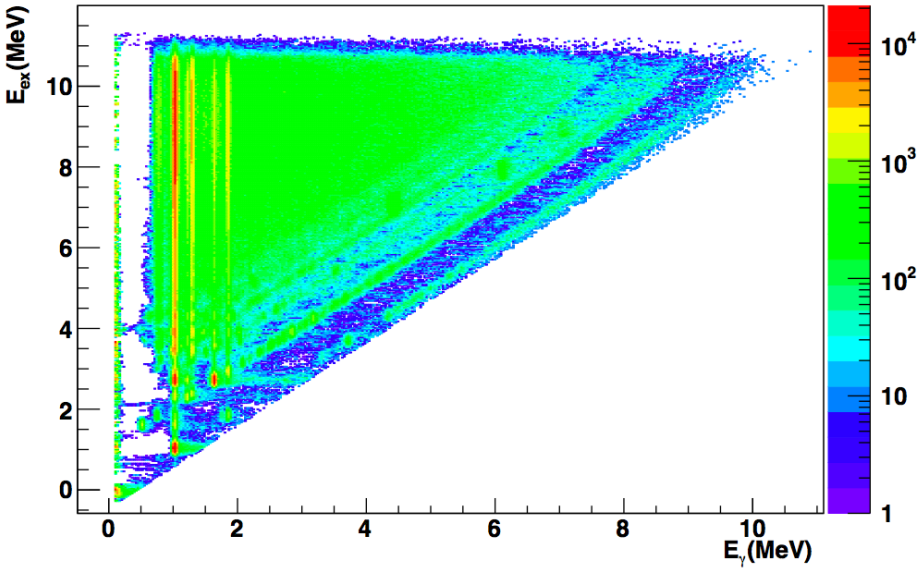

Figure 3.20: The unfolded particle-γ matrix for ^{68}Zn. The number of counts are expressed by a color spectrum from few counts (blue) to most counts (red).

3.3.2 Troubles in the Unfolding Method

To study how well the unfolding works, we look for the familiar energy lines in the spectrum and expect a lot of counts in those areas, and little in the others. We also have to look carefully whethere too many negative counts were removed, as this can destroy valuable information. This can be corrected for by isolating areas affected by such treatment, if it is obvious that this is a fault due to the unfolding and subtraction. However, the less corrections of this manner made is better to keep the true information from the experiment as it originally was. As seen in the coincidence matrix even after it has been processed in the unfolding, counts are visible between the first excited state and the ground state, as though there is a state being populated in this area. Since this is already present in the raw-matrix, we wanted to compare the raw spectrum to a simulated spectrum to see if maybe the simulations of the detector response could be to blame. The simulations were performed by G.M. Tveten. Another thing would be contaminants causing the state to be present, but such contamination is usually by neighbouring isotopes. Checking for ^{64,66,67,69,70} Zn there is none having a significant state in the area of 500 keV. There is also a known carbon/oxygen-contamination which will not contribute to this effect as they have way higher (4000 keV and above) states only. What we concluded was that even when the unfolding process is believed to correct for the background leaving us with the true value in the full energy peak, we see in both the raw, the unfolded, the first generation and the simulation spectra, that there is a significant contribution of 511 keV single-escape γ-rays both from the detector material itself and neighbouring detectors sending this out. See Figure 3.21 and 3.22. This problem has probably been present earlier even if we did not see it, but due to OSCARS higher energy resolution of than our previous detector ar-

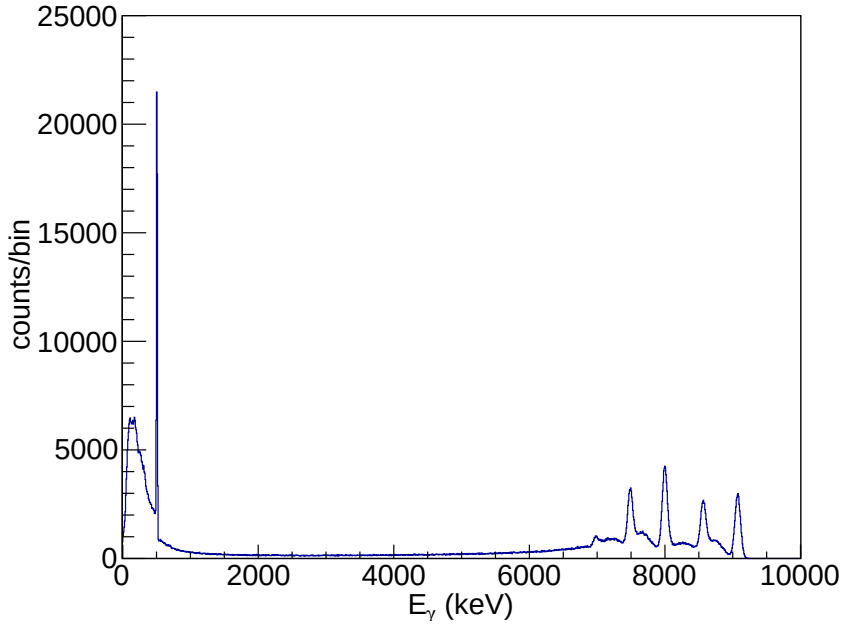

Figure 3.21: A simulated spectrum of the high energy γ-rays from ^{68}Zn for two energies, one around 7000 and one around 9000 keV. We see that the 511 keV disturbance affects both of these states, and this has to be the unwanted counts we see between the diagonals in the unfolded coincidence matrix as well. The first high peak on low energy also shows the amount of 511keV photons we are dealing with is significant. Figure acquired from Ref. [53].

ray CACTUS, it is probably now easier t spot this fault. There is an issue in the unfolding method, causing the contribution of the 511 keV photons to remain as actual states, and since it is exactly halfway between the ground state and the first excited 1077 keV state, the unfolding is probably tricked even more than normal to believe that this could be a possible path for the γ-rays to cascade.

Luckily the contribution from these 511 keV photons will not alter the level density or the strength function in a visible way, which as shown in chapter 5 ended up being decent calculations. The level density is still very smooth, and we can still trust the method to be working quite well. Nevertheless, it is worth taking note of, and being aware of this.

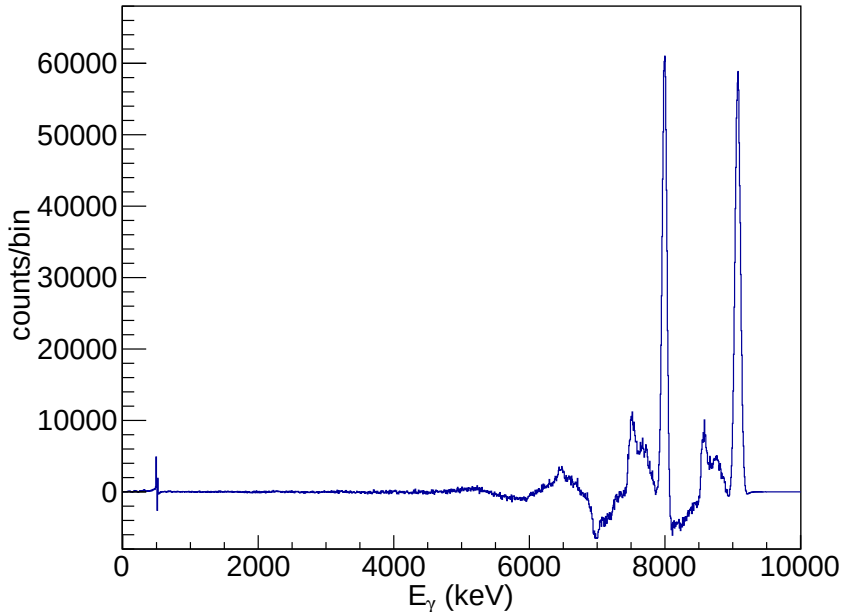

Figure 3.22: A simulated and unfolded spectrum of the high energy γ-rays from ^{68}Zn for two energies, one around 7000 and one around 9000 keV. We see that the 511 keV disturbance affects both of these states, and this has to be the unwanted counts we see between the diagonals in the unfolded coincidence matrix as well. Figure acquired from Ref. [53]

3.3.3 The First-Generation Method

After the unfolding, the next step is to filter out the first γ-rays sent out of the excited nucleus. It is impossible to separate these directly from our original, total γ-ray spectrum as the timing of the detector and the data acquisition is simply not good enough. To get around this, we use the iterative first-generation method, which extracts a first generation matrix from our data [66]. The method is also well explained in [67].

Let $FG(E_\gamma)_{E_x}$, the distribution of γ-ray decay intensity from a given excitation energy E_x, as a function of γ-ray energy E_γ, denote the first generation γ-ray spectrum. In general the nucleus will decay from E_x and down to the ground state, maybe involving several states, through a cascade of γ-rays which makes up the *total* γ-ray spectrum $AG(E_\gamma)_{E_x}$:

$$AG(E_\gamma)_{E_x} = FG(E_\gamma)_{E_x} + \sum_{E'_x<E_x} n(E'_x)_{E_x} w(E'_x)_{E_x} AG(E_\gamma)_{E'_x}, \tag{3.13}$$

which shows that $AG(E_\gamma)_{E_x}$ can be viewed as a superposition of the weighted sum of all-generation spectra of lower excitation energy, and the first-generation spectrum $FG(E_\gamma)_{E_x}$. $w(E'_x)_{E_x}$ is applied as a weighting factor, encoding the probability of a decay from E_x to E'_x, given as

$$w(E'_x)_{E_x} = \frac{FG(E_x - E'_x)E_x}{\sum_{E'_\gamma}} FG(E'_\gamma)_{E_x}, \tag{3.14}$$

which is basically the normalized first-generation spectrum for the given excitation energy E_x. The normalization factor of Eq. (3.13) $n(E'_x)_{E_x}$ corrects for cross section variation populating the E'_x bins, and is estimated as:

$$n(E'_x)_{E_x} = \frac{M(E'_x)N(E_x)}{M(E_x)N(E'_x)}, \tag{3.15}$$

where $M(E_x)$ and $N(E_x)$ denote the average γ-ray multiplicity and total counts at the given excitation energy E_x. $M(E_x)$ can be estimated from the spectrum as

$$M(E_x) = \frac{E_x}{\langle E_\gamma \rangle}, \tag{3.16}$$

where $\langle E_\gamma \rangle$ is the weighted average at excitation energy E_x. We can now rewrite Eq. (3.13) as

$$FG(E_\gamma)_{E_x} = AG(E_\gamma)_{E_x} - \sum_{E'_x<E_x} n(E'_x)_{E_x} \frac{FG(E_x - E'_x)_{E_x}}{\sum_{E'_\gamma} FG(E'_\gamma)_{E_x}} AG(E_\gamma)_{E'_x} \tag{3.17}$$

These set of equations are solved by an iterative procedure, where the starting trial functions are $FG(E_\gamma)_{E_x}$, and we iterate until convergence. We start out with constant functions as trial functions, where the γ-ray energy E_γ is the same value for all functions. Tests of the convergence properties of the procedure have shown that excellent agreement is achieved between the exact solution (from simulated spectra) and the trial function $FG(E_\gamma)_{E_x}$ already after three iterations [66].

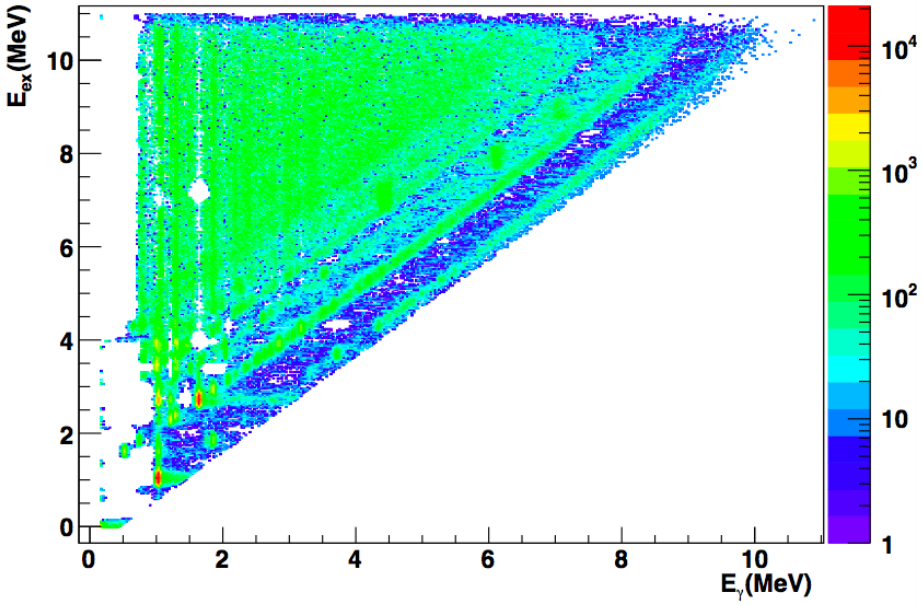

Figure 3.23: The first generation matrix for ^{68}Zn. The number of counts are expressed by a color spectrum from few counts (blue) to most counts (red).

To make the first-generation matrix in MAMA, I used the unfolded spectrum from the iterative unfolding method as input. After iterating through the method, and filling and removing negative counts, I ended up with the first-generation matrix plotted in Figure 3.23.

3.3.4 Extracting the Level Density and γ-Strength Function

When the $FG(E_\gamma)_{E_x}$ trial functions have converged, they are combined and normalized into a decay probability matrix $P(E, E_\gamma)$. When assuming, as the Compound Nucleus model states, that the excitation energy in a compound nucleus will be shared among a large number of nucleons, the nucleon forgets its way of formation (see section 2.1.2). The decay probability $P(E, E_\gamma)$ of a γ-ray with energy E_γ, decaying from energy E is therefore proportional to the transmission coefficient $\mathcal{T}(E_\gamma)$, and the level density $\rho(E_f)$, at the final excitation energy $E_f = E - E_\gamma$:

$$P(E, E_\gamma) \propto \mathcal{T}(E_\gamma)\rho(E_f). \tag{3.18}$$

$\mathcal{T}(E_\gamma)$ is independent of excitation energy, and therefore also independent of the nuclear temperature, according to the Brink hypothesis [49] which states that collective excitation modes built on excited states have the same properties as those built on the ground state. For higher temperatures up towards the GDR, the hypothesis is violated, but since the experiments relevant to the Oslo method have low temperatures and spin values these dependencies are assumed

to be negligible.

To extract the level density and γ-ray transmission coefficient, another iterative procedure is applied to minimize χ^2 as

$$\chi^2 = \frac{1}{N_{free}} \sum_{E=E_{min}}^{E_{max}} \sum_{E_\gamma=E_\gamma^{min}}^{E} (\frac{P_{th}(E,E_\gamma) - P(E,E_\gamma)}{\Delta P(E,E_\gamma)})^2, \tag{3.19}$$

where N_{free} is the degrees of freedom and $\Delta P(E, E_\gamma)$ the uncertainty in the first generation matrix. This is used to normalize the first-generation γ-ray matrix to be within the minimum values $E = E_{min}$, and maximum values $E = E_{max}$, so that for every excitation-energy bin E the bin is unity. Then the output first-generation γ-ray matrix is theoretically determined to be

$$P_{th}(E,E_\gamma) = \frac{\rho(E-E_\gamma)\mathcal{T}(E_\gamma)}{\sum_{E_\gamma=E_{\gamma min}}^{E} \rho(E-E_\gamma)\mathcal{T}(E_\gamma)}. \tag{3.20}$$

E_{min} and E_{max} are chosen to be values that ensure that the data we utilize are from the statistical region of the excitation energy, including no disturbing γ-lines that may still remain after the first-generation method due to incorrect subtraction. Each point of the functions ρ and $\mathcal{T}$ are assumed to be independent variables, and so the reduced χ^2 in Eq. (3.19) is minimized for E and $E-E_\gamma$.

The data points being globally fitted in this way gives us the shape of the level density and the γ-ray transmission coefficient. To perform this process of finding the shape of $\mathcal{T}$ and ρ of ^{68}Zn from the data from the in-elastic scattering experiment, we use the program *Rhosigchi* with input limits of interest for our lower $E_\gamma = 2.36$ MeV and lower and upper excitation energy $E_{ex,l} = 3.0$ MeV and $E_{ex,u} = 11.1$ MeV.

We can still have an infinite number of solutions if the analysis is left at this. The three parameters: A, B and α must be determined, in order to solve the following equations [68]:

$$\tilde{\rho}(E-E_\gamma) = Ae^{\alpha(E-E_\gamma)}\rho(E-E_\gamma), \tag{3.21}$$

and

$$\tilde{\mathcal{T}}(E_\gamma) = Be^{\alpha E_\gamma}\mathcal{T}(E_\gamma) \tag{3.22}$$

and allow only one correct solution, representing the true level density and γ-ray transition strength.

3.3.5 Normalization of the Level Density

To determine α, the slope of $\mathcal{T}$ and ρ, and A which is the absolute value of the level density, ρ had to fit the number of known discrete levels at low excitation energy, while at the same time match neutron (or proton) resonance data at high excitation energy. From Ref. [68], the starting point are the equations:

$$\rho(U,J) = \frac{\sqrt{\pi}}{12}\frac{e^{2\sqrt{aU}}}{a^{1/4}U^{5/4}}\frac{(2J+1)e^{-(J+1/2)^2/2\sigma^2}}{2\sqrt{2\pi}\sigma^3}, \tag{3.23}$$

and

$$\rho(U) = \frac{\sqrt{\pi}}{12}\frac{e^{2\sqrt{aU}}}{a^{1/4}U^{5/4}}\frac{1}{\sqrt{2\pi}\sigma}. \tag{3.24}$$

Here $\rho(U,J)$ is the level density at a given spin J, while $\rho(U)$ is the level density for all spins. a is the level-density parameter, and σ the spin cutoff parameter. In a neutron resonance experiment, if I is set to be the target spin, then the neutron resonance spacing for s-wave neutrons D_0, with a spin/parity of $1/2^+$ can be expressed as

$$\frac{1}{D_0} = \frac{1}{2}[\rho(S_n, J = I + 1/2) + \rho(S_n, J = I - 1/2)]. \tag{3.25}$$

We can do so, since all levels of spin $J = I \pm 1/2$ are accessible in a neutron resonance experiment, and both parities are assumed to contribute equally to the level density at the neutron binding energy S_n. This results in a total level density at the binding energy, with σ calculated at S_n as:

$$\rho(S_n) = \frac{2\sigma^2}{D_0}\frac{1}{(I+1)e^{-(I+1)^2/(2\sigma^2)} + e^{-I^2/2\sigma^2}}. \tag{3.26}$$

I used the program *Robin* to calculate the level density and spin cut-off parameter at $\rho(S_n)$. For spin cut-off formula I used the rigid moment of inertia formula (RMI)(E&B2006) [31]. I then chose the level density parameter a=8.42(26) MeV^{-1} and total backshift parameter $E1$=1.14(30) MeV from the Constant Temperature formula (CT)(E&B2009) [70]. The neutron separation energy $S(n)$= 10.198 MeV was provided to calculate the spin distribution for our spin cut-off parameter, giving $\sigma = 4.26 \pm 0.43$. Since the data itself does not reach excitation energies around S_n, I made an interpolation between the Oslo data and $\rho(S_n)$ using the Constant Temperature model [33]. To do this, I used *D2RHO* to calculate level density ρ from the level spacing D_0 at the neutron and proton separation energy, or excitation energy. I provided the resonance capture levels formed by, in our case, s-wave neutron capture (l=0), since my target is in its ground state and has zero spin in the (n,γ) reaction. The neutron resonance spacing parameter $D_0 = 367 \pm 19$ eV was found through registered info from earlier experiments [72]. σ was calculated by *Robin*, plus a standard deviation of $\approx 0.1\sigma$.

3.3.6 Calculating the γ-Strength Function

The normalization is also important for the γ-strength function, due to the same issue of infinite solutions, as one still has to find the remaining constant B in Eq. 3.22. This is done by using the experimentally measured average total radiative width Γ at the neutron separation energy through the formula from Ref. [69]:

$$\langle \Gamma_\gamma(E, I, \pi) \rangle = \frac{1}{2\pi\rho(E, I, \pi)} \sum_{XL} \sum_{I_f, \pi_f} \int_{E_\gamma=0}^{E} dE_\gamma \mathcal{T}_{XL}(E_\gamma) \rho(E - E_\gamma, I_f, \pi_f), \tag{3.27}$$

where $\langle \Gamma_\gamma(E, I, \pi) \rangle$ is the average total radiative width of levels of energy E, spin I and parity π. Then integrate over all states that are accessible through γ-ray transitions with energy E_γ, and add up over all final levels with final spin I_f, final parity π_f, electromagnetic character X and multipolarity L.

The relationship between the γ-ray strength-function $f(E_\gamma)$ and the γ-ray transmission coefficient $\mathcal{T}(E_\gamma)$ is given in Eq. (2.14). Assuming that the main contribution of γ-ray transmissions are of dipole character (l=1), it can be expressed as

$$B\mathcal{T}(E_\gamma) = B \sum_{XL} \mathcal{T}_{XL}(E_\gamma) \approx B[\mathcal{T}_{E1}(E_\gamma) + \mathcal{T}_{M1}(E_\gamma)], \tag{3.28}$$

and the experimental γ-ray strength function can be found as

$$f(E_\gamma) = \frac{1}{2\pi E_\gamma^3} B\mathcal{T}(E_\gamma). \tag{3.29}$$

Assuming that any excitation energy and spin has equally many accessible levels with positive and negative parity, the level density ρ is given as

$$\rho(E - E_\gamma, I_f, \pm\pi_f) = \frac{1}{2}\rho(E - E_\gamma, I_f). \tag{3.30}$$

Combining Eq. 3.27, 3.28 and 3.30, the total average radiative width of an s-wave neutron capture resonance with spins $I_t \pm 1/2$ can be expressed in terms of the transmission coefficient $\mathcal{T}$ and the experimental level density $\rho(S_n - E_\gamma)$ as

$$\begin{aligned} \langle \Gamma_\gamma(S_n, I_t \pm 1/2, \pi_t) \rangle = \frac{B}{4\pi\rho(S_n, I_t \pm 1/2, \pi_t)} \int_{E_\gamma=0}^{S_n} dE_\gamma \mathcal{T}_{XL}(E_\gamma) \\ \times \rho(S_n - E_\gamma) \sum_{J=-1}^{1} g(S_n - E_\gamma, \mathrm{I}_t \pm 1/2 + \mathrm{J}), \end{aligned} \tag{3.31}$$

where I_t is the spin of the target nucleus in the reaction, π is the parity of the target. We also have that $\frac{B}{4\pi\rho(S_n, I_t \pm 1/2, \pi_t)} = D_0$, the neutron resonance spacing. The spin distribution $g(E, I)$ of the level density is given by [34]:

$$g(E, I) = \frac{2I + 1}{2\sigma^2} e^{-(I+1/2)^2/2\sigma^2}, \tag{3.32}$$

and then g is normalized over all I to be unity. By applying an experimental value for $\langle \Gamma_\gamma \rangle$ at S_n, the weighted sum of the widths of all the levels of spin

$I_t \pm 1/2$ is found by using Eq. 3.31. From this B can be determined. For the analysis, I used the program *Normalization* to normalize the γSF. I used the previously mentioned neutron resonance spacing D_0 from [72] and the average total radiative resonance width $\Gamma = 440 \pm$ MeV, also found in [72]. However, the method suffers in the extraction of the first-generation γ-ray matrix for energies $E_\gamma < E_\gamma^{min}$. In addition, the data for the higher γ-energies up towards S_n is suffering from low statistics. I extrapolated $\mathcal{T}$ with an exponential function to overcome this difficulty.

3.4 Comparison of the Constant Temperature- and Fermi Gas Model

There are several different models discussed in the Oslo Method, and the two most used are the Fermi Gas model and the Constant Temperature model. In this energy range under 10 MeV, the Constant Temperature model is often recommended, as discussed in the theory section. However, it is good practise to check what really works for the data. I therefore looked at the resulting calculations using both of these models before proceeding. The resulting level densities (see Figure 3.24) show a typical Constant Temperature profile, but very minimal differences, making the choice of model quite arbitrary based on this result. Other results had to be studied as well to see if they are better at indicating the winning model.

For the calculated transmission coefficient, see Figure 3.25, there is a slight difference in modelled shape at lower energies. This is a hint that something in the models is going to affect the resulting γ-ray strength function. From this, it was not really easy to determine which is better, so I continued looking. By comparing the two models resulting γ-ray strength function, the main difference in the result was the effect on the upbend and how precisely the model followed the data. I trust our data in the low energy area, and see a very constant-temperature tendency to the level density as well. The Fermi Gas is very similar, but seems to underestimate the upbend slope compared to the data. The Constant Temperature follows the data better, as shown in Figure 3.26, which also resounds what the assumption was beforehand: that CT is better for this energy region. I therefore chose to use the Constant Temperature model for the data analysis.

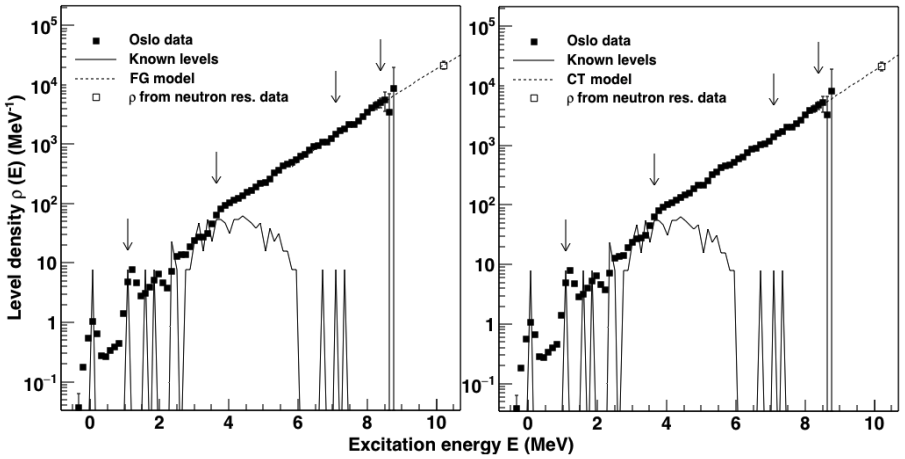

Figure 3.24: The calculated nuclear level density from the Oslo method, using the Fermi Gas model to the left, and the Constant Temperature model to the right.

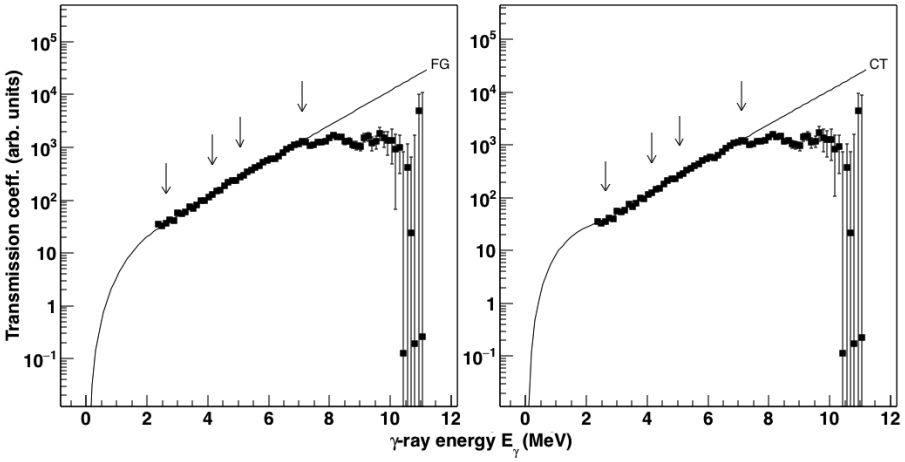

Figure 3.25: The calculated transmission coefficient from the Oslo method, using the Fermi Gas model to the left, and the Constant Temperature model to the right.

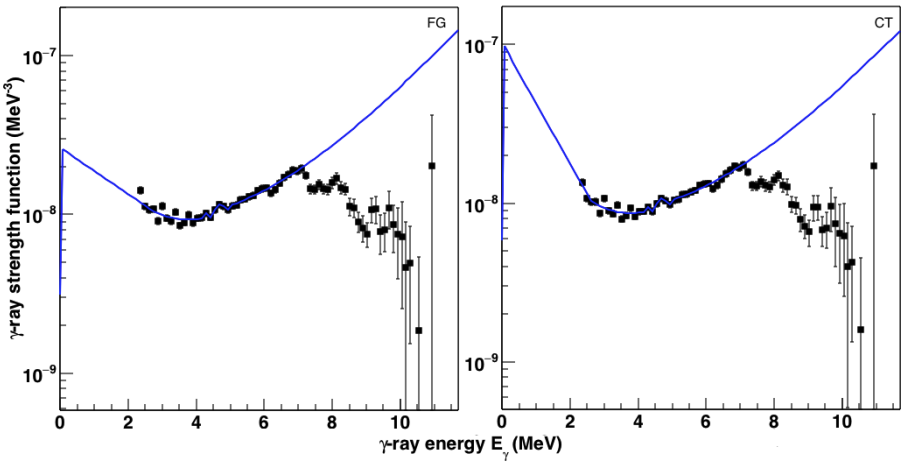

Figure 3.26: The calculated γ-ray strength function from the Oslo method, using the Fermi Gas model to the left, and the Constant Temperature model to the right.

Chapter 4

Experimental details and data analysis of the ^{68}Zn(γ,n) measurement

To cover another energy domain in the γ-strength function, which will help normalize the Oslo data and get a broader understanding of the shape and nature of the γ-strength behavior of this nucleus, we went to Japan!

4.1 Experimental Setup at NewSUBARU

4.1.1 The NewSUBARU Facility

The NewSUBARU Synchrotron Radiation Facility is constructed at SPring-8 in Hyogo, Japan. SPring-8 (Super Photon ring with electron energies of 8 GeV) is a large synchrotron radiation facility managed by RIKEN, with JASRI in charge of usage. The facility accelerates electron beams to close to the speed of light, and applies a magnetic field to force the beam into a curved path. As an effect, electromagnetic radiation beams are created. This radiation is the highest brilliance synchrotron radiation in the world [73], with photon energies in the range 300eV to 300keV. The facility also produces γ-rays of up to 3 GeV, and infrared radiation. NewSUBARU recieves electron beam from the linear accelerator at this site, as shown in Figure 4.1. This smaller facility generates complementary spectral regions, and consists mainly of a 1 GeV electron storage ring operated by the Laboratory of Advanced Science and Technology for Industry at University of Hyogo (LASTI), made for using synchrotron radiation in the soft X-ray to UV regime of energies. The ring is a racetrack type, and is 119 m long in total. The electrons in this ring are delivered directly from the linear accelerator, with energies of around 1 GeV. The storage ring can accelerate or decelerate electrons on its own, and has the capability of adjusting the electron energy. This is useful as we in this experiment will collide a laser beam with the accelerated electrons in a reverse Compton scattering collision, which will be discussed in detail later. If the laser alone was to decide the energy, then we would need to change its wavelength, which is hard to control and

Figure 4.1: View of the SPring-8 accelerator complex. The complex is composed of a 1 GeV linac, 8 GeV booster synchrotron, 1 GeV NewSUBARU storage ring and 8 GeV SPring-8 storage ring. Figure taken from [74].

implement experimentally. As shown in Figure 4.2: On one side of the storage ring is a 12 m long straight path, at which the BL01 beamline is located. The BL01 beamline is used for research and develops new light sources for different applications. This is one of two long straight sections, with an optical klystron installed on it. The optical klystron consists of two undulators sepated by a dispersive section, where the electron energy decides the transit time [75]. The two main applications of the optical klystron are: used as a light amplifier in a Free Electron Laser (FEL), or as a source of coherent synchrotron radiation, in which bunching of the electron beam enhances the emission.

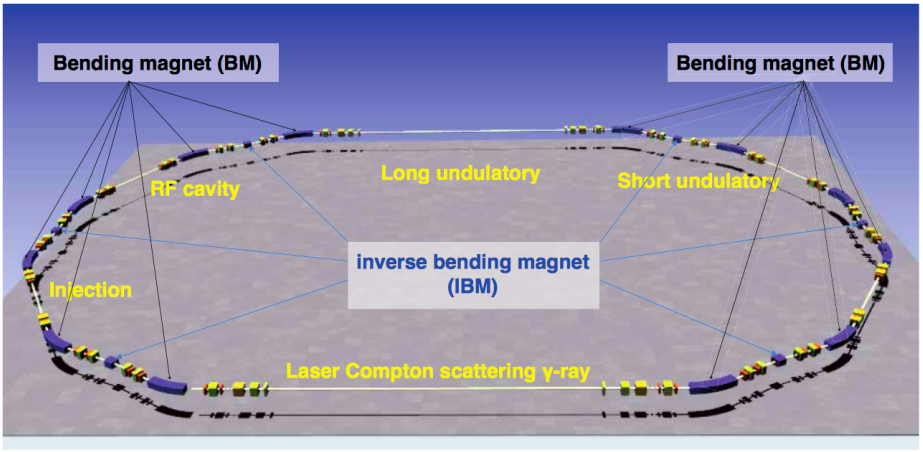

Figure 4.2: Layout of NewSUBARU electron storage ring. The ring consists of 12 bending magnets, 6 inverse bending magnets, multipole magnets and steering magnets. BL01 (Laser Compton scattering γ-ray) is located at the lower long straight path of this illustration. Figure taken from [76].

4.1.2 Laser Compton Scattering

We will be using only the downstream side of this beamline: BL01A. Currently it is used to generate 1-40 MeV laser-Compton γ-rays by inverse Compton scattering [77], see Figure 4.3. This is done by making external laser photons scatter on to the NewSUBARU relativistic electrons. The Laser Compton scattered γ-ray's have an energy E_γ described in [76] as

$$E_\gamma = \frac{4\gamma^2 E_L}{1 + \gamma^2\theta^2 + \frac{4\gamma E_L}{m_e c^2}} \tag{4.1}$$

where $\gamma = \frac{E_e}{m_e c^2}$, E_L is the laser photon energy, γ is the lorentz factor from dealing with relativistic electrons and E_e is the electron kinetic energy. θ is the angle between the direction of the outgoing γ-ray and the incident electron, m_e is the electron rest mass and c the speed of light. The formula in Eq. (4.1) can to some be recognizable as not too different from the original Compton scattering energy relation. If the collision electrons did not have relativistic speed, this equation would be of the original compton form [78]:

$$E_\gamma = \frac{E_L}{1 + (E_\gamma / m_e c^2) + (1 - cos\theta)}. \tag{4.2}$$

The introduction of the Lorentz factor γ is necessary to take the relativistic energy of the electrons into account. To find the final energy of the photon, one must perform two Lorentz transformations, as the standard Compton equations are valid only from the electron's rest frame. The frequencies and angles of the photon as seen by the moving electron are not the same as the ones measured in the lab frame, so one must transform into the electron frame of reference, and back out again. This process therefore converts a low-energy photon to a high-energy one by a factor of order γ^2 [78]. By also assuming ultrarelativistic

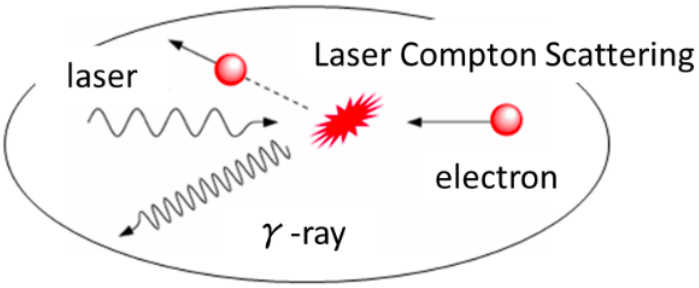

Figure 4.3: Laser Compton Scattering: Collision between laser photons and accelerated electron. The process is also called Inverse Compton Scattering, and it gives the resulting collisional energy to the photon, as illustrated by [79]. Only the backscattered (about 180° scattered) photons (γ-rays) are used.

electrons, and that the photon is most likely scattered into a cone with opening angle along the direction of the incident electron of $2/\gamma \approx 1$ mrad for 1 GeV electrons, one can assume $\theta << 1, \gamma >> 1$ and $\beta \approx 1$. Then Eq. (4.2) reduces to Eq. (4.1).

The energy of the outgoing γ-ray can be changed by either changing the electron energy in the storage ring, or adjusting the laser wavelength. The resulting γ-ray has the unique characteristics of tuneable energy and polarization, as well as being well directed and quasi-monoenergetic. These qualities are useful in various fields of study, including CT-imaging, nuclear transmutation, electron pair creation and photo-nuclear reactions.

4.1.3 The Experimental Hutch

In the experimental hall the lasers are introduced by mirrors into NewSUBARU. The electrons in the ring will collide head on with the incoming laser beam at positions shown in Figure 4.4. The lasers used are Nd:YVO_4 with a wavelength of 1 μm and 0.5 m, and CO_2 with a wavelength of 10.6 μm. The resulting γ-rays from this collision are used for various detection purposes. For performing measurements we used a NaI scintillation counter, a LaBr3:Ce detector and neutron counters. An MCA was used for analog to digital conversion of the detector signals.

In the vacuum tube a mirror is used to introduce laser beams into the beam tube. Generated γ-rays pass through the mirror and window, into the shielding hutch. The energy of Compton γ-rays depend on the angle of which it exits the scattering. We end up with quasi-monoenergetic γ-rays by using a collimator to select outgoing γ-rays with a minimal angle distribution. The collimator is made of lead, and has 6 or 3 mm diameter hole for rays to pass through. The spectra of the γ ray represent the convolution of the detector response function with the γ ray energy distribution. This can be measured by the LaBr3:Ce

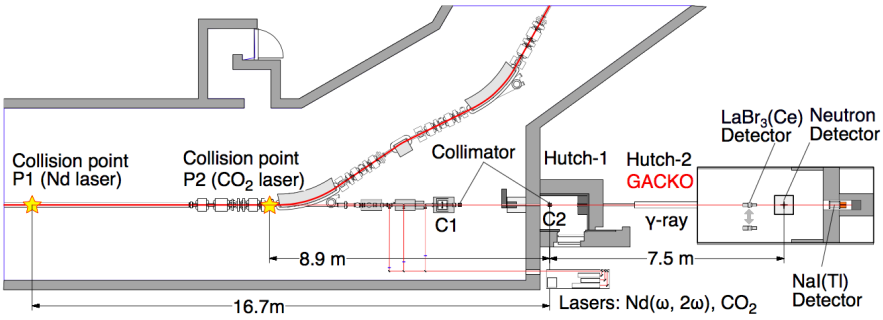

Figure 4.4: Setup of Laser Compton scattering γ-ray beamline. Figure taken from [80].

detector using the MCA, with corrections by simulations to obtain the original energy distribution.

Finally at the end station, the shielding hutch can release the produced and transported γ ray for use, see Figure 4.4. The γ-ray irradiation hutch GACKO is installed at BL01A, and is a collaboration with Konan University. When the electrons have 1 GeV energies, the current is 250 mA, and the laser power of the Nd 1 μm laser is 4W, a γ flux of 6×106 photons/s with energies of 6-17 MeV is generated. Without any collimation, the γ ray beam size in the hutch is 10 mm, 19 m from the collision point. Targets for sampling are placed inside the hutch and irradiated by the γ-rays while the hutch door is thoroughly closed.

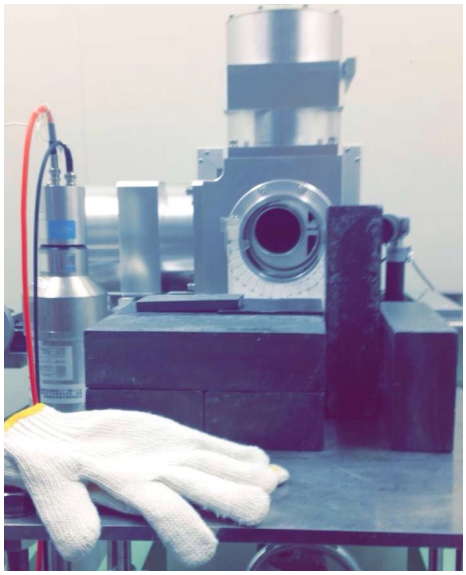

Figure 4.5: The entrance for the γ-rays through the shutter into the enclosed experiment hutch. To the left is the LaBr3:Ce detector placed aside when it was not used for gathering the single photon spectra. Gloves are used to avoid led contamination from the isolating led pieces around the slightly radioactive LaBr3:Ce detector.

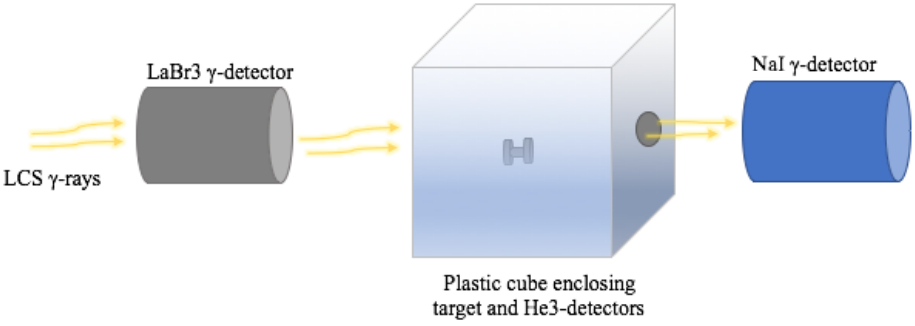

Figure 4.6: Inside the hutch: Setup for detecting single photon spectra with the LaBr3:Ce detector, which is later removed from the line of the beam letting it interact with the target through a hole in the plastic cube. The He3 detectors are located in three rings of different radii around the target to detect outgoing neutrons. The NaI detector detects all the incoming γ-rays.

4.1.4 Experimental Procedure during Measurements

For every data point we collected, we had to explore a different energy for a different isotope. The energy of the γ-rays for our experiment is determined by the energy of the electrons in the storage ring, so that for every new γ-energy the electron energy was adjusted by the operators. This chain of reactions is sensitive to error as it goes through several processes: the storage ring energy adjustment itself and also the laser collision. Each time we changed the beam energy, we repeated a cycle of tests which ends up being quite time consuming. First we did a simple check of the new beam by removing the mirror that redirects the synchrotron light radiation away from our experiment. Letting the light pass through, we checked using transparent barriers if the incoming beam hit both the entrance of the tunnel in which the target (pictured in Figure 4.7) was later positioned, and also that the light comes through to the end of this tunnel without being disturbed. It is important to irradiate only the target material in order for the calculation of number of atoms which can interact with the γ-ray to reflect the actual occurring process/reactions. Once we knew this was fulfilled, the LaBr3:Ce-detector was placed in front of the target tunnel and we did another test to see if the beam hit this detector as well.

Figure 4.7: The Zn-targets we did measurements for in this experiment. My favorite is to the very left.

4.1.5 LaBr3:Ce-detector γ-ray Spectra

When the alignment was done, we were now ready to do runs for all our targets that require this beam energy. We collected data for a short time of 180 seconds, with a low intensity on the laser beam (0.5%), low enough to know we only register one photon at a time, using continuous wave. This spectrum is essential when analyzing multiple photon spectra, to know how many photons were really detected.

4.1.6 NaI-detector γ-ray Spectra

After performing the singles spectrum measurement, we moved this detector out of the beam line. The internal gain was adjusted to be about 12-14%, and a single photon spectra measured was measured using the NaI detector as well, for a short time of 180 seconds. This together with the LaBr3:Ce spectra tells us about the identity of the single photon spectrum. Now we could finally insert the targets and start measuring. We proceeded to collect multiple photon spectra (ON) and background spectra (OFF) until a significant neutron count (preferably 10000) was reached for each target. This could take from a few minutes to several hours, depending on which energy the beam was, if it was approaching the lower boundary of the neutron separation energy, and also on the intensity of the beam. The intensity was constantly sinking until we needed a re-injection to be able to count any neutrons. After all relevant targets had been measured, we did a couple of last safety checks to see if everything was still normal and our measurements still valid throughout the whole target selection. We performed short single photon and LaBr3:Ce runs, just like the ones performed before the long runs. If something had gone wrong during the measurements, these extra-safety spectra can help us discover this.

4.1.7 Counting Neutrons

Inside the hutch, the γ ray will be used to knock neutrons out of our target. The targets used in this experiment are ^{64}Zn, ^{66}Zn, ^{68}Zn, ^{182}W, ^{183}W, ^{184}W and ^{60}Ni, but I will only be discussing and analyzing ^{68}Zn. Using a constant laser beam with a given wavelength, we need to change the electron energy in the storage ring to change the energy of the γ ray. Therefore it was useful to do all relevant targets spectra for each energy before changing it. The target, pictured in Figure 4.7, is placed in the very center of a cube of plastic, which acts as a neutron moderator. Around the target, long cylindrical tubes of ^{3}He were placed in three rings at different radial distances away from the target in the center, see Figure 4.8 and 4.9. These are also called proportional counters because the signal is proportional with the energy deposited by the particle (different types of particles give rise to different signal curves), and they are detecting the neutrons that are knocked out of the target.

The reaction involved in this detection is $^3\text{He} \rightarrow ^3\text{H} + \text{p} + \text{Q}$, where Q = 730 keV is the energy threshold needed to be registered by the detector for us to know a neutron detection occurred. It is the kinetic energy of the ions that ionizes the gas and provides an signal. The wire providing high voltage to the ^{3}He counters makes sure that the signal is transferred as well. The same box

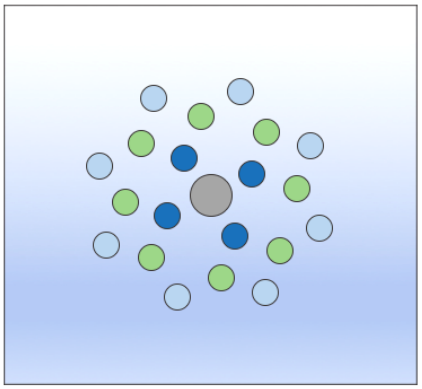

Figure 4.8: A plastic cube with an empty tunnel through the middle where the target sylinders are placed. Surrounding the target is three rings of neutron-detecting ^{3}He detectors, where the inner blue ring is R1, the middle green ring is R2 and the outer light blue ring is R3.

giving the high voltage is also a discriminator. A threshold is chosen in order to filter our energy signals of a lower energy, so that they do not result in a logic pulse out. Every ^{3}He counter is wired to a channel in this discriminator (and power supply) and on to a scaler which counts the number of logic pulses. The pipes are connected in such a way that the separate ring neutron count signals are added together, and displayed as neutron counts in ring R1, R2 and R3. Each ring also registers neutron counts dR1, dR2, dR3, which were not in coincidence with a γ-detection, and therefore these neutrons are background noise in the corresponding ring.

When collecting data, one has to make sure that the relationship between the neutron counts and the error-counts is quite large, and also that the neutron count was high enough to give significant and good statistics (ideally 10000 neutron counts in a ring). Getting enough neutron counts was sometimes difficult and time consuming, due to several factors. Firstly, for low energies relative to the neutron separation energy of the target isotopes, the neutron count per time was also low. Secondly, the beam intensity was dropping off significantly as time since the last new beam injection passed. When starting out with a fresh beam injection, a lot of neutron counts ticked in. The intensity however decreased as time went on, and every 5-6 hours a beam injection was required to get more intensity. But while at the end of the beams life, more counts could be acquired by turning up the laser intensity to reinforce more energy into the Compton collision. However, the laser interaction with the electron beam will increase the entropy of the electron beam and that will result in a broader energy spectrum.

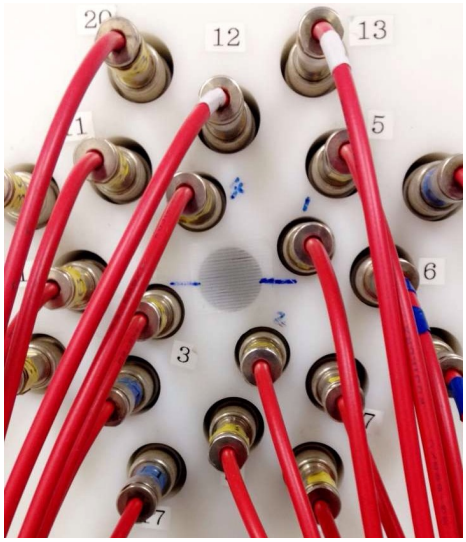

Figure 4.9: A plastic cube with an empty tunnel through the middle where the target sylinders are placed. Surrounding the target is three rings of neutron-detecting ^{3}He detectors, sending electrical signals to neutron counters for the three rings.

4.2 Data Analysis

After performing a (γ,n) experiment, by counting neutrons and counting γ-rays, the (γ,n) cross section for the experiment reaction can be calculated.

4.2.1 γ,n - Cross Section

In order to find the neutron cross section for a (γ, n) reaction the formula

$$\sigma = \frac{N_n}{N_t \cdot N_\gamma}, \tag{4.3}$$

is used, where N_n is the number of neutrons counted by the ^{3}He-detectors, N_t is the number of atoms in the target, and N_γ is the number of γ-rays registered by the NaI-detector. We do get a spread in energy due to the scattering angle of the photons θ, so we have to take this energy spread into account. This is done by writing

$$\int_{S_n}^{E_{min}} n(E_\gamma)\sigma(E_\gamma)dE_\gamma = \frac{N_n}{N_t \cdot N_\gamma}, \tag{4.4}$$

where E_γ is the energy of the gamma coming out of the collision, E_{max} would be the energy of a photon coming straight back the in same direction after the collision, as it had approaching the collision. E_{min} is the energy of the largest scattering angle that is able to enter through the collimators and hit the target, and S_n is the neutron separation energy. This equation contains several values which I need to extract from experimental data, to be able to calculate the final cross section.

For the data analysis of the (γ,n)-data, I had to both analyze the neutron detector results, the counts in the three rings, find the shape of the reaction cross section, and also attempt to filter out how many photons were actually impinging onto the target. For the γ-rays we have recorded a singles spectrum with a LaBr3:Ce-detector to identify what the profile of an incoming photon does look like. But for the NaI-detectors we detected many photons at once, and the challenge is trying to separate this pileup spectrum into the real amount of photons. Such a pileup and singles spectrum for one run is shown in Figure 4.10. I also subtracted the background spectrum of γ-rays radiating from everywhere else, which is also disturbing the true count/distribution.

In order to determine the average energy of the counted neutrons, the ring ratio technique [81] was used. This average energy will affect the efficiency of the neutron detector. Using a ^{252}Cf source, the efficiency was measured, and the energy dependence was found using Monte Carlo simulations, by simulating mono energetic, isotropically distributed neutrons. The efficiency profile from the ring ratio method is shown in Figure 4.11.

This analysis was mainly performed using Matlab. To begin with, I subtracted the background from both the singles and pileup spectrum. After that, I set a threshold around a separated γ-ray in the pileup spectrum in Figure 4.10. I did this by visually plotting and comparing the two for all the corresponding runs. Then the number of photons were calculated using the pileup method. In order to calculate the maximum γ-energy, I used previously calibrated coefficients, the electron energies used in the runs and the laser wavelength used in ($E_{Laser} = \frac{\hbar c 2\pi}{\lambda}$). For energies above 974 MeV I used a polynomial from T.Shima. Otherwise, Aksel-coefficients [82], [83] are used.

For the neutron analysis, the number of registered neutrons N_n were collected in one file manually, and used directly as N_n in Eq. (4.4). This is the equation used in order to calculate the naive monochromatic cross section, which I later had to unfold for the spread in energy occurring. But first, let me show you what the cross section looks like if I assume all γ-rays had the maximum energy calculated (as would be the result of a direct Compton back-scatter). This result is plotted in Figure 4.12. The incoming beam unfortunately is not monochromatic, which I corrected for using an unfolding procedure to reproduce the original photon spectrum. There are several tried and tested ways of going about this, and I will here briefly compare two well established procedures: Firstly the Matrix method, and next the Bayesian Monte Carlo Markov Chain method.

After this naive calculation, the first step to improve it was by correcting for the g-factor (the fraction of γ-rays which are above the neutron separation energy and therefore actually candidates for the reaction) and the attenuation of the beam as it goes through the materials. I did this by altering the ideal Eq. (4.4):

$$\sigma_{exp}^{E_{max}} = \int_{S_n}^{E_{min}} n(E_\gamma)\sigma(E_\gamma)dE_\gamma = \frac{N_n}{N_t \cdot N_\gamma \xi \epsilon_n g}, \tag{4.5}$$

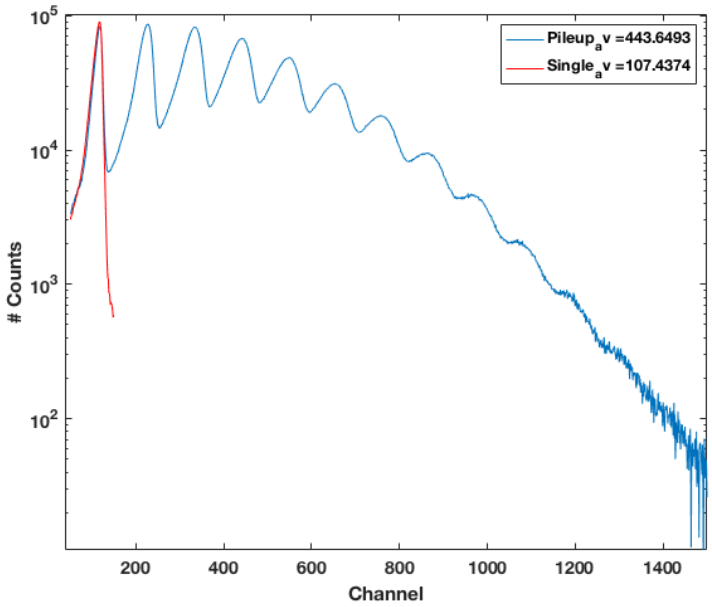

Figure 4.10: The photon pile-up spectrum plotted together with the single photon spectrum, with appropriate thresholds set for the single photon to indicate the actual photon profile.

where $\epsilon = (1 - e^{\mu t})/(\mu t)$ gives a correction for the self-attenuation in the target and g is the g-factor. ϵ_n represents the neutron detection efficiency. As mentioned above the efficiency is energy dependent and calculated using the ring ratio method [81]. After these corrections I went on to attempt an unfolding for a spread in outgoing scattering angles and energy.

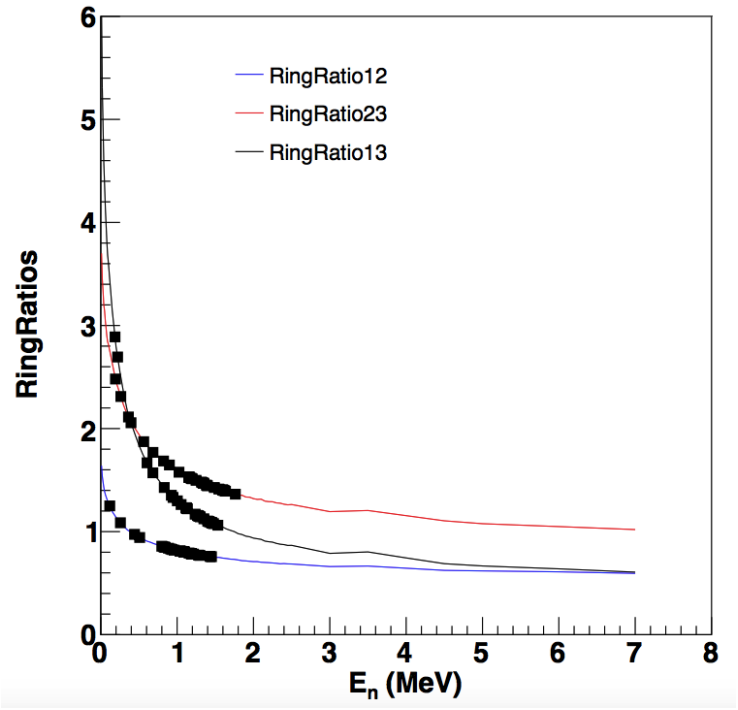

Figure 4.11: The efficiency as a function of neutron energy as calculated using the Ring Ratio method. [81]

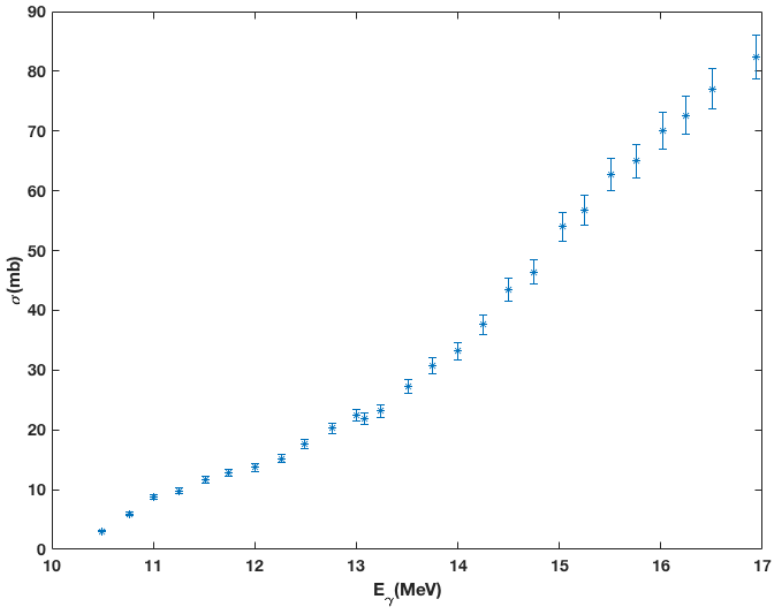

Figure 4.12: The calculated monochromatic cross section for the ^{68}Zn(γ,n)^{67}Zn reaction.

4.3 Unfolding the γ-spectrum

Using GEANT4 simulations of the beams at each energy, one can learn about the true energy profiles, see Figure 4.13. These will be cut off at the neutron separation energy, as those contributions will not be relevant, as shown in Figure 4.13. The calculated mono chromatic cross section (see Figure 4.12) ap-

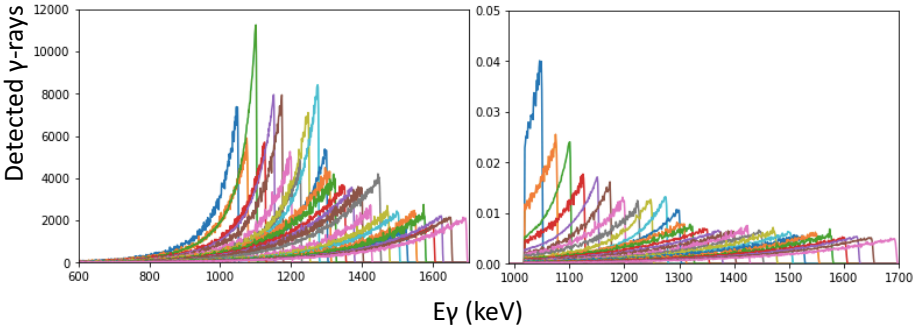

Figure 4.13: The simulated γ-profiles for all the electron energies. To the right, a normalization have been applied to correct for varying run-times of simulations and similar. We also look only at the energies above S_n as these are the only contributing γ-rays for our reaction.

pears very smooth, and shows a clear Giant Dipole Resonance shape. However, the (γ,n)-data proved to be very sensitive throughout the analysis, showing a resonant behavior. Previous data [84], [85], seem conflicted on whether or not to expect such resonances after the unfolding procedure. I therefore wanted to try different unfolding techniques, in case our first attempt to do the regular unfolding is flawed and too sensitive. First a quick introduction to the two methods:

4.3.1 The Iterative Method

In a similar fashion to the Oslo method [64], the iterative method is based on finding a solution to the equation

$$\sigma_f^{i+1} = D\sigma^{i+1} \approx \sigma_{exp} \tag{4.6}$$

where σ_{exp} is the monochromatic cross section calculated from the experimental data, $\mathbf{D}$ is the response matrix, consisting of our simulated response functions in a N $\times$ M matrix, M being the number of channels in the simulations, and the length of the response function files, and N is the number of measured points (runs).

As a starting point, a constant trial function σ^0 is chosen for the 0th iteration. By multiplying this vector by $\mathbf{D}$, we get the 0th folded vector σ_f^0=$\mathbf{D}\sigma^0$. The next trial function is established by adding the difference of the experimentally measured spectrum σ_{exp}, and σ_f^0, to σ_0. An interpolation is applied so that the vectors are of equal dimensions. The next input vector will be $\sigma = \sigma^0 + (\sigma_{exp} - \sigma_f^0)$. These steps are iterated i times, as expressed in Eq. (4.6),

until convergence is achieved. This usually takes about four iterations.

After unfolding, an energy-dependent smoothing was applied to obtain the real cross section. The filter width is set to the FWHM of the photon spectrum to avoid finer disturbing structures. In order to estimate the uncertainty of the unfolded cross section, an upper and lower limit of monochromatic cross section calculations are constructed by adding and subtracting the errors of the measured cross section values. These upper and lower limit monochromatic cross sections were separately unfolded.

4.3.2 Fully Bayesian MCMC

This method is well described in Ref. [71], but I will give a brief explanation of how it is done. The Fully Bayesian unfolding can be expressed analytically through Bayes' theorem:

$$p_{posterior}(\sigma_{unfold|\sigma_{exp}}) = \frac{L(\sigma_{exp}|\sigma_{unfold})p_{prior}(\sigma_{unfold})}{p_{marginal}(\sigma_{exp})} \sim L(\sigma_{exp}|\sigma_{unfold})p_{prior}(\sigma_{unfold}), \tag{4.7}$$

which allows calculation of the probability density of the unfolded cross section $p_{posterior}(\sigma_{unfold}|\sigma_{exp})$ from the likelihood function L, the marginal distribution $p_{marginal}(\sigma_{exp})$ and the prior distribution $p_{prior}(\sigma_{unfold})$ which is known ahead of the experiment.

The first step is choosing p_{prior}, which can be chosen such that smooth and consistent behaviour is favored. Next for finding $p_{posterior}$, Monte Carlo Markov Chain algorithms are used in order to generate a large number of starting samples. Then their average value and error bands are calculated. The prior distributions of the form

$$p_{prior}(\sigma_{unfold}) = e^{-\tau S(\sigma_{unfold})}, \tag{4.8}$$

is convenient to use. Here $\tau > 0$ is the regularization parameter, and (σ_{unfold}) is a function that is large when large fluctuations occur. S can be chosen to be several different functions, for instance the sum of squares $S(\sigma) = \sum \sigma_i^2$ of the sum of squared differences: $S(\sigma) = \sum_i (\sigma_{i+1} - \sigma_i)^2$. Larger values of τ impose stronger fluctuation limitations of the unfolded cross sections.

4.3.3 Unfolding Comparison

I first used an iterative matrix-unfolding method in matlab, and I also attempted a similar implementation in python (which yielded similar results, see Figure 4.15). Since both of these had a tendency to be intimidatingly resonant, I tried another method using Monte Carlo Markov Chains and a randomized, less biased approach [71]. This method allows for more intense smoothing, and as shown in Figure 4.16 this could have a prominent effect. As even this approach ended up displaying a similar shape to what I saw in our iterative matrix method, I now have increased confidence that the matrix method works well, and shows true resonances in ^{68}Zn. Similar results was also found for the other Zn-isotopes we collected data for in Japan. However, these are not published yet to be referenced. Another reality check is comparing our results with previous experimental results. Such a comparison is presented in Chapter 5.

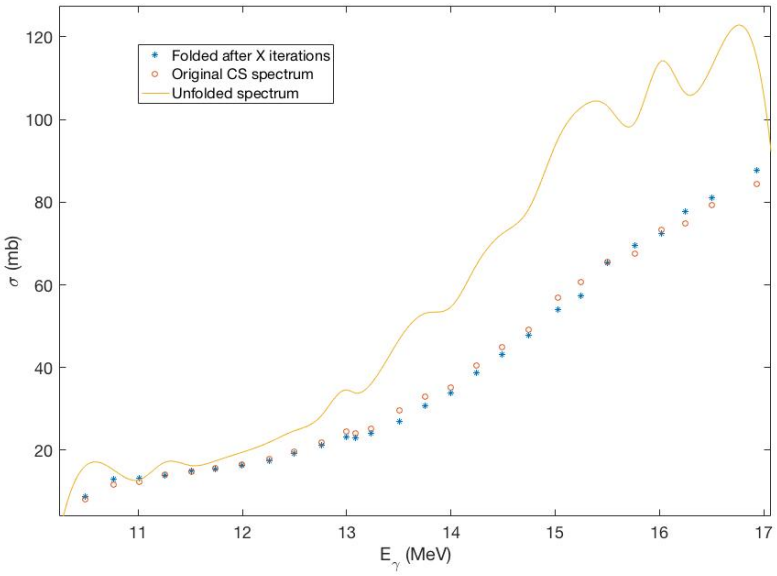

Figure 4.14: The calculated unfolded cross section. The original CS spectrum in red is corrected for both g-factor and attenuation. One can recognize the monochromatic spectrum results as the folded spectrum.

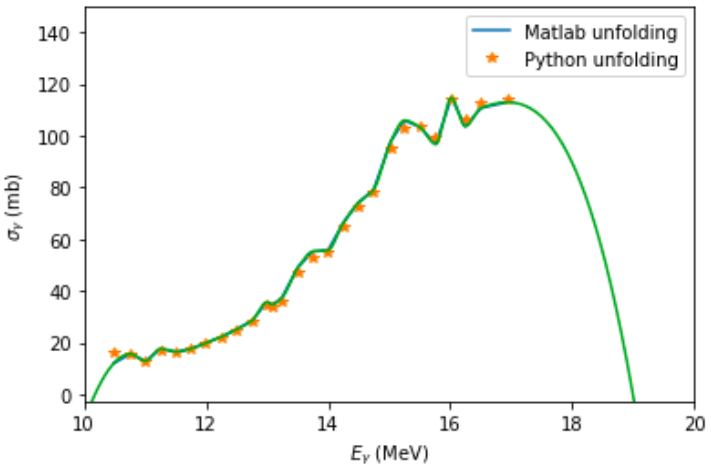

Figure 4.15: The calculated unfolded cross section from both the unfolding in matlab and python for comparison. They produce comparable results.

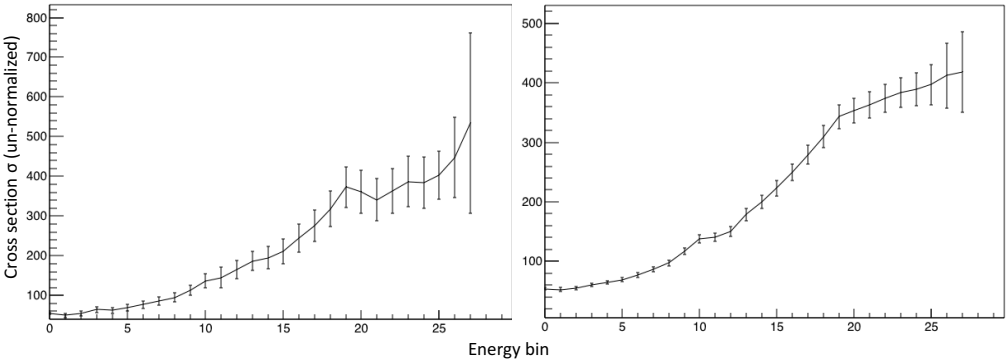

Figure 4.16: The calculated unfolded cross section using the mcmc-method, using a low τ (low resonance supression) to the left and a high τ to the right. To the left, clear resonances are visible, and to the right the spectrum is much smoother. This plot is an illustration of the recognizable shape of the resonances in the other methods (it is not normalized to the same values, and plotted by energy bins, not the genuine energy).

Chapter 5

Results and Application in TALYS

5.1 Results from the Oslo Method

The experimental nuclear level density $\rho(E_x)$, the transmission coefficient $\mathcal{T}(E_\gamma)$ and the normalized γ-ray strength function $f_{XL}(E_\gamma)$ resulting from the Oslo Method are plotted in Figure 5.1, together with the estimation of the spin cutoff parameter $\sigma(E_x)$ which I used in the calculations. The level density model chosen to extrapolate from our last data point, up towards the (γ,n)-data was the Constant Temperature model, and the normalization coefficients D_0 and $\langle\Gamma_{\gamma 0}\rangle$ were found in Ref. [72]. For the NLD the known levels from the discrete level scheme seems to be complete up to about $E_x \approx 3.5$ MeV, as they follow the same trend as the experimentally calculated level density up to this point. The NLD shows no significant large-scale structures, an even exponential growth which is typical according to the Constant Temperature model is observable.

The γSF from the Oslo Method shows a slight tilt up towards the GDR, which is as expected, as the goal is to construct a total solution to the γSF by fitting this data to the (γ, n) data, by using models (See Chapter 2.3.1) of the E1 and M1 components of strength function. An interesting artifact which is visible in this lower region of the γSF, is the characteristic low energy enhancement or so called *upbend* in the $E_\gamma < 4$ MeV region. The same feature has also been reported in a number of other light- and medium mass nuclei [86]. As discussed in Chapter 2, the origin of this enhancement is debated. It is seemingly of a dipole nature, but the electric or magnetic character remains an open question. However, as I move along with fitting the γSF, an assumption will be made to include it in the $M1$ part of the function, as it seems to be the most popular theory at this point. It does not really matter for the fit what the enhancement is included in, as long as it is being accounted for. A direct measurement of the polarization is the crucial missing piece of information, which would tell us about the true nature of the low-energy enhancement [86].

In Figure 5.1, and this is a general comment for all the calculated results from the Oslo Method, the uncertainty for high energies rapidly explodes, and this is a natural consequence of how few counts are present in the high energy region of the extracted coincidence matrix, see Figure 3.19. With low statistics, the data is not trustworthy and therefore I have chosen to put pointers on the lower regions of the transmission coefficient spectrum, as shown in Figure 5.1. These arrows are set to define the limits for which data points are fixed to match the level density of discrete states. By doing this the data yielded reasonable results, and the strength function moves nicely towards higher energies to meet the GDR-data from the (n,γ) experiment.

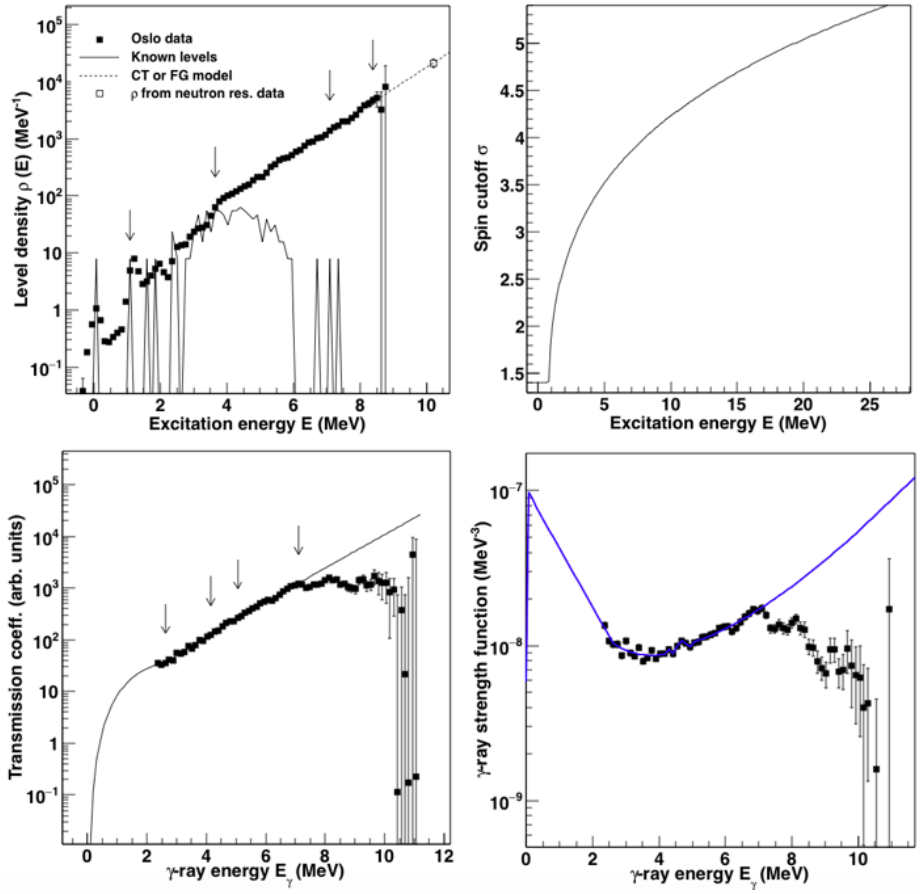

Figure 5.1: Upper left: The calculated NLD, Upper right: The spin-cutoff parameter, Lower left: The transmission coefficient and Lower right: The calculated and estimated GSF.

5.2 (γ,n) Results

The resulting photonuclear reaction cross section for ^{68}Zn(γ,n) is presented in Figure 5.2. This cross section was found from experimental neutron and γ-ray measurements, using Eq. (4.4) and unfolded by applying the unfolded iterative method typically used by the Oslo group. In this part of the cross section, one can definitely see some interesting resonances, which have previously been discussed and could come from the unfolding, but after comparing with other unfolding methods these seem to be manifestations of actual structural resonances. These resonances may be due to interaction of dipole states with more complicated collective states, and I will get back to this shortly.

When comparing this result with previous experimental measurements, as shown in Figure 5.2, B. S. Ishkanov [85] have measured similar resonances as well. Similar resonances are shown to appear for the isotopes ^{58,60}Ni in Ref. [87] from 1969, and the same writer of this paper, A. M. Goryachev, over 10 years later in 1982 [84] ends up with a remarkably smooth cross section. It also looks somewhat similar to the unfolded, monochromatic spectrum of our experiment as shown in Figure 5.2. His results also look similar to my attempt of using MCMC-unfolding with a very strict smoothing factor, as shown in Figure 4.16, where I suspect may have been suppressing actual resonances. In the '69 article however, Goryachev discusses particle-hole coupling as an explanation, and states that *"The quadrupole surface oscillations are not the only collective degree of freedom whose interaction gives rise to the intermediate structure of the giant resonance. Calculations have shown that for magic nuclei an important role in the formation of the structure and the width of the giant resonance is played by collective states of higher multipolarity (3^- and 5^-)"* [87]. Explaining the width and the structure of the giant dipole resonance still remains an open question, but something interesting is definitely going on in this area.

The cross section is a useful result by itself, and is great for comparison with previous data. But our goal is to use this cross section to calculate the γ-ray strength function for higher energies, and fuse it together with the Oslo-data at lower energies. By multiplying by the factor 8.674e-8, and dividing the unfolded cross section by the maximum γ-energy, the resulting γ-ray strength function is plotted in Figure 5.3. Again, the resonances in the GDR region are reflected in the γSF as well.

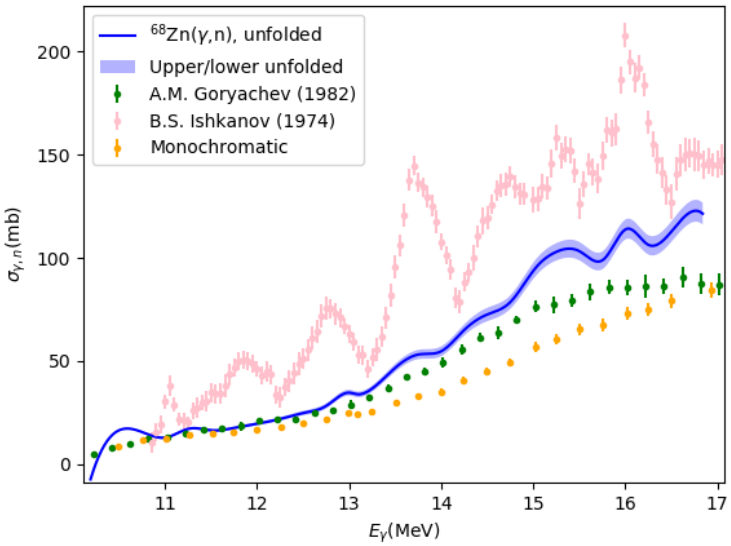

Figure 5.2: The calculated unfolded cross section from the ^{68}Zn(γ,n)-data, compared with previous experimental data from Ref. [84] and [85], and the previously calculated monochromatic cross section.

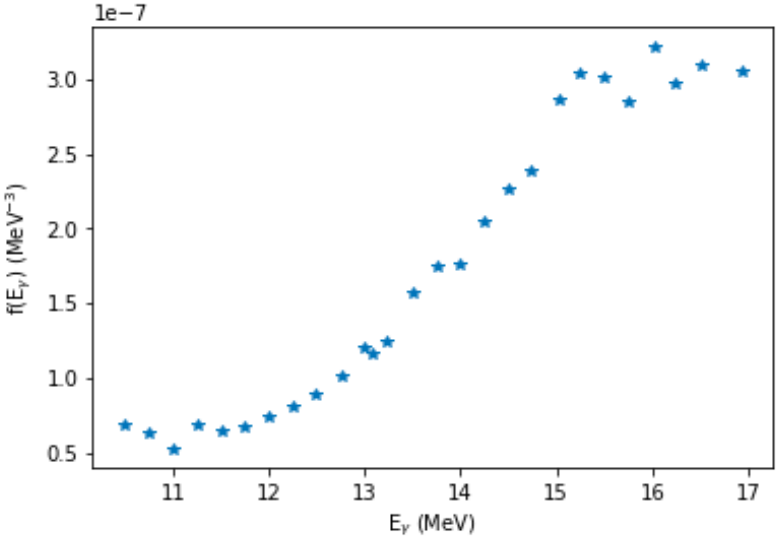

Figure 5.3: The calculated γ-strength function from the ^{68}Zn(γ,n)-data.

5.3 Interpolating the γ-ray Strength Functions

I have experimentally and analytically determined the γ-ray strength function of ^{68}Zn from the (γ, n) and (p, p')-experiments, in the energy regions where the experimental data is valid and trustworthy. Due to experimental limitations around the neutron separation energy S_n there is a gap in our knowledge in this area. As the goal is to have a broader understanding of this nucleus behavior, I estimated as best I could the shape the γSF will take in this mid region, connection the lower energy region of data from Oslo to the higher energy region of data from Japan. In order to understand the physics behind the γ-strength function, it is important to understand the systematics of the different resonance models we will use to do so. In section 2.3 the theoretical foundation behind this section is covered.

5.3.1 E1-Strength Function Fit

A simple estimation for the γSF was found by doing a fit of the E1 component of the γSF, which should reflect the main shape of the function. To do this, I chose a two-component generalized Lorentzian in order to estimate the shape of the GDR-resonance, which we know for certain is present. The extra component is needed to account for slight deformations, and deviations from a spherical nucleus. In Figure 5.4 the fit of only an E1 two-component generalized lorentzian is plotted along with the data sets. The fit desperately needs an upbend, when comparing with the Oslo Method prediction of the strength function shape for lower energies. ^{68}Zn has through the analysis proven to look quite resonant. Both the strength function from (γ,n)-data, and the (p,p')-data have interesting bumps, which makes the very straight line between the two data sets rather suspicious-looking. This is why I decided, that as a pygmy has been measured to exist in Ref. [88], this should be implemented as well in the space between them. However, in all honesty, I can only guess what is going on in the blank space between 8 and 12 MeV.

5.3.2 E1 + M1 Component Strength Function Fit

To estimate the M1-component, I applied resonances that are likely to exist, like the low-energy enhancement. This was modelled as a standard lorentzian with an M1 spin flip. An extra component representing the pygmy-resonance was added by applying the knowledge from experimental data in Ref. [88]. A plot from this reference of the pygmy is shown in Figure 5.5. This gives an interesting, but fitting pygmy-bump in the unknown region. But since the data from Ref. [88] only tells us about the region where it appears, and not about the amplitude of the resonance, it is hard to tell if this is strictly correct. But all in all, the fit looks good and both data sets are complementing each other in this new representation of the γ-strength function of ^{68}Zn (see Figure 5.6).

The parameters used for making the fits were found by starting out with the formulas in Eq.(2.17), and with the parameters set to an educated guess from previous experience, before applying the fit to experimental data. Using the Fit

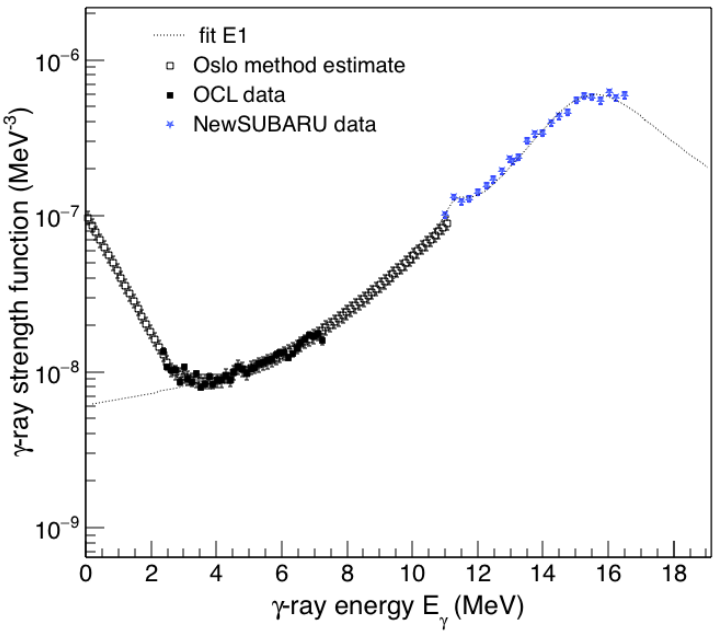

Figure 5.4: The E1-interpolation of the γ-ray strength function, from the lower energy OCL data, towards the higher energy NewSUBARU data.

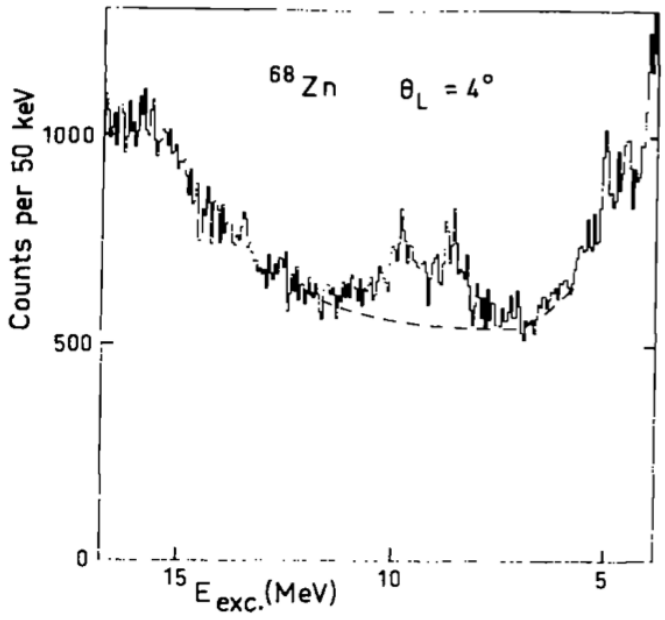

Figure 5.5: Figure taken from Ref. [88], where a pygmy resonance structure was measured at around 9 and 7 MeV. I used a simplified average of these as a pygmy resonance in our M1-component.

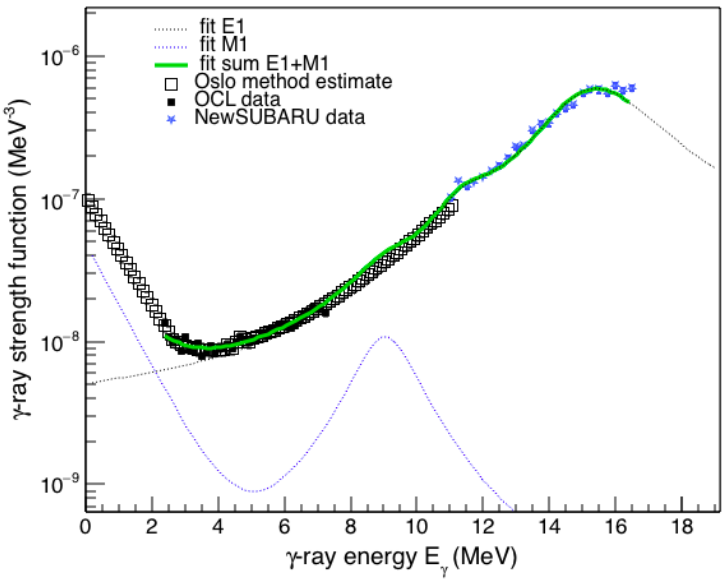

Figure 5.6: The complete interpolation of the γ-ray strength function, from the lower energy OCL data, towards the higher energy NewSUBARU data. In the middle energy region, a pygmy resonance (probably caused by E1, but included in the M1), gently guides the function up towards the resonant higher energy data.

method implemented in ROOT our data was made into histograms of classes TH1, fitting the data programmatically. The pygmy-parameters were set to be fixed values to reproduce the enhancement from Ref. [88]. The temperature parameter was a fixed constant temperature, but will differ given what the assumptions were in the method. This means that a change in the normalization parameters for instance, will affect this fixed parameter. The rest of the parameters concerning the E1 resonance will be set as free values. The upbend-parameter η_{upb} had to be limited to the maximum value 1.00, as to reproduce the predictions from the Oslo Method, which I deem reasonable to trust. The resulting parameters are given in table 5.1 and the resulting interpolation is shown to fit quite well in 5.6.

The uncertainties in this fit do not reflect the statistical uncertainty, and to explore the sensitivity of our data, a comparison of the most extreme values of the normalization parameters D_0 and $\Gamma_{\gamma 0}$ is shown in Table 5.2. Here it is displayed that changing these parameters within the statistical uncertainty that lies behind the estimation will vary the parameter results of this fit. The GEDR E and Γ-parameters, seem to vary around $\pm$ 0.1-0.3 MeV. For the temperature T, the variation is about 0.1. It therefore does not seem like the systems calculated energy and temperature is too sensitive to the statistical errors in these parameters. However, it is good to keep in mind that these variations could be hiding in the background, adding to the total uncertainty of our fit. The upbend constant c_{upb} on the other hand, shows a sensitivity of $\pm 1 \cdot 10^{-8}$,

which is relatively significant for such low energies. It seems like the upbend parameter might be the most sensitive and must therefore be carefully adjusted.

The resulting γSF in Figure 5.6 reflects all the resonances I believe to be present, and these estimations of the E1 and M1 component can be now used in TALYS to calculate the neutron capture reaction rate for the energy interval represented in the fitted function.

$E_{r1}(MeV)$	$\Gamma_{r1}(MeV)$	$\sigma_{r1}(mb)$	$E_{r2}(MeV)$	$\Gamma_{r2}(MeV)$	$\sigma_{r2}(mb)$
15.76	3.30	125.78	11.65	1.51	9.61
T (MeV)	$E_{pyg}(MeV)$	$\Gamma_{pyg}(MeV)$	$\sigma_{pyg}(mb)$	c_{upb}	η_{upb}
1.18	9.10	2.00	1.13	$4.87{\cdot}10^{-8}$	1.00

Table 5.1: The numerically fitted parameters for the GEDR (r1 and r2) and GMDR (featuring the pygmy resonance), and the upbend constants. Here we used the middle D_0 and $\Gamma_{\gamma 0}$ as given in [72].

Parameter	$D_0 + \sigma_{D_0}$	$D_0 - \sigma_{D_0}$	$\Gamma_{\gamma 0} + \sigma_{\Gamma_{\gamma 0}}$	$\Gamma_{\gamma 0} - \sigma_{\Gamma_{\gamma 0}}$
E_{r1} (MeV)	15.82	15.91	15.97	15.74
Γ_{r1} (MeV)	3.41	3.58	3.66	3.25
σ_{r1} (mb)	126.44	127.61	128.9	125.6
E_{r2} (MeV)	11.58	11.50	11.47	11.68
Γ_{r2} (MeV)	1.46	1.42	1.52	1.53
σ_{r2} (mb)	8.92	7.92	7.33	9.87
T (MeV)	1.21	1.25	1.28	1.17
c_{upb}	$5.05 \cdot 10^{-8}$	$5.33 \cdot 10^{-8}$	$5.57 \cdot 10^{-8}$	$4.80 \cdot 10^{-8}$
η_{upb}	1.00	1.00	1.00	1.00

Table 5.2: A sensitivity analysis of the input normalization parameters from [72], varying them one by one to the possible maximum and minimum value as given by the uncertainty σ. These are the numerically fitted parameters for the GEDR (r1 and r2) and the upbend constants. The pygmy-parameters are fixed to reflect [88] and therefore not sensitive to changes in D_0 and $\Gamma_{\gamma 0}$.

5.4 TALYS-Calculations

5.4.1 About TALYS

Today experimental data covers only a small fraction of the necessary information we need for performing calculations for nuclear physics applications, like nuclear astrophysics, reactor physics, medical physics and the production of radioisotopes etc. Even if we came around and measured and fully understood stable isotopes, which we still do not, there are still many reactions of interest involving unstable or even exotic nuclei. For these, little experimental data exist. Another limit on our experimental data is the energy range which we have available in our experimental setups. To fill these gaps, we need theoretical predictions. We can simulate nuclear reactions using TALYS [15], a software including many theoretical models covering all relevant reaction mechanisms met in light particle-induced nuclear reactions. The energy span that is most well defined is between 1 keV to 200 MeV, and target nuclei can have mass numbers between 12 and 339. Reaction channels and observables are described, and the simulations account for all types of compound, direct or pre-equilibrium mechanisms. Experimental information measured on mass, deformation, level densities etc., is considered by the algorithm if available. If no such experimental measurements are found, models will take its place representing theoretical properties of structure, potentials, level densities etc.

TALYS is designed to calculate cross sections, energy spectra, angular distributions and astrophysical reaction rates evaluated by the Hauser-Feschbach model [89]. This model relies of the fundamental Bohr hypothesis [19] of capture occurring as an intermediary production of a compound system which can reach a state of thermodynamic equilibrium (the pre-equilibrium[90]). When we look at compound nucleus reactions, exit channel is independent of the input channel, which makes it possible to implement such a statistical model as the H.F., as the decay of the compound nucleus only depends on its properties [91]. The model gives the energy averaged cross sections, while conserving relevant quantum numbers and its energy. TALYS is limited by this Hauser-Feshbach requirement of conservation, as this may not be fulfilled. If other decays than compound decay happen, like a pre-equillibrium decay where similar wave functions are factored, the theory does not allow it. This happens for instance in elastic channel reactions, where entrance and exit channels have the same transmission coefficient. To avoid this happening, a correction of width fluctuation correction should be introduced. Another weak spot of TALYS is the areas of nuclear physics where less experimental data causes the code to extrapolate input values like mass, half life and so on. This of course adds to the uncertainty of the end product, as we can not know if these guesses are correct. [91]

5.4.2 TALYS Results

After performing the interpolation, I created a suitable output of the E1 and M1 component: into files which are of the format TALYS wants (see Appendix B and C). Running the TALYS calculations I wanted to study the Reaction Rate and the Maxwellian-average Cross Sections (MACS) (see section 2.5), and compare the two to known values, and take a look at how the neutron strength function compares to the normalization data.

To run a standard TALYS calculation, in order to compare with what it calculates for currently existing data and integrated models, I started out with a simple inputfile:

```
projectile n
ejectiles g
element Zn
mass 67
energy energies.txt

Ntop 30 68 47
gnorm 1.
outlevels y
outdensity y
outgamma y

astro y
```

TALYS has access to available experimental data and does produce semi-believable results for the more stable isotopes, so I want to study whether this new data can enhance the credibility of the calculated reaction rates. One of the first ways one can improve the standard, is by adjusting only a couple parameters in the Constant Temperature model, using the parameters for temperature T = 1.14 and energy shift E0 = -1.319544, which I found in the Oslo Method to reduce the χ^2 error the most. The commands I used to make this adjustment are the following:

```
T 30 68 1.14
E0 30 68 -1.319544
Exmatch 30 68 11
```

Here the last command Exmatch sets the matching energy between the constant temperature and Fermi gas region. I set it quite high (11 MeV), to make sure it did not affect the data as I have seen no apparent shift to a Fermi-gas region. In Figure 5.7 a comparison of the standard TALYS representation (see appendix A to see what models choices are standard) of the level density of ^{68}Zn is presented, together with an attempt of improving these standard models by inputting new T and $E0$ parameters. Seemingly, these new parameters do make the level density match the Oslo Method data better, which is what we want in order to apply this level density to further calculations later and know that it is truly a representative estimation of our data. Now that I had improved the TALYS models with level density data giving the Constant Temperature model more

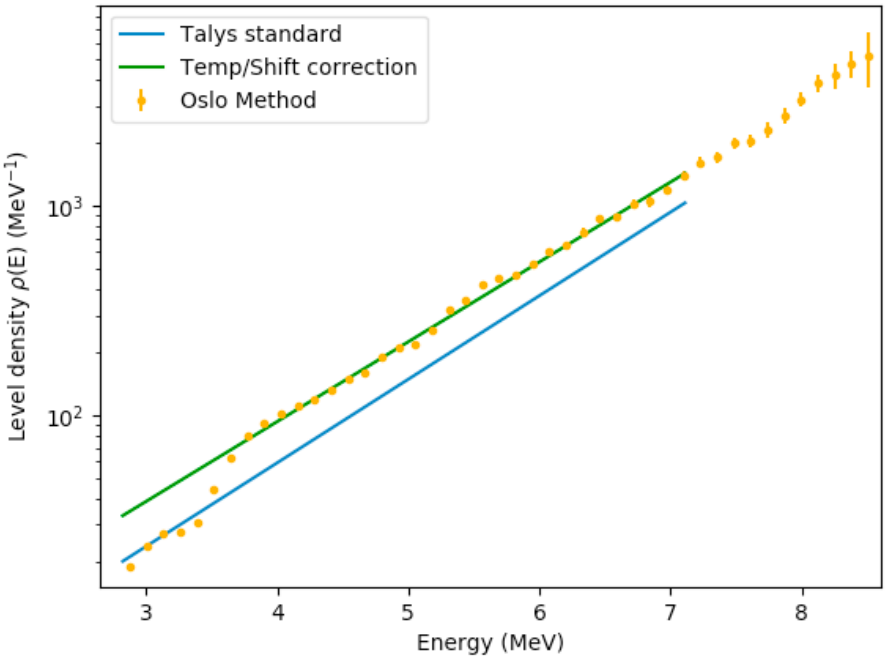

Figure 5.7: Showing that by editing the parameters T and E0 in TALYS (temperature and energy shift), we achieve a representation of the level density close to our Oslo Method results. This is ideal to use for further enhancement of the Reaction Rate calculations.

fitting parameters, I wanted to use the γ-ray strength function as an input as well. This can be done using the commands E1file and M1file, reading in the estimated E1 and M1 components separately.

```
Strength 3
E1file 30 68 E1_gsf_68Zn_middle.txt
M1file 30 68 M1_gsf_68Zn_middle.txt
```

This is how you read in E1/M1 files in TALYS, with a filename of your choosing. The Strength 3 command was necessary in order to be able read the E1-file correctly, due to a bug which is hopefully soon dealt with. But for now, in TALYS 1.9, that command is a must. In Appendix B and C are attatched the exact files I used as input E1 and M1 files for TALYS. The format of these input files is very important, so these two can serve as an example.

One of the main goals, if not the main goal of this thesis, was to calculate the Reaction Rate of the ^{67}Zn(n,γ)^{68}Zn reaction. This was quite easily done in TALYS (although a bit time consuming) using the **astro y** command. This will output the Reaction Rate and the Maxwellian Average cross section (MACS, which we will get back to) as a function of temperature T (GK) (see section 2.5 for the theoretical details of these calculations). By doing TALYS calculations for the TALYS Standard (see Appendix A) reaction rate, the level density improved reaction rate and lastly the γ-strength function + level density im-

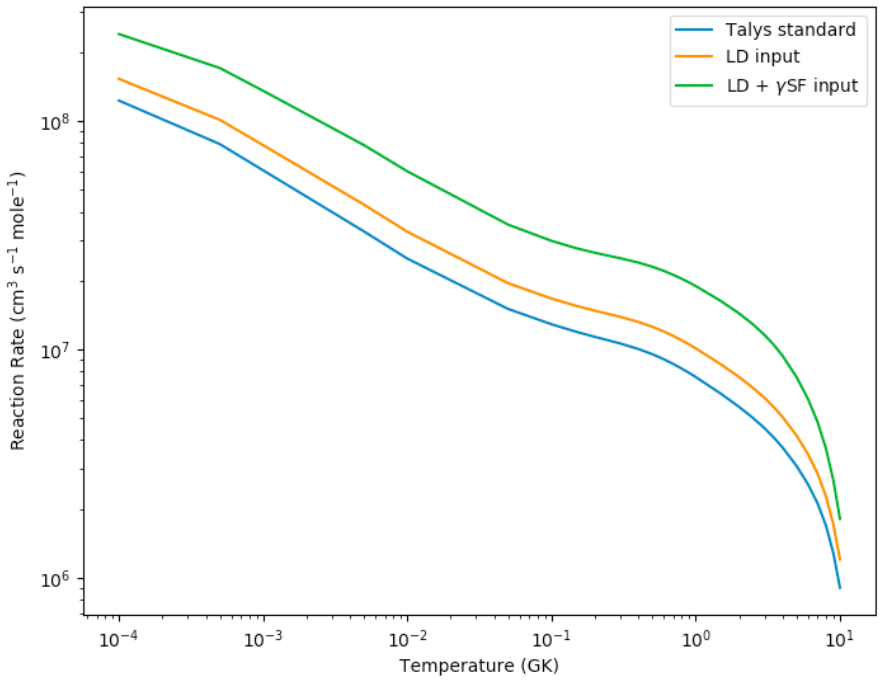

Figure 5.8: The calculated reaction rate for the neutron capture reaction ^{67}Zn(n,γ)^{68}Zn. Shown is the calculation TALYS standard, see Appendix A, would calculate from previously featured measurements and implemented models, versus what it looks like if we correct for our level density extracted by the Oslo Method, and also for an additional input of the E1/M1-component from the experimentally extracted γ-ray strength function.

proved reaction rate, in Figure 5.8 it looks like the new measurements push the rates higher and closer to the experimental data. This seems to be fitting, but to check if this is really an improvement of the TALYS standard model calculations, comparisons with other experimental data sets are necessary. I chose to compare our results with data found on KaDoNiS [92]. This database contains calculated neutron cross sections performed in Ref. [93] from various data sources and experiments. In our case, Ref. [94] have performed high-resolution measurements on the neutron capture cross sections using the neutron time of flight technique at the pulsed Oak Ridge Electron Linear Accelerator in 1992. The MACS calculated in Ref. [93] from these data is plotted as blue stars in Figure 5.9. In the same figure "This work", the complete improved calculation with all corrections from our experiment, is plotted, and it looks like it fits the expected MACS much better than the TALYS standard calculation. I now have further reason to believe my results are trustworthy. In Figure 5.10 the uncertainty given at 30 keV approaches our resulting value, even with this being the seemingly worst estimated point. It is stated at the KaDoNis website [92] that the relative uncertainty for the other points will be of the same magnitude as the one given at 30 keV, so we seem to be well within this uncertainty overall.

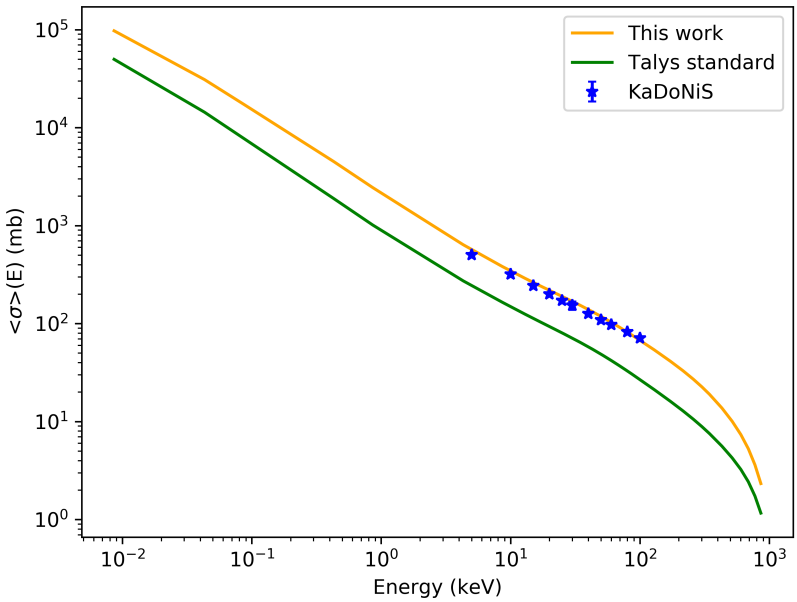

Figure 5.9: The Maxwellian averaged Cross Section for the neutron capture reaction on ^{67}Zn, with TALYS Standard (A) input compared to our enhancement using level density and γ-ray strength function data as input. For reference the only data available is the MACS from KaDoNiS [92], which goes well with the new fit.

For the S-process, which is assumed to work in the energy region from 10-100 keV, the data from KaDoNis fit very closely to our calculations. The KaDoNis data is currently what is being used for S-process reaction network calculations, so seeing how similar our constrained calculations come out, it is reasonable to assume that using this exact result as an input in a reaction network calculation of the S-process is not going to affect the resulting solar system abundances in a significant way.

In Figure 5.11 the calculation of the experimentally constrained reaction rate is compared to the standard TALYS calculation as it is today, and also the JINA-Reaclib [95] estimated reaction rate. In the energy region 10^2-10^3, the r-process is assumed to dominate the production of heavy elements as a result of neutron capture. This region is not covered by previously measured data in KaDoNiS [92], and for r-process reaction network calculations, the JINA-Reaclib [95] database is currently used as input. Reaclib uses a variety of references and models, and in this case they actually suggested the KaDoNiS V0.3 refit 2017 [92] as the recommended choice. In contrary to the previous KaDoNiS data set, which are experimentally measured, these are just a fit to those data using many parameters. What can be seen is that my constrained TALYS-calculation of the reaction rate in this region relevant to the r-process, fits very well to the

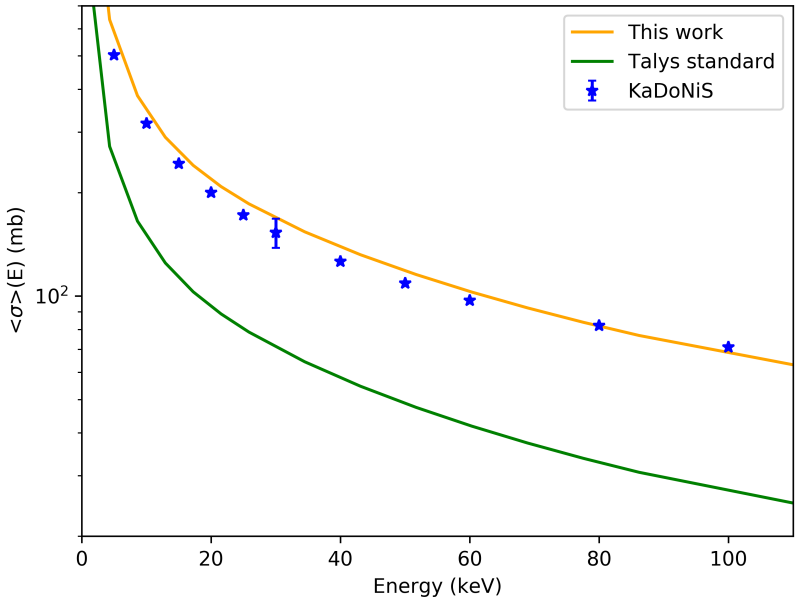

Figure 5.10: The Maxwellian averaged Cross Section for the neutron capture reaction on ^{67}Zn, with TALYS Standard (see Appendix A) input compared to our enhancement using level density and γ-ray strength function data as input. For reference the only data available is the MACS from KaDoNiS [92], which goes well with the new fit. The uncertainty at 30 keV is in given in [92], and it is stated that all other uncertainties will have a similar relative uncertainty to this point.

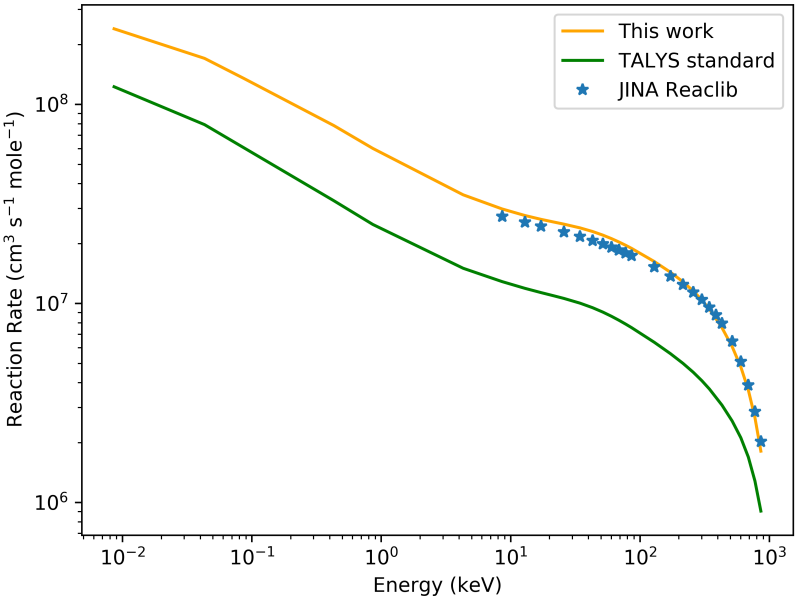

Figure 5.11: The calculated reaction rate for the neutron capture reaction on ^{67}Zn, with TALYS standard (see Appendix A) input compared to TALYS calculation using our new constraints on the nuclear level density and γ-ray strength function. For reference the r-process reaction network calculations use the JINA-Reaclib data [95], which goes well with the new fit. Our data seem to confirm these theoretically modelled points the r-process calculations usually assume.

numbers already in the JINA-Reaclib. So the data works well as a confirmation that this library is a good estimate still for this isotope. Seemingly, however, this data set as an input in r-process reaction rate networks will not affect the final distribution of the elements in the solar system, compared to the calculations being done already using modelled data from JINA. It shows that for this reaction, the database is trustworthy.

Lastly to compare our results, I looked at the neutron strength function parameter S_0. From ATLAS of Neutron Resonances [72] S_0= 1.98 $\cdot 10^{-4}$, while the output from TALYS states a theoretical S-wave strength S_0 = 13.20208 $\cdot 10^{-4}$. Ideally, adjustments to make these two match better should be done, but to do so is a long process of performing simulations and fitting models, which is unfortunately not doable in the time frame of this thesis. Some scientists may prefer to tweak parameters in the existing analysis to make this fit better, but this is a dangerous game to play as it may cause other aspects of the analysis to get severely flawed. Seeing as this is almost within order of magnitude correct, it is better for now to let this parameter be. In the future however, a better fit of the neutron strength could provide an improvement to these results.

Chapter 6

Conclusions and Outlook

In this work, experimental measurements were made in order to estimate the γ-ray strength function as well as the nuclear level density for ^{68}Zn. For lower energies both of these were extracted from (p,p')-data from the Oslo Cyclotron lab. For higher energies, the γ-ray strength function was determined using (γ, n)-data from the NewSUBARU facility. Normalization parameters used were found in ATLAS of Neutron Resonances [72]. The resulting level density shows a constant temperature tendency, see Figure 3.24, and the constant temperature model is used throughout the Oslo Method as it better fits trusted data points, see Figure 3.26. Both iterative matrix unfolding and Monte Carlo randomized unfolding were used to unfold the (γ,n) data, as previous measurements showed a disagreement between whether this isotopes strength function should contain resonances or not. The structure of ^{68}Zn unfolded by us definitely recognizes some of the structures from a previous experiment by Ishkanov [85], yet it looks like his data or method has been even more sensitive to the resonances. I also tried applied an extensive amount of smoothing, and ended up with a result resembling the non-resonant data set from Goryachev [84], so I believe that maybe some structures have been lost due to over smoothing in this case. My experimental data shows that there may indeed be interesting structures to this isotope.

The brand new detector array OSCAR has proven to be a great improvement to its predecessor CACTUS, in the sense that the energy resolution is now much better, and the timing gives us ns-precision. However, this being one of the first experiments to utilize this new instrument, new challenges were found. The energy resolution now makes it clear that for OSCAR, when calibrating the LaBr3:Ce-detectors, a linear calibration may not always be satisfactory. In the case of our data, the results from the Oslo Method shows that our calibration works fine for energies in this range. But a tendency of non-linear effects towards higher energies is definitely something to be aware of and to learn to work around in the future. Another potential issue now manifesting itself in the data, is an interpretation on 511 keV single-escape γ-rays as states in the nucleus. This is a problem in the Oslo method unfolding which will have to be resolved in the future for better results. A conclusive remark is that OSCAR is a definite improvement to the OCL, but also surprised the team with effects we did not expect to be dealing with.

Nevertheless, the data analysis still went decently, providing a meaningful data set for the cause of better understanding the neutron capture processes by gathering better data. Combining the two data sets, and performing a fit of E1 and M1 components to the experimental strength function data and previously measured data [88], I extracted the final γ-strength function as shown in Figure 5.6. The strength function shows a low energy enhancement, as well as a distinct GDR profile. A potential pygmy-resonance from a previous study [88] is included as well. A sensitivity analysis of the parameters used in the fit was performed, and is shown in Tables 5.1 and 5.2. The low energy enhancement region seems to be the most sensitive to slight parameter changes within the uncertainty limits stated in [72]. The sensitivity the upbend-region shows in this analysis, may also be reflected in the comparison between the Constant Temperature and Fermi Gas level density models, see Figure 3.26, where the Constant Temperature model is chosen due to its better fit in this particular area. This was the only area showing a significant sensitivity to the choice between those two level density models.

The experimentally constrained results of the Maxwellian-averaged cross section calculated at 30 keV: $<\sigma>_{(n,\gamma)} = 168.359$ is close to being within the uncertainty of experimental values available at KaDoNiS [92], $<\sigma>_{n,\gamma} = 153 \pm 15$ mb. This energy is the value which is the least agreeable to the KaDoNis data, as seen in Figure 5.10. This figure also shows the experimental constraints effect on the TALYS standard as is today, and it is definitely an improvement to the standard models of TALYS. However, s-process reaction network calculations are currently using KaDoNis data as input, so I can now confirm that by producing similar results to KaDoNiS, that the calculations are already using good values. Results in the r-process neutron energy region are compared with models from JINA-Reaclib [95], and shown to be in agreement as well, as shown in Figure 5.11. The measurements and calculations of ^{67}Zn(n,γ)^{68}Zn acquired in this experiment therefore acts as a confirmation that the reaction rates used in both the current s-process and r-process simulations of neutron reaction network calculations should be considered trustworthy. Therefore, I can at least rule out the reaction rate of this reaction as a large cause of error for calculations of the abundance of elements in the solar system. And by ruling out one potential source of error, we are one step closer to finding the real downfalls and correcting them.

Bibliography

[1] Los Alamos National Laboratory (2011), Periodic Table of Elements: LANL. Los Alamos, New Mexico: Los Alamos National Security, LLC. Retrieved 23 May 2019.

[2] NNDC, 2019, Interactive Chart of Nuclides, Retrieved 05.23.2019, available at https://www.nndc.bnl.gov/nudat2/

[3] National Research Council, Connecting Quarks with the Cosmos: Eleven Science Questions for the New Century. Washington, DC: The National Academies Press (2003).

[4] C. Iliadis, Nuclear Physics of Stars, John Wiley Sons (2015).

[5] K. Lodders, Solar System Abundances and Condensation Temperatures of the Elements. In: The Astrophysical Journal. 591, p. 1220–1247 (2003).

[6] C. Deaconu (2008): http://large.stanford.edu/courses/2008/ph204/deaconu1/

[7] A. C. Phillips, The Physics of Stars, 2nd Edition (Wiley, 1999).

[8] Burbidge, E. Margaret and Burbidge, G. R. and Fowler, William A. and Hoyle, F., Synthesis of the Elements in Stars, Rev. Mod. Phys. 29, 547 (1957).

[9] A. G. W. Cameron, Nuclear Reactions in Stars and Nucleogenesis, Astronomical Society of the Pacific, Vol. 69, No. 408, p.201 (1957).

[10] Merrill, P. W., Technetium in the stars, Science 115 2992: 479-89 [484] (1952).

[11] B. P. Abbott, R. Abbott, T. D. Abbott, et al. GW170817: Observation of Gravitational Waves from a Binary Neutron Star Inspiral. Phys. Rev, 119(16):30–33 (2017).

[12] A. Goldstein, P. Veres, E. Burns, et al. An Ordinary Short Gamma-Ray Burst with Extraordinary Implications: Fermi-GBM Detection of GRB 170817A. The Astrophysical Journal Letters, 848(2):L14 (2017).

[13] V. Savchenko, C. Ferrigno, E. Kuulkers, et al. INTEGRAL Detection of the First Prompt Gamma-Ray Signal Coincident with the Gravitational Wave Event GW170817. The Astrophysical Journal Letters, 848(2):L15 (2017).

[14] NASA's Goddard Space Flight Center/CI Lab, currently available at http://svs.gsfc.nasa.gov/12949

[15] A. Koning, S. Hilaire and S. Goriely, TALYS - 1.8 User Manual, (2015).

[16] A.C.Larsen, A. Spyrou, S.N.Liddick et Al., Novel techniques for constraining neutron-capture rates relevant for r-process heavy-element nucleosynthesis. Progress in Particle and Nuclear Physics (2019).

[17] N.Otuka, E.Dupont, V.Semkova and et. Al., Towards a More Complete and Accurate Experimental Nuclear Reaction Data Library (EXFOR): International Collaboration Between Nuclear Reaction Data Centres (NRDC), Nucl. Data Sheets 120 272 (2014).

[18] R. Capote, M. Herman, P. Oblozinsky and et. Al., Reference Input Parameter Library (RIPL-3), Nuclear Data Sheets - Volume 110, Issue 12, p 3107-3214, (2009).

[19] N.Bohr, Neutron Capture and Nuclear Constitiution, Nature 137, issue of 29 Feb, p 351, p 351 (1936).

[20] Spicer B.M., The Giant Dipole Resonance. In: Baranger M., Vogt E. (eds) Advances in Nuclear Physics. Springer, New York, NY (1969).

[21] J. M. Blatt and V. F. Weisskopf, Theoretical Nuclear Physics (John Wiley Sons, New York, 1952).

[22] Breit, G. and Wigner, E., Capture of Slow Neutrons, Phys. Rev. 49,7 p. 519-531 (1936).

[23] I. Gheorghe, doctoral thesis, Univerity of Bucharest (2017).

[24] H. Feshbach, C. E. Porter and V. F. Weisskopf, Model for Nuclear Reactions with Neutrons, Phys. Rev. 96, 448 (1954).

[25] G. Vladuca, Elemente de fizică nucleară. Bucureşti: Universitatea din Bucureşti, Facultatea de Fizică (1988).

[26] A. C. Larsen, Private Communication (May 2019).

[27] T. Ericson, The Statistical Model and Nuclear Level Densities, Adv. Phys., 9, p 425 (1960).

[28] H. A. Bethe, An attempt to calculate the number of energy levels of a heavy nucleus, Phys. Rev. 50(4) p 322-341 (1936).

[29] A. V. Ignatyuk and J. L. Weil, Density of discrete levels in 116Sn, Phys. Rev. C Vol. 47, Iss. 4 (1993).

[30] A. C. Larsen, J. E. Midtbø and M. Guttormsen et. al. Enhanced low-energy γ-decay strength of 70Ni and its robustness within the shell model, Phys. Rev. C 97, 054329 (2018).

[31] T. Egidy and D. Bucurescu, Systematics of nuclear level density parameters, Phys. Rev. C 72, 044311 (2005).

[32] T. Ericson, A Statistical Analysis of Excited Nuclear States, Nuclear Phys, A 11, 481, (1959).

[33] V. Zelevinsky, S. Karampagia and A. Berlaga, Constant Temperature Model for Nuclear Level Density, Phys Letters N 783, p 428-433 (2018).

[34] A. Gilbert and A. G. W. Cameron, A Composite Nuclear-Level Density Formula with Shell Corrections, Can. J Phys. 43, 1446 (1965).

[35] J. J. Atick and E. Witten, The Hagedorn transition and the number of degrees of freedom of string theory, Nuclear Physics B, p 291-334 (1988).

[36] Bartholomew et al., Gamma-Ray Strength Functions, Adv. Nucl. Phys. 7 p 299-324 (1973).

[37] P. A. M. Dirac, The quantum theory of the emission and absorption of radiation, Proc. R. Soc. Lond. Ser. A Math. Phys. Eng. Sci. 114 p 243–265 (1927).

[38] E. Fermi, Nuclear Physics, University of Chicago Press, formula VIII.2, (1950).

[39] P. Axel, Proceedings of the International Symposium on Nuclear Structure, Dubna, IAEA Vienna, p 299 (1968).

[40] V. Ponomarev, Pygmy Dipole Resonance, J. Phys.: Conf. Ser. 533, 012028 (2014).

[41] T. Renstrøm and et. Al. First evidence of low energy enhancement in Ge isotopes, EPJ Web of Conferences 93, 04003 (2015).

[42] A. Voinov, E. Algin, U. Agvaanluvsan and et. al., Large Enhancement of Radiative Strength for Soft Transitions in the Quasicontinuum, Phys. Rev. Lett. 93, 142504 (2004).

[43] A. C. Larsen and S. Goriely, Impact of a low-energy enhancement in the γ-ray strength function on the neutron-capture cross section, Phys. Rev. C 82, 014318 (2010).

[44] A. C. Larsen, N. Blasi, A. Bracco and et. al., Evidence for the Dipole Nature of the Low-Energy γ Enhancement in 56Fe, Phys. Rev. Lett. 111, 242504 (2013).

[45] Low-Energy Enhancement of Magnetic Dipole Radiation, R. Schwengner, S. Frauendorf and A. C. Larsen, Phys. Rev. Lett. 111, 232504 (2013).

[46] B. A. Brown and A. C. Larsen, Large Low-Energy M1 Strength for 56,57Fe within the Nuclear Shell Model, Phys. Rev. Lett. 113, 252502 (2014).

[47] E. Litvinova and N. Belov, Low-energy limit of the radiative dipole strength in nuclei, Phys. Rev. C 88, 031302(R) (2013).

[48] T. Belgya et al. Handbook for Calculations of Nuclear Reaction Data, RIPL-2, IAEA-TECDOC-1506 (IAEA, Vienna, 2006).

[49] D. M. Brink, Doctoral thesis, Oxford University (1955).

[50] OCL website: https://www.mn.uio.no/fysikk/english/research/about/infrastructure/OCL/index.html

[51] E. Lawrence and M. Livingston, The Production of High Speed Light Ions without the use of High Voltages, University of California (1932).

[52] W. Kleeven and S. Zaremba, Cyclotrons: Magnetic Design and Beam Dynamics, Ion Beam Applications, Louvain-La-Neuve, Belgium (2018).

[53] G. M. Tveten - Private communication (2018).

[54] E.V.D van Loef, P. Dorenbos and C.Q.E. van Eijk, High-energy-resolution scintillator: Ce3+ activated Labr3, Appl. Phys. Lett 79, 1573 (2001).

[55] MIT OpenCourseWare, Course of Origin: 20.309 Biological Engineering II: Instrumentation and Measurement (Fall 2006).

[56] F. Zeiser, Efficiency of OSCAR, unpublished (private communiaction).

[57] M. Guttormsen, A. Bürger, T.E. Hansen and N. Lietaer, The SiRi Particle-Telescope System, Nucl. Instr. and Meth. Phys. Res. A 648, p 168 (2011).

[58] W. R. Leo, Techniques for Nuclear and Particle Physics Experiments, Springer-Verlag, 24 (1994).

[59] R. Brun and F. Rademakers, ROOT - An Object Oriented Data Analysis Framework, Proceedings AIHENP'96 Workshop, Lausanne, Sep. 1996, Nucl. Inst. Meth. in Phys. Res. A 389 p 81-86 (1997).

[60] Vetle W. Ingeberg, fzeiser and Erlend Lima, oslocyclotronlab/Qkinz: Update (Version 1.3.3, 2018, March 23. 10.5281/zenodo.1206099)

[61] E.A. Mccutchan, Nuclear Data Sheets for A = 68, Nucl. Data Sheets 113, 1735 (2012).

[62] M. Shamsuzzoha Basunia, Nuclear Data Sheets for A = 28, Nucl. Data Sheets 114, 1189 (2013).

[63] M. Guttormsen, F. Zeiser, J. E. Midtbø, V. W. Ingeberg, A. C. Larsen, oslocyclotronlab/oslo-method-software: Oslo Method v1.1.2 doi:10.5281/zenodo.2318646

[64] M. Guttormsen et. al., The unfolding of continuum γ-ray spectra, Nuclear Instruments and Methods in Physics Research A 374, p 371-376 (1996).

[65] M. Guttormsen, Ten steps to heaven, Unpublished (2018).

[66] M. Guttormsen, T. Ramsøy, J. Rekstad, The first generation of γ-rays from hot nuclei, Nucl. Instrum. Methods Phys. Res. A 255, 518 (1987)

[67] J. E. Midtbø, Doctoral Thesis (2019)

[68] A. Schiller, L. Bergholt, M. Guttormsen, E. Melby, J. Rekstad and S. Siem, Extraction of level density and gamma strength function from primary gamma spectra, Nucl. Instr. and Meth. A 447 p 498-511 (2000).

[69] J.Kopecky and M.Uhl, Phys. Rev. C41, 1941 (1990).

[70] T. Egidy and D. Bucurescu, Experimental energy-dependent nuclear spin distributions, Phys. Rev. C 80, 054310 (2009).

[71] G. Choudalakis, Fully Bayesian Unfolding, University of Chicago, Enrico Fermi Institute (2012).

[72] S.F. Mughabghab, Atlas of Neutron Resonances, Volume 1: Resonance Properties and Thermal Cross Sections Z=1-60 (2018)

[73] RIKEN/JASRI-website: http://www.spring8.or.jp/en/about_us/whats_sp8/

[74] Google Maps, May 2019, maps.google.com.

[75] P. Elleaume, Optical Klystrons, Journal de Physique Colloques, 44 (C1), pp.C1-333-C1-352 (1983).

[76] LASTI Annual Report Vol. 18. (2016).

[77] University of Hyogo, NewSUBARU Synchrotron Radiation Facility website: http://www.lasti.u-hyogo.ac.jp/NS-en/facility/bl01/

[78] G.B. Rybicki and A.P. Lightman, Radiative Processes in Astrophysics, Harvard-Smithsonian Center for Astrophysics, p 195-199 (1979).

[79] National Institutes for Quantum and Radiological Science and Technology, Project LCS gamma-ray website (2017): http://www.taka.qst.go.jp/tokai_center/lcs_en/

[80] H. Utsunomiya, T. Renstrøm, G. M. Tveten and et. al., γ-ray strength function for thallium isotopes relevant to the ^{205}Pb $-^{205}$ Tl chronometry, Phys. Rev. C 99, 024609 (2019).

[81] B. L. Berman, J. T. Caldwell, R. R. Harvey and et. al, Photoneutron Cross Sections for Zr90, Zr91, Zr92, Zr94, and Y89, Phys. Rev. 162, 1098 (1967).

[82] T. Shima and H. Utsunomiya, Proceedings of the Nuclear Physics and Gamma- ray Sources for Nuclear Security and Nonproliferation, World Scientific Publishing, Singapore (2014).

[83] H. Utsunomiya and et al., IEEE Trans. Nucl. Sc., vol 61 (2014).

[84] A.M.Goryachev and G.N.Zalesnyy, The studying of the photoneutron reactions cross sections in the region of the giant dipole resonance in zinc, germanium, selenium, and strontium isotopes. Voprosy Teoreticheskoy i Yadernoy Fiziki, Vol.1982, Issue.8, p 121 (1982).

[85] B.S.Ishkhanov, I.M.Kapitonov, E.V.Lazutin, I.M.Piskarev, O.P.Shevchenko. Photoneutron Cross Sections for 64Zn and 68Zn in the Giant Resonance Region. Yadernaya Fizika, Vol.20, p.433 (1974).

[86] M. D. Jones and et. Al., Examination of the low-energy enhancement of the γ-ray strength function of 56 Fe, Phys. Rev. C 97, 024327 (2018).

[87] B. I. Goryachev, B.S. Ishkanov and et. al., Giant Dipole Resonance on Ni Isotopes, Yad. Fiz. 10, 252—259 (1969).

[88] C. Djalali et al., Systematics of the excitation of M1 Resonances in medium heavy nuclei by 200 MeV proton inelastic scattering, Nuclear Physics A388 1-18 (1982).

[89] W. Hauser, H. Feshbach, The Inelastic Scattering of Neutrons, Phys.Rev.87, 366 (1952).

[90] S. Goriely, S. Hilaire and A. Koning, Improved predictions of nuclear reaction rates with the TALYS reaction code for astrophysical applications (2008).

[91] S. Goriely, Optical model and compound nucleus model, Lecture at University of Stellenbosch (Nov. 2017).

[92] I. Dillmann, M. Heil, F. Käppeler and et. al., KADoNiS - The Karlsruhe Astrophysical Database of Nucleosynthesis in Stars. AIP Conf. Proc. 819, 123; online at $http://www.kadonis.org$.

[93] Z. T. Bao, H. Beer, F. Käppeler and et. al. Neutron Cross Sections for Nucleosynthesis Studies. Atomic Data and Nuclear Data Tables 76 70 (2000).

[94] H. Agrawal et al., High-resolution neutron total and capture cross sections in 67Zn, J. Phys. G: Nucl. Part. Phys. 18, 1069 (1992).

[95] R. H. Cyburt et al., The JINA Reaclib Database: Its recent updates and impact on type-I X-ray Bursts, ApJS 189 (2010) 240; online at http://reaclib.jinaweb.org.

Appendices

Appendix A

TALYS standard

```
TALYS-1.9 (Version: December 21, 2017)

Copyright (C) 2017  A.J. Koning, S. Hilaire and S. Goriely
                        IAEA         CEA          ULB

Dimensions - Cross sections: mb, Energies: MeV, Angles: degrees

########## USER INPUT ##########

USER INPUT FILE

#
# talys input file, 67zn(n,g)68zn
#
# hfb08, mughabghab d0 = 367 ev, <gg> = 440 mev

projectile n
ejectiles g
element zn
mass 67
energy energies.txt

equidistant y

ntop 30 68 47

preequilibrium y
outspectra y
fileresidual y
outbasic y

gnorm 1.
localomp n
```

```
outlevels y
outdensity y
outgamma y

astro y

USER INPUT FILE + DEFAULTS

Keyword           Value   Variable     Explanation

#
# Four main keywords
#
projectile          n     ptype0       type of incident particle
element            Zn     Starget      symbol of target nucleus
mass               67     mass         mass number of target nucleus
energy energies.txt       energyfile   file with incident energies
#
# Basic physical and numerical parameters
#
ejectiles g               outtype      outgoing particles
maxz               12     maxZ         maximal number of protons away
                                       from the initial compound nucleus

maxn               32     maxN         maximal number of neutrons away
                                       from the initial compound nucleus

bins               40     nbins        number of continuum excitation energy bins

equidistant         y     flagequi     flag to use equidistant excitation bins
                                       instead of logarithmic bins

popmev              n     flagpopmev   flag to use initial population per MeV
                                       instead of histograms

segment             1     segment      number of segments to divide emission
                                       energy grid

maxlevelstar       30     nlevmax      maximum number of included discrete
                                       levels for target

maxlevelsres       10     nlevmaxres   maximum number of included discrete
                                       levels for residual nucleus

maxlevelsbin g     10     nlevbin      maximum number of included discrete
                                       levels for gamma channel

maxlevelsbin n     30     nlevbin      maximum number of included discrete
                                       levels for neutron channel
```

maxlevelsbin p	10	nlevbin	maximum number of included discrete levels for proton channel
maxlevelsbin d	5	nlevbin	maximum number of included discrete levels for deuteron channel
maxlevelsbin t	5	nlevbin	maximum number of included discrete levels for triton channel
maxlevelsbin h	5	nlevbin	maximum number of included discrete levels for helium-3 channel
maxlevelsbin a	10	nlevbin	maximum number of included discrete levels for alpha channel
ltarget	0	ltarget	excited level of target
isomer	1.00E+00	isomer	definition of isomer in seconds
transpower	15	transpower	power for transmission coefficient limit
transeps	1.00E-15	transeps	limit for transmission coefficient
xseps	1.00E-25	xseps	limit for cross sections
popeps	1.00E-25	popeps	limit for population cross section per nucleus
Rfiseps	1.00E-06	Rfiseps	ratio for limit for fission cross section per nucleus
elow	1.00E-06	elow	minimal incident energy for nuclear model calculations
angles	90	nangle	number of angles
anglescont	18	nanglecont	number of angles for continuum
anglesrec	1	nanglerec	number of recoil angles
maxenrec	20	maxenrec	number of recoil energies
channels	n	flagchannels	flag for exclusive channels calculation
maxchannel	4	maxchannel	maximal number of outgoing particles in individual channel description
micro	n	flagmicro	flag for completely microscopic Talys calculation

best	n	flagbest	flag to use best set of adjusted parameters
bestbranch	y	flagbestbr	flag to use flag to use only best set of branching ratios
bestend	n	flagbestend	flag to put best set of parameters at end of input file
relativistic	y	flagrel	flag for relativistic kinematics
recoil	n	flagrecoil	flag for calculation of recoils
labddx	n	flaglabddx	flag for calculation of DDX in LAB system
recoilaverage	n	flagrecoilav	flag for average velocity in recoil calculation
channelenergy	n	flagEchannel	flag for channel energy for emission spectrum
reaction	y	flagreaction	flag for calculation of nuclear reactions
astro	y	flagastro	flag for calculation of astrophysics reaction rate
astrogs	n	flagastrogs	flag for calculation of astrophysics reaction rate with target in ground state only
astroex	n	flagastroex	flag for calculation of astrophysics reaction rate to long-lived excited states
nonthermlev	-1	nonthermlev	excited level non-thermalized in the calculation of astrophysics rate
massmodel	2	massmodel	model for theoretical nuclear mass
expmass	y	flagexpmass	flag for using experimental nuclear mass if available
disctable	1	disctable	table with discrete levels
production	n	flagprod	flag for isotope production
outfy	n	flagoutfy	flag for output detailed fission

```
                                        yield calculation

gefran          50000     gefran        number of random events for GEF
                                        calculation

Estop         1000.000    Estop         incident energy above which TALYS
                                        stops

rpevap              n     flagrpevap    flag for evaporation of residual
                                        products at high incident energies

maxZrp             12     maxZrp        maximal number of protons away from
                                        the initial compound nucleus before
                                        residual evaporation

maxNrp             32     maxNrp        maximal number of neutons away from
                                        the initial compound nucleus before
                                        residual evaporation
#
# Optical model
#
localomp            n     flaglocalomp  flag for local (y) or global (n)
                                        optical model

dispersion          n     flagdisp      flag for dispersive optical model

jlmomp              n     flagjlm       flag for using semi-microscopic
                                        JLM OMP

optmodall           n     flagompall    flag for new optical model
                                        calculation for all residual nuclei

incadjust           y     flagincadj    flag for OMP adjustment on incident
                                        channel also

omponly             n     flagomponly   flag to execute ONLY an optical
                                        model calculation

autorot             n     flagautorot   flag for automatic rotational coupled
                                        channels calculations for A > 150

spherical           n     flagspher     flag to force spherical optical model

coulomb             y     flagcoulomb   flag for Coulomb excitation
                                        calculation with ECIS

statepot            n     flagstate     flag for optical model potential
                                        for each excited state

maxband             0     maxband       highest vibrational band added
```

```
                                        to rotational model

maxrot              2     maxrot        number of included excited
                                        rotational levels

sysreaction               sysreaction   particles with reaction cross
                                        section from systematics

rotational   n            rotational    particles with possible rotational
                                        optical model

core               -1     core          even-even core for weakcoupling
                                        (-1 or 1)

ecissave            n     flagecissave  flag for saving ECIS input and
                                        output files

eciscalc            y     flageciscalc  flag for new ECIS calculation for
                                        outgoing particles and energy grid

inccalc             y     flaginccalc   flag for new ECIS calculation for
                                        incident channel

endfecis            y     flagendfecis  flag for new ECIS calculation for
                                        ENDF-6 files

radialmodel         2     radialmodel   model for radial matter densities
                                        (JLM OMP only)

jlmmode             0     jlmmode       option for JLM imaginary potential
                                        normalization

alphaomp            6     alphaomp      alpha OMP (1=normal,
                                        2= McFadden-Satchler, 3-5= folding potential,
                                        6,8= Avrigeanu, 7=Nolte)

deuteronomp         1     deuteronomp   deuteron OMP (1=normal, 2=Daehnick,
                                        3=Bojowald, 4=Han-Shi-Shen, 5=An-Cai)
#
# Compound nucleus
#
widthfluc           7.052 ewfc          off-set incident energy for width
                                        fluctuation calculation

widthmode           1     wmode         designator for width fluctuation model

compound            y     flagcomp      flag for compound nucleus model

fullhf              n     flagfullhf    flag for full spin dependence of
                                        transmission coefficients
```

```
ecisccompound       n     flageciscomp flag for compound nucleus calculation
                                       by ECIS

cpang               n     flagcpang    flag for compound angular distribution
                                       calculation for incident charged particles

urr                 n     flagurr      flag for URR calculation

urrnjoy             n     flagurrnjoy  flag for normalization of URR parameters
                                       with NJOY method

lurr                2     lurr         maximal orbital angular momentum for URR
#
# Gamma emission
#
gammax              2     gammax       number of l-values for gamma multipolarity

strength            1     strength     model for E1 gamma-ray strength function

strengthM1          2     strengthM1   model for M1 gamma-ray strength function

electronconv        y     flagelectron flag for application of electron
                                       conversion coefficient

racap               n     flagracap    flag for radiative capture model

ldmodelracap        1     ldmodelracap level density model for direct radiative
                                       capture
#
# Pre-equilibrium
#
preequilibrium      y     flagpreeq    flag for pre-equilibrium calculation

preeqmode           2     preeqmode    designator for pre-equilibrium model

multipreeq         20.000 emulpre      on-set incident energy for multiple
                                       preequilibrium

mpreeqmode          2     mpreeqmode   designator for multiple
                                       pre-equilibrium model

breakupmodel        1     breakupmodel model for break-up reaction:
                                       1. Kalbach 2. Avrigeanu

phmodel             1     phmodel      particle-hole state density model

pairmodel           2     pairmodel    designator for pre-equilibrium
                                       pairing model
```

```
preeqspin           1     pespinmodel  model for pre-equilibrium spin
                                       distribution

giantresonance      y     flaggiant    flag for collective contribution
                                       from giant resonances

preeqsurface        y     flagsurface  flag for surface effects in
                                       exciton model

preeqcomplex        y     flagpecomp   flag for Kalbach complex particle
                                       emission model

twocomponent        y     flag2comp    flag for two-component
                                       pre-equilibrium model

ecisdwba            y     flagecisdwba flag for new ECIS calculation
                                       for DWBA for MSD

onestep             n     flagonestep  flag for continuum one-step direct only
#
# Level densities
#
ldmodel             1     ldmodelall   level density model

shellmodel          1     shellmodel   model for shell correction energies

kvibmodel           2     kvibmodel    model for vibrational enhancement

spincutmodel        1     spincutmodel model for spin cutoff factor for
                                       ground state

asys                n     flagasys     flag for all level density
                                       parameters a from systematics

parity              n     flagparity   flag for non-equal parity distribution

colenhance          n     flagcolall   flag for collective enahncement of
                                       level density for all nuclides

ctmglobal           n     flagctmglob  flag for global CTM model
                                       (no discrete level info)

gshell              n     flaggshell   flag for energy dependence of single
                                       particle level density parameter g
#
# Fission
#
fission             n     flagfission  flag for fission

fismodel            1     fismodel     fission model
```

```
fismodelalt         4     fismodelalt   alternative fission model for
                                        default barriers

hbstate             y     flaghbstate   flag for head band states in fission

class2              y     flagclass2    flag for class2 states in fission

massdis             n     flagmassdis   flag for calculation of fission
                                        fragment mass yields

ffevaporation       y     flagffevap    flag for calculation of particle
                                        evaporation from fission fragment
                                        mass yields

fisfeed             n     flagfisfeed   flag for output of fission per
                                        excitation bin

fymodel             2     fymodel       fission yield model, 1: Brosa 2: GEF

ffspin              n     flagffspin    flag to use spin distribution in
                                        initial FF population
#
# Output
#
outmain             y     flagmain      flag for main output

outbasic            y     flagbasic     flag for output of basic
                                        information and results

outpopulation       y     flagpop       flag for output of population

outcheck            y     flagcheck     flag for output of numerical checks

outlevels           y     flaglevels    flag for output of discrete
                                        level information

outdensity          y     flagdensity   flag for output of level densities

outomp              y     flagoutomp    flag for output of optical
                                        model parameters

outdirect           y     flagdirect    flag for output of direct
                                        reaction results

outinverse          y     flaginverse   flag for output of transmission
                                        coefficients and inverse reaction
                                        cross sections

outtransenergy      y     flagtransen   flag for output of transmission
```

			coefficients per energy
outecis	n	flagoutecis	flag for output of ECIS results
outgamma	y	flaggamma	flag for output of gamma-ray information
outpreequilibrium	n	flagpeout	flag for output of pre-equilibrium results
outfission	n	flagfisout	flag for output of fission information
outdiscrete	y	flagdisc	flag for output of discrete state cross sections
outspectra	y	flagspec	flag for output of double-differential cross sections
outbinspectra	n	flagbinspec	flag for output of emission spectrum per excitation bin
resonance	n	flagres	flag for output of low energy resonance cross sections
group	n	flaggroup	flag for output of low energy groupwise cross sections
addiscrete	y	flagadd	flag for addition of discrete states to spectra
addelastic	y	flagaddel	flag for addition of elastic peak to spectra
outangle	n	flagang	flag for output of angular distributions
outlegendre	n	flaglegendre	flag for output of Legendre coefficients
ddxmode	0	ddxmode	mode for double-differential cross sections
outdwba	n	flagoutdwba	flag for output of DWBA cross sections for MSD
outgamdis	n	flaggamdis	flag for output of discrete gamma-ray intensities
outexcitation	y	flagexc	flag for output of

```
                                        excitation functions

components          n     flagcompo     flag for output of
                                        cross section components

endf                n     flagendf      flag for information for ENDF-6 file

endfdetail          y     flagendfdet   flag for detailed ENDF-6
                                        information per channel

sacs                n     flagsacs      flag for statistical analysis
                                        of cross sections

partable            n     flagpartable  flag for output of model parameters
                                        on separate file

########## BASIC REACTION PARAMETERS ##########

Projectile          : neutron     Mass in a.m.u.      :   1.008665
Target              :  67Zn       Mass in a.m.u.      :  66.927127
```

Appendix B

TALYS input file: E1

```
Z=  30 A=  68
 U[MeV]  fM1[mb/MeV]
   0.100   5.885E-02
   0.200   5.939E-02
   0.300   5.993E-02
   0.400   6.048E-02
   0.500   6.103E-02
   0.600   6.158E-02
   0.700   6.214E-02
   0.800   6.271E-02
   0.900   6.328E-02
   1.000   6.386E-02
   1.100   6.445E-02
   1.200   6.505E-02
   1.300   6.566E-02
   1.400   6.628E-02
   1.500   6.692E-02
   1.600   6.757E-02
   1.700   6.823E-02
   1.800   6.891E-02
   1.900   6.961E-02
   2.000   7.032E-02
   2.100   7.106E-02
   2.200   7.181E-02
   2.300   7.259E-02
   2.400   7.339E-02
   2.500   7.421E-02
   2.600   7.506E-02
   2.700   7.594E-02
   2.800   7.684E-02
   2.900   7.778E-02
   3.000   7.874E-02
   3.100   7.974E-02
   3.200   8.078E-02
```

3.300	8.185E-02
3.400	8.296E-02
3.500	8.411E-02
3.600	8.530E-02
3.700	8.654E-02
3.800	8.782E-02
3.900	8.915E-02
4.000	9.053E-02
4.100	9.197E-02
4.200	9.346E-02
4.300	9.501E-02
4.400	9.663E-02
4.500	9.831E-02
4.600	1.001E-01
4.700	1.019E-01
4.800	1.038E-01
4.900	1.057E-01
5.000	1.078E-01
5.100	1.099E-01
5.200	1.121E-01
5.300	1.145E-01
5.400	1.169E-01
5.500	1.194E-01
5.600	1.221E-01
5.700	1.248E-01
5.800	1.277E-01
5.900	1.307E-01
6.000	1.338E-01
6.100	1.371E-01
6.200	1.405E-01
6.300	1.441E-01
6.400	1.479E-01
6.500	1.518E-01
6.600	1.560E-01
6.700	1.603E-01
6.800	1.648E-01
6.900	1.695E-01
7.000	1.745E-01
7.100	1.798E-01
7.200	1.853E-01
7.300	1.910E-01
7.400	1.971E-01
7.500	2.035E-01
7.600	2.103E-01
7.700	2.174E-01
7.800	2.249E-01
7.900	2.328E-01
8.000	2.411E-01
8.100	2.500E-01
8.200	2.594E-01

8.300	2.693E-01
8.400	2.798E-01
8.500	2.910E-01
8.600	3.029E-01
8.700	3.155E-01
8.800	3.290E-01
8.900	3.434E-01
9.000	3.588E-01
9.100	3.753E-01
9.200	3.931E-01
9.300	4.121E-01
9.400	4.326E-01
9.500	4.548E-01
9.600	4.788E-01
9.700	5.048E-01
9.800	5.330E-01
9.900	5.638E-01
10.000	5.974E-01
10.100	6.341E-01
10.200	6.743E-01
10.300	7.183E-01
10.400	7.664E-01
10.500	8.190E-01
10.600	8.763E-01
10.700	9.383E-01
10.800	1.005E+00
10.900	1.075E+00
11.000	1.148E+00
11.100	1.221E+00
11.200	1.294E+00
11.300	1.362E+00
11.400	1.425E+00
11.500	1.480E+00
11.600	1.527E+00
11.700	1.566E+00
11.800	1.600E+00
11.900	1.631E+00
12.000	1.661E+00
12.100	1.694E+00
12.200	1.732E+00
12.300	1.776E+00
12.400	1.827E+00
12.500	1.887E+00
12.600	1.956E+00
12.700	2.034E+00
12.800	2.123E+00
12.900	2.222E+00
13.000	2.333E+00
13.100	2.454E+00
13.200	2.588E+00

13.300	2.733E+00
13.400	2.891E+00
13.500	3.061E+00
13.600	3.244E+00
13.700	3.440E+00
13.800	3.648E+00
13.900	3.868E+00
14.000	4.099E+00
14.100	4.339E+00
14.200	4.588E+00
14.300	4.842E+00
14.400	5.098E+00
14.500	5.353E+00
14.600	5.603E+00
14.700	5.842E+00
14.800	6.065E+00
14.900	6.268E+00
15.000	6.445E+00
15.100	6.592E+00
15.200	6.704E+00
15.300	6.779E+00
15.400	6.816E+00
15.500	6.813E+00
15.600	6.773E+00
15.700	6.697E+00
15.800	6.590E+00
15.900	6.454E+00
16.000	6.295E+00
16.100	6.117E+00
16.200	5.925E+00
16.300	5.722E+00
16.400	5.514E+00
16.500	5.302E+00
16.600	5.091E+00
16.700	4.882E+00
16.800	4.676E+00
16.900	4.477E+00
17.000	4.284E+00
17.100	4.099E+00
17.200	3.921E+00
17.300	3.751E+00
17.400	3.590E+00
17.500	3.436E+00
17.600	3.290E+00
17.700	3.153E+00
17.800	3.022E+00
17.900	2.899E+00
18.000	2.782E+00
18.100	2.672E+00
18.200	2.568E+00

18.300	2.470E+00
18.400	2.377E+00
18.500	2.289E+00
18.600	2.206E+00
18.700	2.127E+00
18.800	2.053E+00
18.900	1.983E+00
19.000	1.916E+00
19.100	1.853E+00
19.200	1.793E+00
19.300	1.736E+00
19.400	1.682E+00
19.500	1.631E+00
19.600	1.582E+00
19.700	1.536E+00
19.800	1.492E+00
19.900	1.449E+00
20.000	1.409E+00
20.100	1.371E+00
20.200	1.334E+00
20.300	1.300E+00
20.400	1.266E+00
20.500	1.234E+00
20.600	1.204E+00
20.700	1.174E+00
20.800	1.146E+00
20.900	1.120E+00
21.000	1.094E+00
21.100	1.069E+00
21.200	1.045E+00
21.300	1.022E+00
21.400	1.000E+00
21.500	9.793E-01
21.600	9.590E-01
21.700	9.394E-01
21.800	9.206E-01
21.900	9.024E-01
22.000	8.849E-01
22.100	8.680E-01
22.200	8.516E-01
22.300	8.359E-01
22.400	8.207E-01
22.500	8.060E-01
22.600	7.917E-01
22.700	7.780E-01
22.800	7.647E-01
22.900	7.518E-01
23.000	7.393E-01
23.100	7.272E-01
23.200	7.155E-01

23.300	7.041E-01
23.400	6.931E-01
23.500	6.824E-01
23.600	6.720E-01
23.700	6.619E-01
23.800	6.521E-01
23.900	6.426E-01
24.000	6.334E-01
24.100	6.244E-01
24.200	6.157E-01
24.300	6.072E-01
24.400	5.989E-01
24.500	5.908E-01
24.600	5.830E-01
24.700	5.753E-01
24.800	5.679E-01
24.900	5.607E-01
25.000	5.536E-01
25.100	5.467E-01
25.200	5.400E-01
25.300	5.334E-01
25.400	5.270E-01
25.500	5.208E-01
25.600	5.147E-01
25.700	5.087E-01
25.800	5.029E-01
25.900	4.972E-01
26.000	4.917E-01
26.100	4.863E-01
26.200	4.810E-01
26.300	4.758E-01
26.400	4.707E-01
26.500	4.658E-01
26.600	4.609E-01
26.700	4.562E-01
26.800	4.515E-01
26.900	4.470E-01
27.000	4.425E-01
27.100	4.381E-01
27.200	4.339E-01
27.300	4.297E-01
27.400	4.256E-01
27.500	4.216E-01
27.600	4.176E-01
27.700	4.137E-01
27.800	4.100E-01
27.900	4.062E-01
28.000	4.026E-01
28.100	3.990E-01
28.200	3.955E-01

28.300	3.921E-01
28.400	3.887E-01
28.500	3.854E-01
28.600	3.821E-01
28.700	3.789E-01
28.800	3.758E-01
28.900	3.727E-01
29.000	3.696E-01
29.100	3.667E-01
29.200	3.637E-01
29.300	3.608E-01
29.400	3.580E-01
29.500	3.552E-01
29.600	3.525E-01
29.700	3.498E-01
29.800	3.472E-01
29.900	3.446E-01
30.000	3.420E-01

Appendix C

TALYS input file: M1

```
Z=  30 A=  68
 U[MeV]  fM1[mb/MeV]
   0.100   5.077E-01
   0.200   4.594E-01
   0.300   4.158E-01
   0.400   3.763E-01
   0.500   3.406E-01
   0.600   3.083E-01
   0.700   2.791E-01
   0.800   2.526E-01
   0.900   2.287E-01
   1.000   2.071E-01
   1.100   1.875E-01
   1.200   1.698E-01
   1.300   1.538E-01
   1.400   1.393E-01
   1.500   1.262E-01
   1.600   1.144E-01
   1.700   1.037E-01
   1.800   9.402E-02
   1.900   8.527E-02
   2.000   7.738E-02
   2.100   7.024E-02
   2.200   6.379E-02
   2.300   5.797E-02
   2.400   5.271E-02
   2.500   4.797E-02
   2.600   4.369E-02
   2.700   3.983E-02
   2.800   3.635E-02
   2.900   3.322E-02
   3.000   3.040E-02
   3.100   2.787E-02
   3.200   2.559E-02
```

3.300	2.355E-02
3.400	2.172E-02
3.500	2.009E-02
3.600	1.863E-02
3.700	1.733E-02
3.800	1.618E-02
3.900	1.516E-02
4.000	1.427E-02
4.100	1.349E-02
4.200	1.281E-02
4.300	1.223E-02
4.400	1.173E-02
4.500	1.132E-02
4.600	1.099E-02
4.700	1.073E-02
4.800	1.054E-02
4.900	1.041E-02
5.000	1.035E-02
5.100	1.034E-02
5.200	1.040E-02
5.300	1.051E-02
5.400	1.068E-02
5.500	1.091E-02
5.600	1.120E-02
5.700	1.155E-02
5.800	1.197E-02
5.900	1.245E-02
6.000	1.300E-02
6.100	1.363E-02
6.200	1.434E-02
6.300	1.514E-02
6.400	1.604E-02
6.500	1.704E-02
6.600	1.816E-02
6.700	1.941E-02
6.800	2.081E-02
6.900	2.238E-02
7.000	2.414E-02
7.100	2.611E-02
7.200	2.832E-02
7.300	3.080E-02
7.400	3.360E-02
7.500	3.674E-02
7.600	4.029E-02
7.700	4.429E-02
7.800	4.879E-02
7.900	5.384E-02
8.000	5.948E-02
8.100	6.575E-02
8.200	7.263E-02

8.300	8.007E-02
8.400	8.795E-02
8.500	9.604E-02
8.600	1.040E-01
8.700	1.113E-01
8.800	1.176E-01
8.900	1.220E-01
9.000	1.244E-01
9.100	1.242E-01
9.200	1.217E-01
9.300	1.170E-01
9.400	1.106E-01
9.500	1.032E-01
9.600	9.518E-02
9.700	8.709E-02
9.800	7.924E-02
9.900	7.184E-02
10.000	6.501E-02
10.100	5.880E-02
10.200	5.320E-02
10.300	4.820E-02
10.400	4.373E-02
10.500	3.976E-02
10.600	3.624E-02
10.700	3.310E-02
10.800	3.031E-02
10.900	2.782E-02
11.000	2.560E-02
11.100	2.362E-02
11.200	2.184E-02
11.300	2.023E-02
11.400	1.879E-02
11.500	1.749E-02
11.600	1.631E-02
11.700	1.523E-02
11.800	1.426E-02
11.900	1.337E-02
12.000	1.256E-02
12.100	1.181E-02
12.200	1.113E-02
12.300	1.050E-02
12.400	9.924E-03
12.500	9.390E-03
12.600	8.896E-03
12.700	8.438E-03
12.800	8.013E-03
12.900	7.619E-03
13.000	7.251E-03
13.100	6.909E-03
13.200	6.589E-03

13.300	6.290E-03
13.400	6.010E-03
13.500	5.748E-03
13.600	5.502E-03
13.700	5.270E-03
13.800	5.053E-03
13.900	4.848E-03
14.000	4.655E-03
14.100	4.472E-03
14.200	4.300E-03
14.300	4.137E-03
14.400	3.983E-03
14.500	3.837E-03
14.600	3.698E-03
14.700	3.567E-03
14.800	3.442E-03
14.900	3.323E-03
15.000	3.211E-03
15.100	3.103E-03
15.200	3.001E-03
15.300	2.903E-03
15.400	2.810E-03
15.500	2.721E-03
15.600	2.636E-03
15.700	2.555E-03
15.800	2.477E-03
15.900	2.403E-03
16.000	2.331E-03
16.100	2.263E-03
16.200	2.198E-03
16.300	2.135E-03
16.400	2.075E-03
16.500	2.017E-03
16.600	1.961E-03
16.700	1.908E-03
16.800	1.857E-03
16.900	1.807E-03
17.000	1.760E-03
17.100	1.714E-03
17.200	1.670E-03
17.300	1.627E-03
17.400	1.586E-03
17.500	1.546E-03
17.600	1.508E-03
17.700	1.471E-03
17.800	1.436E-03
17.900	1.401E-03
18.000	1.368E-03
18.100	1.336E-03
18.200	1.305E-03

18.300	1.275E-03
18.400	1.246E-03
18.500	1.218E-03
18.600	1.190E-03
18.700	1.164E-03
18.800	1.138E-03
18.900	1.113E-03
19.000	1.089E-03
19.100	1.066E-03
19.200	1.043E-03
19.300	1.021E-03
19.400	1.000E-03
19.500	9.794E-04
19.600	9.593E-04
19.700	9.398E-04
19.800	9.208E-04
19.900	9.024E-04
20.000	8.844E-04
20.100	8.670E-04
20.200	8.500E-04
20.300	8.336E-04
20.400	8.175E-04
20.500	8.019E-04
20.600	7.867E-04
20.700	7.719E-04
20.800	7.575E-04
20.900	7.434E-04
21.000	7.298E-04
21.100	7.164E-04
21.200	7.035E-04
21.300	6.908E-04
21.400	6.784E-04
21.500	6.664E-04
21.600	6.547E-04
21.700	6.432E-04
21.800	6.320E-04
21.900	6.211E-04
22.000	6.105E-04
22.100	6.001E-04
22.200	5.899E-04
22.300	5.800E-04
22.400	5.703E-04
22.500	5.608E-04
22.600	5.516E-04
22.700	5.426E-04
22.800	5.337E-04
22.900	5.251E-04
23.000	5.167E-04
23.100	5.084E-04
23.200	5.004E-04

23.300	4.925E-04
23.400	4.848E-04
23.500	4.772E-04
23.600	4.698E-04
23.700	4.626E-04
23.800	4.555E-04
23.900	4.486E-04
24.000	4.418E-04
24.100	4.351E-04
24.200	4.286E-04
24.300	4.223E-04
24.400	4.160E-04
24.500	4.099E-04
24.600	4.039E-04
24.700	3.981E-04
24.800	3.923E-04
24.900	3.867E-04
25.000	3.811E-04
25.100	3.757E-04
25.200	3.704E-04
25.300	3.652E-04
25.400	3.601E-04
25.500	3.551E-04
25.600	3.502E-04
25.700	3.453E-04
25.800	3.406E-04
25.900	3.360E-04
26.000	3.314E-04
26.100	3.270E-04
26.200	3.226E-04
26.300	3.183E-04
26.400	3.140E-04
26.500	3.099E-04
26.600	3.058E-04
26.700	3.018E-04
26.800	2.979E-04
26.900	2.940E-04
27.000	2.902E-04
27.100	2.865E-04
27.200	2.828E-04
27.300	2.793E-04
27.400	2.757E-04
27.500	2.723E-04
27.600	2.688E-04
27.700	2.655E-04
27.800	2.622E-04
27.900	2.590E-04
28.000	2.558E-04
28.100	2.526E-04
28.200	2.496E-04

28.300	2.465E-04
28.400	2.436E-04
28.500	2.406E-04
28.600	2.377E-04
28.700	2.349E-04
28.800	2.321E-04
28.900	2.294E-04
29.000	2.267E-04
29.100	2.240E-04
29.200	2.214E-04
29.300	2.189E-04
29.400	2.163E-04
29.500	2.138E-04
29.600	2.114E-04
29.700	2.090E-04
29.800	2.066E-04
29.900	2.043E-04
30.000	2.020E-04